Facile Fabrication of functional nanocomposites for supercapacitor applications

By

Yue Liang

A dissertation submitted to Graduate Faculty of

Auburn University

in partial fulfillment of the

requirements for the Degree of

Doctor of Philosophy

Auburn, Alabama

December 10, 2022

Keywords: nanocomposites, flexible electrode, energy storage, supercapacitors

Approved by

Dr. Xinyu Zhang, Chair, Professor, Department of Chemical Engineering

Dr. Majid Beidaghi, Assistant Professor, Department of Mechanical Engineering

Dr. Asha-Dee Celestine, Assistant Professor, Department of Aerospace Engineering

Dr. Russell Mailen, Assistant Professor, Department of Aerospace Engineering

Abstract

To address the energy crisis and environmental pollution issues, urgently need to develop an inexpensive, environmentally-friendly, and safe electrochemical energy storage system (EES). Supercapacitors (SCs) are considered promising energy storage device candidates due to their fast delivery rate, high power density, and long cycling life. However, finding an eco-friendly, low-cost, and high-energy density SC to meet commercial applications is still a challenge. To target the above-mentioned challenges, four aspects were investigated in this research: 1) energy storage mechanism through these functional nanocomposites, especially characterization and understanding of the electron and ionic transport behavior in complex interface, which could give us better design of the nanocomposite to improve the performances of the devices; 2) low-cost, sustainable raw materials (graphene, metal oxide, conducting polymer, cellulose) were chosen to synthesize electrodes for lower production cost; 3) functional nanocomposite electrodes were designed and fabricated to overcome the disadvantages of single component electrode material to enhance the performance of SC; 4) establish of facile, ultra-fast and high energy efficient approach for manufacturing of functional nanocomposites, with scale-up possibilities.

In the first project (Chapter 2), a high energy efficient and ultra-fast microwave heating technique was used to fabricate NiO_x@graphene electrode. Electrochemical studies indicated that the combination of NiO_x and graphene leads to a high specific capacitance of 623 F/g and excellent cycling stability due to the synergistic effect between NiO_x and graphene. Furthermore, three different types metal precursors

((Ni(OH)$_2$, Ni(Ac)$_2$·4H$_2$O and Ni(NO$_3$)$_2$·6H$_2$O) were used to prepare the NiO$_x$@graphene nanocomposite, and explore the electrode formation mechanism. It demonstrated that the microstructure and morphology of electrode materials were metal precursor-dependent, and directly related to the electrochemical performance. This work provides experimental support for the design of nanocomposite electrode architectures with high electrochemical performance for next generation energy storage devices.

Vanadium pentoxide (V$_2$O$_5$) possesses layered structure, a high theoretical specific capacity (2120 F/g), and a wide working potential window (up to 1.2 V in H$_2$O). According to the definition of energy density ($E = \frac{1}{2}CV^2$), which is proportional to the electrochemical potential window, V$_2$O$_5$ is believed to be one of the most promising electrode materials for the preparation of supercapacitors. In project 2 (Chapter 3), V$_2$O$_5$@polypyrrole (V$_2$O$_5$/PPy) core-shell nanofiber was synthesized by combining an economical, easy-to-process, and eco-friendly sol-gel with an *in situ* polymerization method to improve the energy density of SC. The PPy coating, with high conductivity, facilitated charge transfer and protected the dissolution of V$_2$O$_5$ in the aqueous solution. The symmetric device of V$_2$O$_5$/PPy device exhibited a maximum energy density of 37 Wh/Kg when the power density was 161 W/kg. The synergistic effect between the V$_2$O$_5$ and PPy and the individual role of each component in the electrochemical process were studied to further understand the growth mechanism and provide the rational design electrode material fundamental in the future.

With the development of rechargeable consumer electronics, portable and wearable electronic devices are rapidly appearing in our life, such as roll-up displays, smart textiles, etc. Flexible supercapacitor has become an emerging frontier research area. In project 3 (Chapter 4), nature abundant, renewable, non-toxic, biocompatible and biodegradable nanocellulose was used as building blocks to fabricate the freestanding, binder-free flexible polypyrrole/poly(styrene sulfonate)/cellulose nanopaper (PPy:PSS/CNP) electrode by a facile and fast vacuum filtration method. The optimized PPy:PSS/CNP exhibited high areal specific capacitance of 3.8 F/cm^2, an energy density of 122 $\mu Wh/cm^2$ and good cycling stability (80.9% capacitance retention rate, 5,000 cycles), which was superior to other cellulose-based composite materials. It is worth noting that PPy:PSS/CNP functions well as a flexible supercapacitor electrode material because of the following reasons: 1) poly(styrene sulfonate) (PSS) serves as a dopant and forms a water-soluble polymer network (PPy:PSS) with PPy, effectively improving the dispersity and processibility of PPy; 2) PPy with high conductivity enhances the charge transport rates and electrochemical properties (high specific capacitance, long cycling life, high power density); 3) Cellulose (CNF) is chosen as the flexible substrate, which provides good flexibility and mechanical strength for the electrodes due to large number of hydrogen bonds among cellulose molecules.

Compared to PPy, polyaniline (PANI) has a higher doping level of 0.5 (i.e. two monomer units per dopant) and a higher theoretical specific capacitance (750 F/g). In project 4 (Chapter 5), we used PANI, instead of PPy used in project 3, to synthesize

another promising flexible PANI:PSS/CNP electrode. The optimized PANI:PSS/CNP electrode exhibited a lower specific capacitance (2.56 F/cm^2), better cycling stability (81.5% capacitance retention rate, 8000 cycles), and higher mechanical strength (29.1 MPa) than PPy:PSS/CNP. The lower specific capacitance of PANI:PSS/CNP can be attributed to the lower conductivity of PANI (0.1-5 S/cm) than PPy (10-50 S/cm). The better cycling stability and higher mechanical strength properties of PANI:PSS/CNP might be explained by a stronger interaction between PANI and CNF. In comparison to the PANI:PSS/CNP, the cross-sectional morphology of PPy:PSS/CNP displayed obviously expanded interior lamellar structures, indicating a possible interruption of more hydrogen bonds among CNFs. The number of intermolecular and intramolecular hydrogen bonds reducing in nanocellulose will affect the mechanical properties of the nanopaper.

In summary, we have successfully designed and prepared four high-performance nanocomposite electrodes through simple, fast, high energy efficient, and low-cost approaches (microwave heating, *in situ* polymerization, and vacuum filtration). The charge transport and energy storage mechanism in the nanocomposites were investigated during the charge-discharge process. Our work is expected to provide experimental support to design functional nanocomposite electrodes with high electrochemical performance for next-generation energy storage devices.

Acknowledgments

Time flies, four years of Ph.D. study and research experience will be the most treasured treasure in my life journey. During the preparation of this thesis, I am grateful to those who have offered me encouragement and support during my study.

First and foremost, I would like to express my heartfelt gratitude to my supervisor, Dr. Xinyu Zhang, for his patience, constant encouragement, and guidance throughout my Ph.D. career.

Secondly, I should give my hearty thanks to my committee members and university reader, Dr. Russell Mailen, Dr. Majid Beidaghi, Dr. Asha-Dee Celestine, and Dr. Dengjun Wang for their patient instructions, their precious time, and insightful advice for my study here.

I would also like to extend my deep grateful to Dr. Ruigang Wang and his student Zhen Wei for helping us with material characterization tests. I would like to thank my group members for their help and support in the lab. I greatly appreciate the China Scholarship Council supporting my Ph.D. study.

Last but not least, I am deeply indebted to my family and friends, who have helped me and shared with me my worries, frustrations, and happiness.

Table of Contents

Abstract II

Acknowledgments VI

Publications X

List of Figures XI

List of Tables XIX

List of Abbreviations XX

Table of contents VII

Chapter 1: Introduction 1

1.1 History of supercapacitors 5

1.2 Fundamentals of supercapacitors 7

1.3 Electrochemical testing system 18

1.4 Electrochemical experiment evaluation 19

1.4.1 Cyclic voltammetry (CV) 19

1.4.2 Galvanostatic charge-discharge (GCD) 21

1.4.3 Energy and power density 23

1.4.4 Electrochemical impedance spectroscopy (EIS) 24

1.5 Synthetic method 25

1.5.1 Electrochemical deposition 25

1.5.2 Sol-gel method 26

1.5.3 Hydrothermal/solvothermal methods 27

1.5.4 Microwave-assisted method 28

1.6 Electrolyte effect 29

1.6.1 Aqueous electrolyte 30

1.7 Electrode material 32

1.7.1 EDLCs materials 33

1.7.2 Pseudocapacitor materials 39

1.8 Research Objectives and Approach 53

Chapter 2: The microwave facile synthesis of NiO_x@graphene nanocomposites for

application in supercapacitors: insights into the formation and storage mechanisms .56
2.1 Introduction 57
2.2 Experimental 60
2.2.1 Material Characterization.....60
2.2.2 Materials 61
2.2.3 Preparation of the NiOx/Graphene Nanocomposite 62
2.3 Electrochemical Measurements.....64
2.4 Results and Discussion.....65
2.5 Conclusions 78
Chapter 3: Fabrication of V_2O_5@PPy core-shell nanofiber electrode for supercapacitor 80
3.1 Introduction 80
3.2 Experimental 84
3.2.1 Materials Characterization 84
3.2.2 Materials 84
3.2.3 Preparation of V_2O_5 nanofiber 84
3.2.4 Preparation of V_2O_5@PPy nanofibers 85
3.2.5 Electrochemical measurements.....86
3.3 Results and discussions 87
3.4 Electrochemical characterization 89
3.5 Conclusion.....97
Chapter 4: High performance flexible freestanding conductive nanopaper based on PPy:PSS nanocellulose composite for supercapacitors 99
4.1 Introduction 100
4.2 Experimental section 103
4.2.1 Materials 103
4.2.2 Preparation of cellulose nanopaper (CNP) 104
4.2.3 Preparation of PPy:PSS/CNP.....104
4.2.4 Tensile test 106

4.2.5 Conductivity measurement 106
4.2.6 Electrochemical measurements 107
4.2.7 Materials Characterization 108
4.3 Results and discussions 109
4.3.1 Materials characterization 109
4.3.2 Mechanical property 112
4.3.3 Conductivity 113
4.3.4 Electrochemical characterization 114
4.4 Conclusions 120
Chapter 5: Flexible and freestanding PANI: PSS/CNF nanopaper electrodes with enhanced electrochemical performance for supercapacitors 122
5.1 Introduction 123
5.2 Experiments 126
5.2.1 Materials 126
5.2.2 Preparation of cellulose nanopaper (CNP) 126
5.2.3 Preparation of PANI: PSS/CNP 127
5.2.4 Tensile test 128
5.2.5 Conductivity measurement 129
5.2.6 Electrochemical measurements 129
5.2.7 Materials Characterization 130
5.3 Results and discussions 131
5.3.1 Materials characterization 131
5.3.2 Mechanical property 134
5.3.3 Conductivity 136
5.3.4 Electrochemical characterization 137
5.4 Conclusion 144
Chapter 6: Conclusion and future work 145
Reference 150

List of Figures

Figure 1.1 Ragone plot of different electrochemical energy conversion systems .3

Figure 1.2 Applications of supercapacitors.....4

Figure 1.3 (a) Schematic diagram of supercapacitor; (b) The charging stage (ion adsorption) and (c) discharging stage (ion desorption).....5

Figure 1.4 (a) The charge process of EDLC; (b) The formation of EDLC; (c) The discharge process of EDLC 7

Figure 1.5 The electrochemical behavior of different types electrode materials. (a,d) electrical double layer, (b, e) pseudocapacitive, and (c,f) battery type. (a-c) Schematic of galvanostatic charge-discharge profiles showing linear and nonlinear responses with time and (d-f) corresponding CV profiles 10

Figure 1.6 Cyclic voltammograms for (a) spinel (b) layer structure of $LiCoO_2$ (c) Discharge curves of $LiCoO_2$ in various crystallite sizes.....11

Figure 1.7 Schematic diagrams of the different faradaic processes that give rise to pseudocapacitance: (a) monolayer adsorption pseudocapacitance (underpotential deposition), (b) surface redox pseudocapacitance, and (c) intercalation pseudocapacitance.....13

Figure 1.8 Illustration of the electrode processes occurring at (a) electrical double-layer capacitive, (b) pseudocapacitive, and (c) faradaic electrodes..14

Figure 1.9 Schematic of different charge storage mechanisms. (a) Charge storagemechanism of rechargeable battery, (b) Charge storage mechanism of supercapacitor, (c) Charge storage mechanism of intercalation

pseudocapacitance 14

Figure 1.10 (a) CV profiles of VSe_2 at different scan rates and (b) Relationship between log (i) and log(υ) at each redox-peak pair; (c) Capacitive contribution of pseudocapacitive at 1.1 mV/s; (d) The contribution ratio of pseudocapacitive 17

Figure 1.11 Schematic illustration of two and three-electrode measurements for on-chip supercapacitor materials 19

Figure 1.12 (a) Cyclic voltammetry potential sweeps plotted vs. time, (b) The resulting measured current of an ideal SC plotted vs. time, (c) The CV curve, showing the current plotted vs. potential 20

Figure 1.13 Sample SC CV non-idealities: (a) sweep rate limitations, (b) potential window that exceeds electrolyte stability window, (c) pseudocapacitive charge storage 21

Figure 1.14 Galvanostatic charge-discharge plots of (a) EDLC and (b) pseudocapacitive material 22

Figure 1.15 Nyquist plots of the three prepared different material electrodes.....25

Figure 1.16 The materials prepared by electrochemical deposition method 26

Figure 1.17 Different types of carbon nanotubes 37

Figure 1.18 Fabrication of coaxial yarn asymmetric supercapacitor 37

Figure 1.19 Illustration of 2D graphene sheet as the building blocks for other carbon materials such as particle, 1D CNT, and 3D graphite 39

Figure 1.20 The different TMOs theoretical capacitances based on cyclic

voltammograms 41

Figure 1.21 Four polymorphs of MnO_2: (a) α-MnO_2, (b) λ-MnO_2, (c) β-MnO_2, and (d) γ-MnO_2 43

Figure 1.22 (a) 3D free-standing binder-free Ni@NiO nanowire membrane; (b) Volume capacitance with respect to the current density; (c) Energy and power density of the NiO/GF//HPNCNTs asymmetric SC and positive and negative electrode morphology.....46

Figure 1.23 Chemical structures of common used conducting polymers 50

Figure 1.24 Illustration of conducting polymer's charging/discharging mechanism with two doping states: (a) p-doping and (b) n-doping 53

Figure 2.1 Illustration of the microwave synthesis of the NiO_x@graphene composites 63

Figure 2.2 XRD patterns for NiO_x@GR-A2, NiO_x@GR-B2, and NiO_x@GR-C2 66

Figure 2.3 (a) XPS spectrum of the NiO_x@GR-C2; (b) High-resolution XPS spectrum of Ni 2p 66

Figure 2.4 SEM images of (a),(b) NiO_x@GR-A2, (d),(e) NiO_x@GR-B2, and (g),(h) NiO_x@GR-C2 at different magnifications. TEM images of (c) NiO_x@GR-A2, (f) NiO_x@GR-B2, and (i) NiO_x@GR-C2 68

Figure 2.5 (a) SEM image of NiO_x@GR-C2 (inset: EDS composite elemental map); elemental mapping: (b) carbon (C), (c) nickel (Ni), (d) oxygen (O); (e) EDS spectrum 69

Figure 2.6 (a) N_2 adsorption-desorption isotherms and (b) the BJH pore size distribution plots of NiO_x@GR-A2, NiO_x@GR-B2, and NiO_x@GR-C2.....70

Figure 2.7 Specific capacitance of the NiO_x@GR nanocomposites at different current densities: (**a**) NiO_x@GR-A1, NiO_x@GR-A2, and NiO_x@GR-A3; (b) NiO_x@GR-B1, NiO_x@GR-B2, and NiO_x@GR-B3; and (**c**) NiO_x@GR-C1, NiO_x@GR-C2, and NiO_x@GR-C3.....71

Figure 2.8 (a) CV curves, (b) GCD curves (c) specific capacitance, (d) Cyclic stability, and (e) Nyquist plots of the EIS (The inset shows the enlarged EIS of the electrodes.....72

) of NiO_x@GR-A2, NiO_x@GR-B2, and NiO_x@GR-C2 72

Figure 2.9 (a) CV curves of NiO_x@GR-C2 at varied scan rates. (b) GCD curves of NiO_x@GR-C2 at different current densities.....74

Figure 2.10 (a) CV graph indicating the capacitive contribution of NiO_x@GR-C2 at 20 mV/s. (b) The calculated b values at different scan rates. (c) A stacked bar graph showing the percentage of the total capacitance attributed to the diffusion-limited and capacitive contributions.....78

Figure 3.1 The TGA curves of the V_2O_5@PPy-n (n = 0, 1, 2, 3).....87

Figure 3.2 FTIR spectra of V_2O_5@PPy 88

Figure 3.3 (a) SEM and (b) TEM image of V_2O_5@PPy; (c) Elemental mapping images of vanadium (V), carbon (C), nitrogen (N) and oxygen (O) 89

Figure 3.4 CV curves of (a) V_2O_5@PPy-1; (b) V_2O_5@PPy-2; (c) V_2O_5@PPy-3 at

different scan rates; Charge-discharge curves of (d) V_2O_5@PPy-1; (e) V_2O_5@PPy-2; (f) V_2O_5@PPy-3 at different current density 91

Figure 3.5 (a) CV and (b) GCD curves for V_2O_5@PPy-n; (c) The cycling stability of V_2O_5@PPy-n at 3 A/g; (d) Nyquist plots for V_2O_5@PPy-n. The inset shows the enlarged view of the intercepts of the corresponding EIS curves at the real axis at the medium-high frequency region..... 94

Figure 3.6 The calculated b values during the anodic and cathodic scans for (a) V_2O_5@PPy-1; (b) V_2O_5@PPy-2; (c) V_2O_5@PPy-3; and the contribution detail of surface capacitive and diffusion limited for (d) V_2O_5@PPy-1; (e) V_2O_5@PPy-2; (f) V_2O_5@PPy-3..... 96

Figure 3.7. (a) CV and (b) GCD curves of V_2O_5@PPy//V_2O_5@PPy; (c) The cycling stability and (d) specific capacitance of V_2O_5@PPy//V_2O_5@PPy; (e) The Ragone plot..... 97

Figure 4.1 The schematic formation of PPy:PSS/CNF composite 106

Figure 4.2 FTIR spectra of CNP, PPy:PSS, and PPy:PSS/CNP 110

Figure 4.2 SEM surface and cross-section images of (a, b, and c) pure CNP, and (d, e, and f) PPy:PSS/CNP..... 111

Figure 4.3 EDS spectra of PPy:PSS/CNP..... 111

Figure 4.4 (a) Stress vs strain plot and (b) Tensile strength for CNP and PPy:PSS/CNP with different PPy:PSS mass loading; (c) Snapshots of PPy:PSS/CNP-4 strip, which can still lift up a static load of 800 g 113

Figure 4.5 (a) Conductivity and (b) Photographs of PPy:PSS/CNP-4 films with

different bending angles 114

Figure 4.6 The electrochemical performance of PPy:PSS/CNP-4 electrode in 1 M H_2SO_4 electrolyte. (a) CV curves; (b) GCD curves; (c) Specific capacitance based on areal and volume as functions of current density; (d) Specific capacitance based on total weight and active material weight as functions of current density; (e) Nyquist plot; (f) Cycling stability at 10 mA/cm^2 116

Figure 4.7 Stress vs strain plot of PPy:PSS/CNP-4 and PPy:PSS/CNP-4 after the cycling stability test (5000 cycles) in the three-electrode system 118

Figure 4.8 (a) CV curves and (b) digital photos of PPy:PSS/CNP-4 at different bending angles 118

Figure 4.9 (a) Schematic illustration of the PPy:PSS/CNP supercapacitor device; (b) CV curves at different scan rate; (c) GCD curves at different current density; (d) Specific capacitance based on area and volume; (e) Specific capacitance based on total weight and active material weight; (f) Cycling stability at 5 mA/cm^2 120

Figure 4.10 Ragone plots the symmetrical PPy:PSS/CNP supercapacitor device based on (a) area and (b) volume in comparison with other cellulose materials 120

Figure 5.1. The schematic formation of PANI: PSS/CNP 128

Figure 5.2 FTIR spectra of CNP, PANI: PSS, and PANI: PSS/CNP 132

Fig.2. (a) XPS survey spectra of PANI: PSS/CNP; (b) N1s spectra of PANI: PSS/CNP 133

Figure 5.4. (a, b, and c) SEM surface and cross-section images of pure CNP, and (d, e, and f) PANI: PSS/CNP 134

Figure 5.5 EDS spectra of PANI: PSS/CNP 134

Figure 5.6 (a) Stress vs strain plot and (b) Tensile strength for CNP and PANI: PSS/CNP with different PANI: PSS mass loading; (c) Photograph of the PANI: PSS/CNP-4 strip, which could lift up a static load of 800 g.....136

Figure 5.7 (a) Conductivity and (b) Photographs of PANI: PSS/CNP-4 with different bending angles.....137

Figure 5.8 The electrochemical performance of PANI: PSS/CNP-4 in 1 M H_2SO_4 electrolyte. (a) CV curves; (b) GCD curves; (c) Specific capacitance based on areal and volume as a function of current density; (d) Specific capacitance based on total weight and active material weight as a function of current density; (e) Nyquist plot; (f) Cycling stability at 10 mA/cm^2 139

Figure 5.9 (a) Digital photos of PANI: PSS/CNP-4 at different bending angles (0 º, 90 º, and 180 º), (b) CV curves, (c) GCD curves, and (d) Specific capacitance of PANI: PSS/CNP-4 at different bending angles under 10 mA/cm^2 140

Figure 5.10 (a) Schematic illustration of the PANI: PSS/CNP supercapacitor device, (b) CV curves at different scan rate; (c) GCD curves at different current density; (d) Specific capacitance based on area and volume; (e) Specific capacitance based on total weight and active material weight; (f) Cycling stability of PANI: PSS/CNP device at 2 mA/cm^2 143

Figure 5.11 Ragone plots the symmetrical PANI: PSS/CNP supercapacitor device

based on (a) area and (b) volume in comparison with other cellulose materials.....143

List of Tables

Table 1.1 The comparison of supercapacitors with capacitors and batteries 3

Table 2.1 Operation conditions for synthesizing NiO_x@graphene 63

Table 2.2 Operation conditions for synthesizing NiO_x@graphene 63

Table 2.3 Operation conditions for synthesizing NiO_x@graphene 64

Table 2.4 Comparison of the electrochemical properties of NiO_x@GR prepared through microwave heating with previously reported approaches 73

Table 2.5 Comparison of the electrochemical properties of NiO_x@GR with previously reported work 76

Table 3.1 Operation conditions for synthesizing V_2O_5@PPy-n composites.....85

Table 4.1 Operation conditions for synthesizing PPy:PSS/CNP 105

Table 4.2 Comparison of PPy:PSS/CNP electrode with reported nanocellulose supported conductive material based supercapacitors 117

Table 5.1 Operation conditions for synthesizing PANI: PSS/CNP.....128

Table 5.2 Comparison of PANI: PSS/CNP electrode with other PANI-based electrode materials 141

List of Abbreviations

AC	Activated Carbon
1D	One-Dimensional
2D	Two-Dimensional
3D	Three-Dimensional
APS	Ammonium Peroxydisulfate
ASC	Asymmetric Supercapacitor
BET	Brunauer-Emmett-Teller
BJH	Barrett-Joyner-Halenda
CE	Counter Electrode
CNF	Cellulose Nanofiber
CNP	Cellulose Nanopaper
CNT	Carbon Nanotube
CPs	Conducting Polymers
CV	Cyclic Voltammetry
EDLC	Electric Double-Layer Capacitors
EDS	Energy-Dispersive X-Ray Spectroscopy
EES	Energy Storage System
EIS	Electrochemical Impedance Spectroscopy
ESR	Equivalent Series Resistance
FTIR	Fourier Transform Infrared

GCD	Galvanostatic Charge-Discharge
GN	Graphene
GO	Graphene Oxide
MWNT	Multi-Walled Nanotube
PA	Polyacetylene
PANI	Polyaniline
PEDOT	Poly(3,4-ethylenedioxythiophene)
PPy	Polypyrrole
PSS	Polystyrene Sulfonate
PTH	Polythiophene
RE	Reference Electrode
RGO	Reduced Graphene Oxide
SC	Supercapacitor
SDBS	Sodium Dodecylbenzene Sulfonate
SEM	Scanning Electron Microscopy
SWCNT	Single-Walled Nanotube
TEM	Transmission Electron Microscopy
TGA	Thermogravimetric Analysis
TMOs	Transition Metal Oxides
WE	Working Electrode
XPS	X-Ray Photoelectron Spectroscopy
XRD	X-Ray Diffraction

Publications

1. **Liang Yue**, Zhen Wei, Ruigang Wang * , Xinyu Zhang * . The microwave facile synthesis of NiO_x@graphene nanocomposites for application in supercapacitors: insights into the formation and storage mechanisms. Coatings. 12.8 (2022): 1060.
2. **Liang Yue**, Zhen Wei, Hung-En Wang, Ruigang Wang * , Xinyu Zhang * . High performance flexible freestanding conductive nanopaper based on PPy:PSS nanocellulose composite for supercapacitors. SCIENCE CHINA Materials. (Accepted).
3. **Liang Yue**, Zhen Wei, Hung-En Wang, Martin Flores, Ruigang Wang * , Xinyu Zhang * . Flexible and freestanding PANI:PSS/CNF nanopaper electrodes with enhanced electrochemical performance for supercapacitors. Journal of Power Sources. 548 (2022): 232071.
4. **Liang Yue**, Zhen Wei, Ruigang Wang * , Xinyu Zhang * . Fabrication of V_2O_5@PPy core-shell nanofiber electrode for supercapacitor. ES Energy & Environment. (Accepted).

Chapter 1: Introduction

With the rapid development of the world that has led to the gradual exhaustion of fossil fuels, global warming, and the pollution situation; there is an urgent need to develop secure, sustainable energy to satisfy the future development of low-carbon and sustainable economies. However, some renewable energy sources such as solar, wind, ocean, and biomass are intermittent and geographical, which limits their applications. Therefore, safe electrochemical energy storage systems (EESs) play a critical role in utilizing sustainable and renewable energy resources, especially with the advent of electric vehicles, smart grids, and various portable and integrated of wireless devices in our life. The conventional energy storage systems such as (batteries, capacitors, and fuel cells) that convert energy through diffusion and migration of ions are widely employed in high technology industries. Among them, batteries dominate the market for electrical energy storage devices because of their good energy density. However, the rechargeable batteries store the charge through electrochemical reactions within the crystalline structures of electrode materials, resulting in ‘‘phase-transformation’’ of the electrode material, significantly reducing the power density and battery charging and discharging rates. The conventional dielectric capacitor can provide high power density and fast charging and discharging process, but its energy density is less than 1-2 orders of magnitude than that of battery. It is worth noting that neither traditional batteries nor capacitors can meet the requirements of modern technology with high power density and high energy density.

As shown in **Figure 1.1**, the ragone plot can explain the performance gap between batteries and capacitors. This plot explains that capacitors are high power systems, whereas batteries and fuel cells are high-energy systems. The supercapacitor (SC) overlaps with traditional capacitors and batteries, which means that it maintains the high power nature of the capacitor and high energy density characteristics of the battery at the same time, filling the power/energy gap between the battery and the capacitor. Besides, it is clear that developing high energy density SCs that are close to current rechargeable batteries is a major challenge in the future. In addition, SCs store electrical energy through the ion adsorption/desorption process between the electrode and electrolyte interface and the surface faradic redox reactions. The electrostatic work mechanism makes them lower in internal resistance, exhibiting a very high degree of reversibility with good cycle stability (>500,000 cycles) compared to batteries. **Table 1.1** gives the comparison of SCs with capacitors and batteries. [1] The great advantages of SCs make it best suit applications such as back-up devices for mobile electronic equipment (telephone, laptop, camera, etc.), surge-power delivery devices for hybrid electrical vehicles, and solar lighting system, etc. (**Figure 1.2**). SC as an advanced energy storage device has fascinated massive attention from the world.

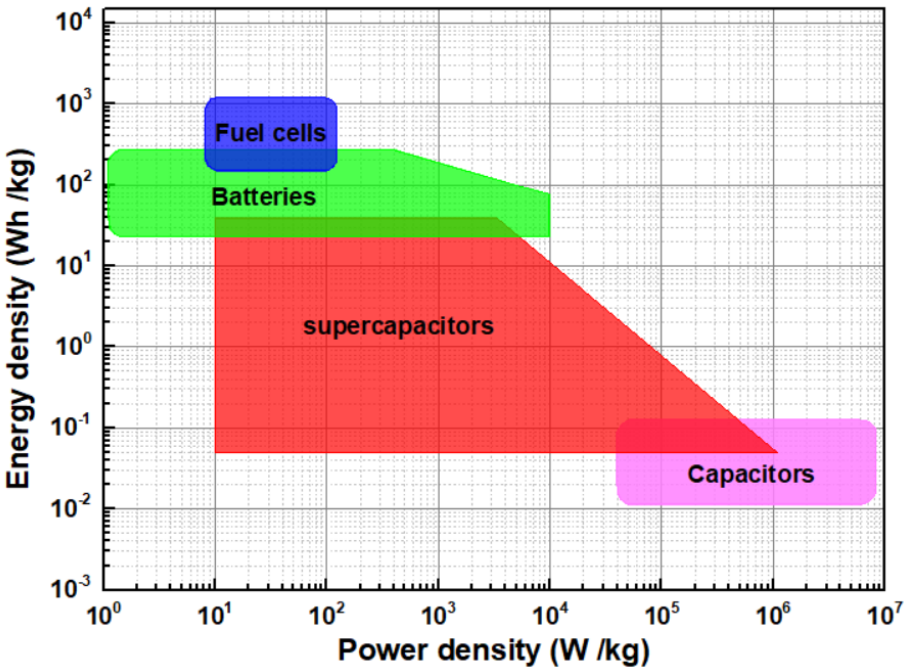

Figure 1.1 Ragone plot of different electrochemical energy conversion systems

Table 1.1 The comparison of supercapacitors with capacitors and batteries

Features	Capacitor	Supercapacitor	Battery
Specific energy (Wh/kg)	<0.1	1-10	10-100
Specific power (W/kg)	≥10,000	500-10,000	<1000
Discharge time	10^{-6} to 10^{-3} s	s to min	0.3-3 h
Charge time	10^{-6} to 10^{-3} s	s to min	1-5 h
Cycle-life	Almost infinite	>500,000	About 1000
Storage mechanism	Physical	Physical	Chemical

Figure 1.2 Applications of supercapacitors

Normally, the SC device is composed of two electrodes separated by a semipermeable membrane separator, electrolyte solution, and current collector **Figure 1.3**.[2] The electrode material directly determines the characteristic of SCs; particularly, the surface area and the distribution of pore-size. Hence, the selection and design of electrode materials and their modification are very important in the development of advanced high-performance SCs. Researchers usually prefer to use larger specific surface area carbon-based materials, multiple oxidation states metal oxides, and high conductivity conducting polymers as electrode materials. Also, to improve the SC performance, various synthesis techniques were applied to control the structures and properties of the materials for suitable electrochemical SC applications including electrochemical deposition, hydrothermal/solvothermal methods, microwave-assisted method, and sol-gel method based on the reported articles. The electrolyte is another important constituent that determines the performance of a SC and that influences the

operating voltage. For example, ionic liquids electrolytes allow the cell operating voltages range from 2 to 6 V, which is much higher than that of the aqueous electrolytes, operating within 1.23 V, with low conductivity ≤ 10 mS/cm. On account of the fact that the energy density ($E = \frac{1}{2}CV^2$) is proportional to the square of the cell voltage and the energy density is mostly influenced by the electrolyte. Clearly, the fabrication of high-performance SC should consider the combined effect of the above factors.

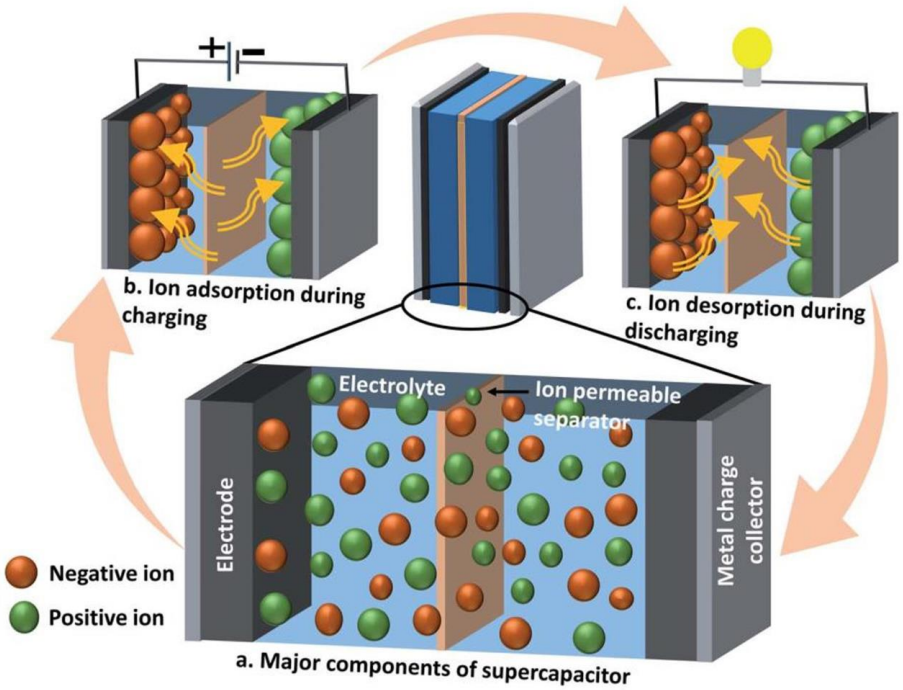

Figure 1.3 (a) Schematic diagram of supercapacitor; (b) The charging stage (ion adsorption) and (c) discharging stage (ion desorption)

1.1 History of supercapacitors

The capacitor originated from the famous Leyden jar experiment in 1754. The device consisted of a metal foil served as the electrode and a glass vessel served as the dielectric. During the charging process, the positive and negative charges moved in the opposite direction and accumulated on the electrode, forming the capacitor. In

1879, the concept of double-layer was proposed by Von Helmholtz to define this type of charge storage mechanism by Von Helmholtz.[3] Unfortunately, the concept was applied in practice until 1957 when the first patent technology of electric double-layer capacitor (EDLC) was granted to General Electric Company. For the first SC, the activated charcoal electrode was separated by an ion-permeable film and immersed in an electrolyte. During the charging process, the carbon pores were used to store energy.[4] The device showed high specific capacitance due to the porous structure of activated charcoal with a high surface area. At this time, the EDLCs were not commercialized. In 1968, SOHIO, the standard oil company of Ohio, obtained another patent for a device with a capacitance higher than Becker to further promote the development of SCs. However, they had to transfer the patent to NEC in 1975 due to the company's administrative issue. In 1978, NEC began to apply the device to electric vehicles and named them "Supercapacitor". Since then, the doors of commercial applications have opened to SCs, and until now it has been widely used in various fields. Nowadays, to further improve the energy storage performance of SC, various active electrochemical materials have been studied from traditional carbon materials with high surface areas such as graphene, carbon nanotubes (CNTs), and activated carbons (ACs) to a variety of pseudocapacitive materials, which normally have a higher capacitance and energy density than EDLC materials, for example, metal oxide and conducting polymer.[5-11] Moreover, companies such as Panasonic, Maxwell, and NESS have also invested a great deal of interest in SC. In general, the research and commercialization of SCs mainly developed in Japan, United States,

South Korea, Russia, Switzerland, and France at the early stage. However, the current SC market almost filled the products from the United States, Japan, and Russia.

1.2 Fundamentals of supercapacitors

Understanding the ion storage and transport mechanisms of energy storage systems is extremely important, which gives a direction to advance the performance of devices. According to the charge storage mechanism, SCs can be classified into two types of capacitors: electric double-layer capacitors (EDLCs) and pseudocapacitors.[12] The EDLC stores energy through the electrostatic storage process, which prevents the production of defects in the electrode by forming/opening the chemical bonds, resulting in excellent cycle life, high power density, and rapid charge rate compared to conventional batteries. In **Figure 1.4**, when the potential is applied to the electrodes, opposite ions in the electrolyte accumulate on the surface of each electrode, leading to double-layer, which separated by solvent molecules. The energy was stored during the charge adsorption process.[13]

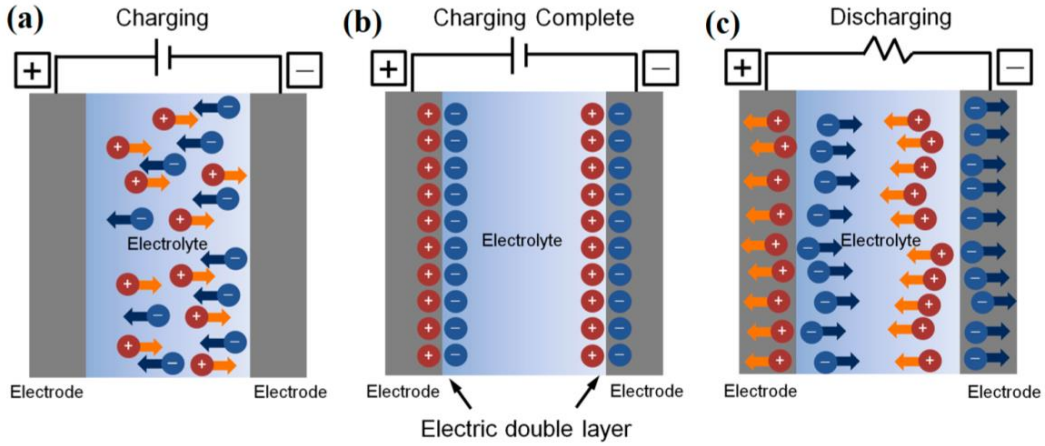

Figure 1.4 (a) The charge process of EDLC; (b) The formation of EDLC; (c) The discharge process of EDLC

The stored total charge Q_c for EDLCs is a linear function of the potential difference ΔU:

$$Q_c = C\Delta U \tag{1.1}$$

The capacitance of the electrochemical double layer capacitor is given by:

$$C = \varepsilon_0 \varepsilon_r \frac{A}{D} \tag{1.2}$$

Where C is the capacitance of a single electrode;

A is the area of the electrode;

D is the distance between the double layers;

ε_0 is the electric constant of free space;

ε_r is the dielectric constant of the insulating material between the electrodes.

The specific capacitance (C) is directly proportional to the surface area A of each electrode and inversely proportional to the distance D between the double layer.

When the capacitance of the EDLC is constant, the response current can be presented by

$$I = \frac{dQ}{dt} = C\frac{dV}{dt} \tag{1.3}$$

Where V is the applied voltage and the charge time is t. if using the v present the scan rate

$$v = \frac{dV}{dt} \tag{1.4}$$

The equation converts to

$$I = Cv \tag{1.5}$$

This equation can better explain why the electrochemical behavior of electric double layer capacitors is triangular in galvanostatic charge/discharge curves and

rectangular in cyclic voltammogram curves.

The energy stored is calculated according to：

$$E = \frac{1}{2}CV^2 \tag{1.6}$$

Where *C* is the specific capacitance in Farads, *V* is the nominal voltage, and *E* is the energy density. The stored energy in a capacitor is directly proportional to its capacitance. The specific power (*P*) of SC is dependent on the voltage during discharge of the capacitor and the equivalent series resistance (ESR) in ohms, given by the following equation [16]. Ideal the ESR is expected to be as low as possible.

$$P = \frac{V^2}{4R} \tag{1.7}$$

This equation shows the relation between the ESR and the maximum power of a capacitor.

The pseudocapacitor is another kind of SC, considered as a complementary form of EDLC, which stores energy not depending on the electrostatic in origin but relies on the faradaic redox reaction or ion intercalation between or near the surface of the electrode and electrolytes. Similarly to the EDLC, which presents a continuous, highly reversible change in the oxidation state during charge/discharge, the electrochemical signatures of ideal pseudocapacitors exhibit the (quasi)-rectangular cyclic voltammetry (CV) curves and almost linear galvanostatic charge-discharge (GCD) curves. The relationship between the potential and the time and between the potential and the stored charge is demonstrated from the figure of the voltage versus capacity under a constant current measurement. According to equation 1.1, the capacitance can be estimated by

$$C = \frac{dQ_C}{d\Delta U} \tag{1.8}$$

Although both batteries and pseudocapacitors store charges via redox reaction, nevertheless, batteries depend on the intercalation/de-intercalation of cations (H^+ or Li^+) within the crystalline framework of the active material which is often accompanied by a phase transformation of material. This characteristic can be presented in the CV curves with distinct peaks and in the galvanostatic charge-discharge profiles with plateaus. On the other hand, the electrochemical feature of pseudocapacitive materials is the quasi-linear relationship between capacity and voltage compared to battery-type materials. To sum up, whether we have a redox reaction or not, from the definition of pseudocapacitance proposed by B. E. Conway we can have a clear boundary of between EDLC and pseudocapacitors. **Figure 1.5** summarizes the electrochemical behavior of different type electrode materials.[14]

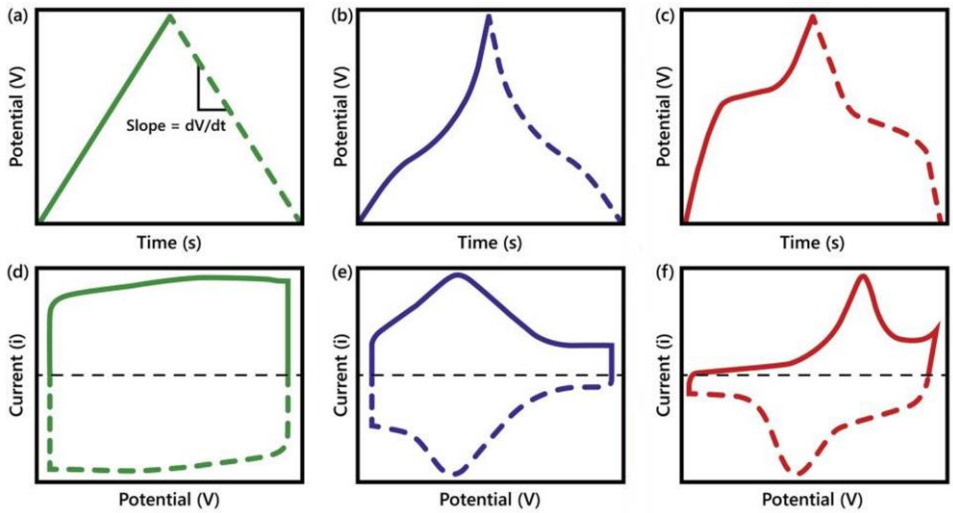

Figure 1.5 The electrochemical behavior of different types electrode materials. (a,d) electrical double layer, (b, e) pseudocapacitive, and (c,f) battery type. (a-c) Schematic of galvanostatic charge-discharge profiles showing linear and nonlinear responses with time and (d-f) corresponding CV profiles

In recent years, with the rapid development of nanotechnologies, more and more electrodes based on nanomaterials have been developed in batteries. Nanoscale size materials decreased the diffusion distance of ions and increased the specific surface area of materials, which changed the "bulk redox reaction" to "surface redox reaction". Under such circumstances, some battery materials exhibited extrinsic pseudocapacitive properties that were signatures in CV and GCD profiles. For example, $LiCoO_2$ was a typical battery material that showed redox peaks at 4.0/3.85V for layer $LiCoO_2$ and quasi-reversible process at 3.85/3.3V for spinel $LiCoO_2$ and in CV curves.[15] The lower reversibility for the $LiCoO_2$ spinel arose from the structure difference between $LiCoO_2$. The spinel structure of $LiCoO_2$ with tetrahedral sites had smaller Li-ion insertion volume sites than layered $LiCoO_2$ with octahedral sites. With the decrease in material size, the discharge peaks almost disappeared and the capacitor behavior became more dominant. Dunn *et al.* defined this behavior as "extrinsic pseudocapacitance".[16] **Figure 1.6** shows the effect of material size on the electrochemical performance of $LiCoO_2$.[15, 17]

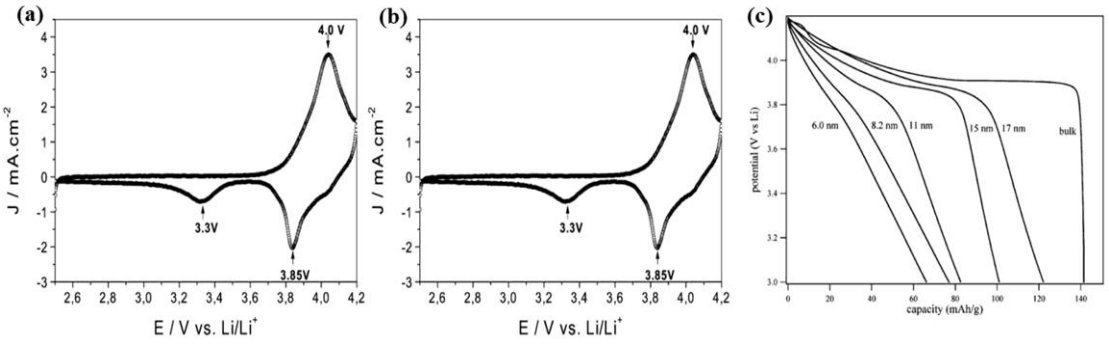

Figure 1.6 Cyclic voltammograms for (a) spinel (b) layer structure of $LiCoO_2$ (c) Discharge curves of $LiCoO_2$ in various crystallite sizes

From this aspect, the traditional definition of "pseudocapacitor material" cannot distinguish it well from "battery material". On the other hand, in order to overcome the shortcoming of the lower power density of batteries and low energy density of capacitor, hybrid SC systems combing the battery-type electrodes and SC type electrodes were designed and fabricated, resulting in further confusion. In terms of kinetics, pseudocapacitive materials limited by surface-related processes could be distinguished from battery-type materials controlled by diffusion reactions by analysis of electrochemical experiments. The new charge storage mechanism named "intercalation pseudocapacitance" was further defined by Dunn and Simon *et al*.[18] Compared to surface redox pseudocapacitance, the faradaic charge transfer of intercalation pseudocapacitance occurs in the bulk. On the other hand, there is no phase change when ion intercalation and de-intercalation into the tunnels or layers of the electrode material. As a practical example, a pseudocapacitive material will generally have the electrochemical characteristics of one, or a combination, of the following categories: (i) monolayer adsorption pseudocapacitance (under-potential deposition), (ii) surface redox pseudocapacitance and (iii) intercalation pseudocapacitance (**Figure 1.7**).[19] Underpotential deposition is not a very common approach, it occurs mainly under the reduction potential higher than itself when deposition a metal on to another metal surface resulting in an absorption monolayer (e.g., Pd^{2+} on Au).[20] Surface redox pseudocapacitance is the most common pseudocapacitive reaction that depends on the redox reaction at or near the surface of a material. For example, the first surface redox pseudocapacitive behavior material is

RuO_2 in 1971.[21] Intercalation pseudocapacitance with no crystallographic phase change occurs when insertion cations into the crystal structure of the electrode are accompanied by a Faraday charge transfer process (e.g., Nb_2O_5).[22] Based on the above description, we can summarize the different charge storage mechanisms shown in **Figure 1.8 and 1.9**.[14, 23]

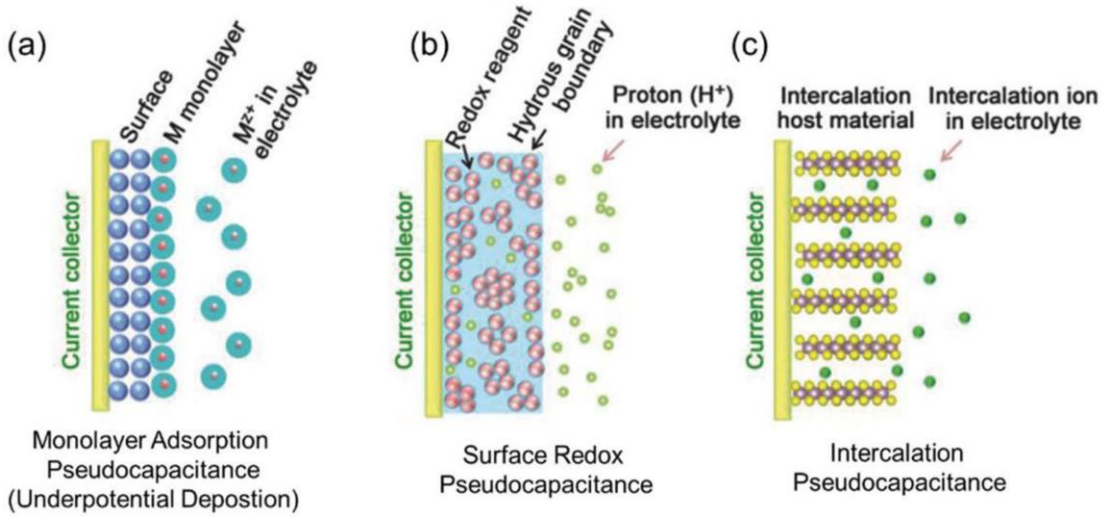

Figure 1.7 Schematic diagrams of the different faradaic processes that give rise to pseudocapacitance: (a) monolayer adsorption pseudocapacitance (underpotential deposition), (b) surface redox pseudocapacitance, and (c) intercalation pseudocapacitance

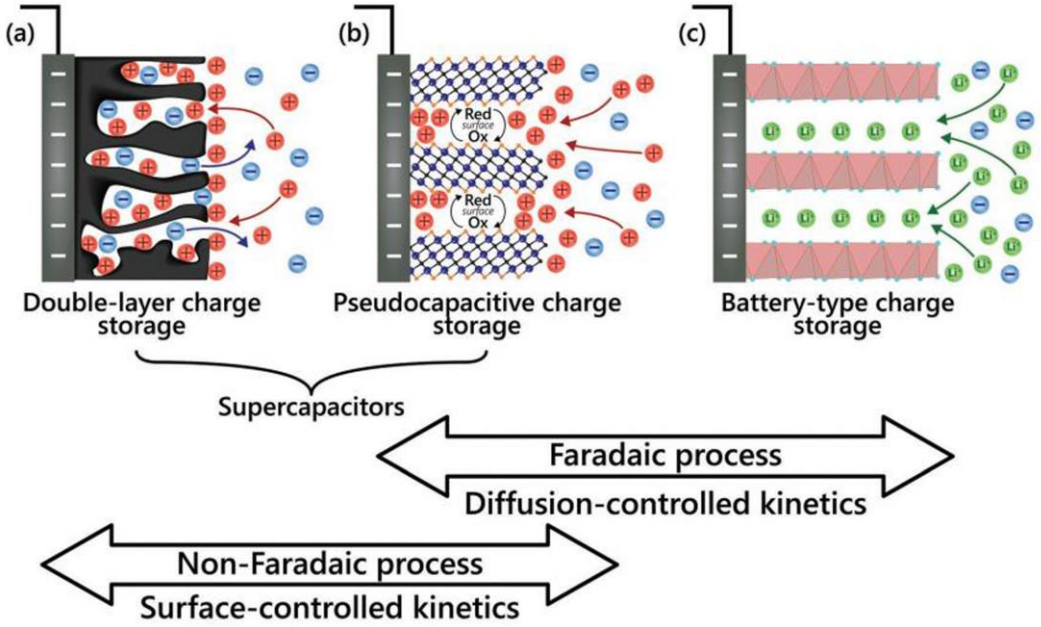

Figure 1.8 Illustration of the electrode processes occurring at (a) electrical double-layer capacitive, (b) pseudocapacitive, and (c) faradaic electrodes

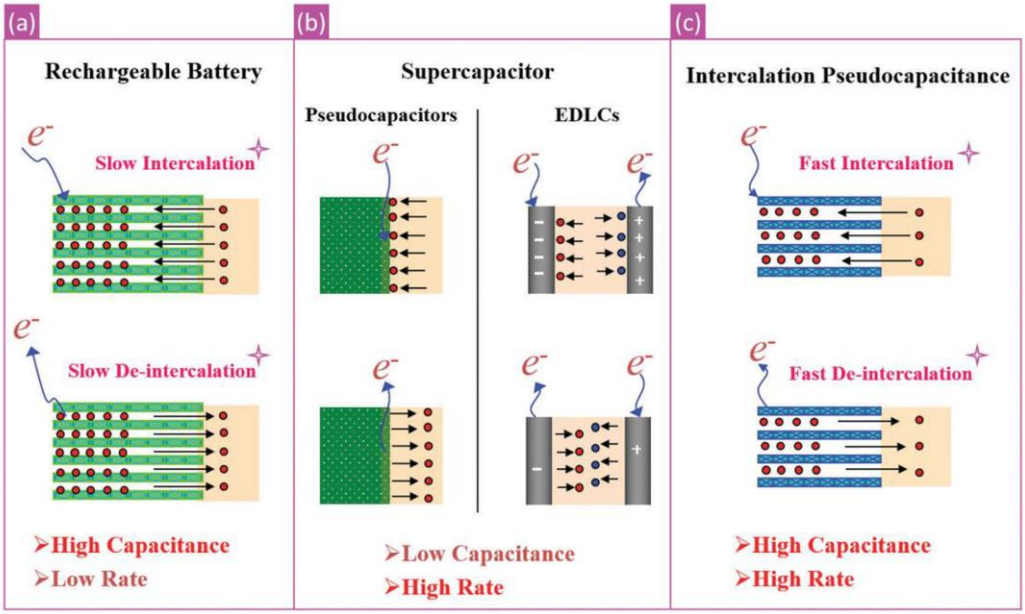

Figure 1.9 Schematic of different charge storage mechanisms. (a) Charge storagemechanism of rechargeable battery, (b) Charge storage mechanism of supercapacitor, (c) Charge storage mechanism of intercalation pseudocapacitance

As discussed above, different ion and charge transport paths are produced when the redox reaction involving both surface intercalation/de-intercalation and sorption/desorption of electrolyte cations takes place due to the dispersive nature of the electrode composites. As a result, understanding the structural parameters (e.g., size, crystalline structures, and morphology) and the kinetic parameters (e.g., scan rate, potential window) during the redox reactions process is important, which is related to the charge storage mechanism. In 2007, Dunn *et al.*[18] put forward that by kinetics analysis the CV curves distinguished contributions from slow diffusion-controlled processes and capacitive effects. In CV measurements, the total current at a given potential is derived from the capacitive contribution (i_c) and the diffusion controlled contribution (i_d).

$$i_{total} = i_c + i_d \tag{1.9}$$

The capacitive current (i_c) from the EDLC capacitance and pseudocapacitance is proportional to the sweep rate v according to equation 1.5.

$$i_c = k_c v \tag{1.10}$$

In addition, the current (i_d) from diffusion-limited redox reaction is proportional to the square root of the scan rate v.

$$i_d = k_d v^{0.5} \tag{1.11}$$

Therefore, equation 1.9 can be changed into:

$$i_{total} = k_c v + k_d v^{0.5} \tag{1.12}$$

Where the $k_c v$ is capacitive effect and the $k_d v^{0.5}$ is diffusion-controlled contribution. Equation 1.12 can be transformed to:

$$\frac{i_{total}}{v^{0.5}} = k_c v^{0.5} + k_d \quad (1.13)$$

Through plotting $\frac{i_{total}}{v^{0.5}}$ versus $v^{0.5}$, k_c and k_d can be determined. The contributions of capacitive effects and diffusion-controlled to total capacitance are able to quantitatively determine.

In addition, the total current (i_{total}) in the CV curve and the potential scan rate (v) follow the power law relationship, which can be described as:

$$i = av^b \quad (1.14)$$

Where a and b are variable constants.[24] By determining the value of b, we can determine the contribution of diffusion control and capacitive to the total capacitance.

When the b value is close to 0.5, the total capacitance is dominated by the diffusion-controlled faradaic process. When the b value is close to 1, the charge storage process is controlled by capacitive. As the value of b ranges from 0.5 to 1, it proves that the electrochemical process benefits from both capacitive and diffusion-limited redox processes. However, even though Dunn ś method has been widely used to analyze the kinetic performance of materials since it was reported, we need to note that 1) this method could be suitable for low rates CVs according to what Dunn et al. did; 2) it could be wrong to consider the charge storage process controlled by capacitive, and not diffusion, when the b value is close to 1. This could be due to the size effect, i.e. when the size of the material was small enough (nanosize effect; surface process), some battery materials would also show that b is equal to 1. It should also be noted that, although the behavior of intercalation pseudocapacitive was similar to the capacitive or conventional pseudocapacitive behavior, the

electrochemical signature was still close to the battery-type electrode.[16] **Figure 1.10** shows the kinetic analysis of the storage capacity of VSe_2 for sodium ions.[25] **Figure 1.10a** shows the CV curves of VSe_2 at various scan rates, there are four redox peaks. The b values calculated according to equation 1.14 were 0.89, 0.78, 0.84, and 0.93, respectively, suggesting that the charge storage of VSe_2 benefited from both diffusion-controlled and capacitive mechanisms (**Figure 1.10b**). The overall capacity could be divided into two parts: diffusion-controlled and capacitive contributions through equation 1.12 (**Figure 1.10c**) and the detail of each part at different scan rates could be found in **Figure 1.10d**.

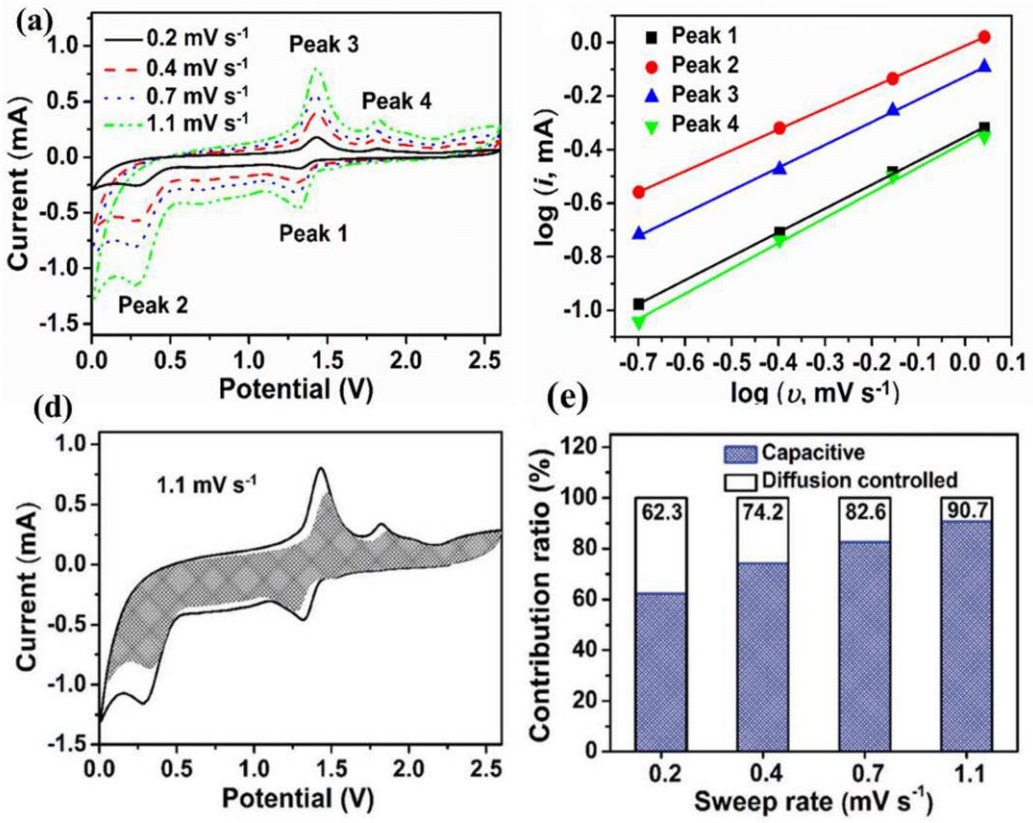

Figure 1.10 (a) CV profiles of VSe_2 at different scan rates and (b) Relationship between log (i) and log(υ) at each redox-peak pair; (c) Capacitive contribution of pseudocapacitive at 1.1 mV/s; (d) The contribution ratio of pseudocapacitive

1.3 Electrochemical testing system

Generally, the test apparatus used to characterize the performance of electrode materials included a three-electrode and two-electrode system. The two-electrode system focuses on characterizing the performance of the full SC devices, while the three-electrode system is typically used to evaluate the electrochemical properties of electrode material.[26] As illustrated in **Figure 1.11**, the test configuration of the two-electrode testing system that is more close to the performance of a cell is comprised of positive and negative electrodes. Based on the types of electrode materials, the SC is classified into symmetric and asymmetric devices. The three-electrode system consists of a working electrode (WE), counter electrode (CE), and reference electrode (RE). The working electrode is normally the material that is being analyzed. The main effect of the counter electrode is to adjust the potential during measurement by supplying the necessary current to balance the reaction that is occurring on the working electrode. In most cases, inert materials such as Pt are often used as counter electrode. The Ag/AgCl, saturated calomel electrode, and Hg/HgO electrode are common reference electrodes. Because of the stability of the material used to prepare the reference electrode, the reference electrode is considered to have an almost constant half-reaction potential. The reference electrode is used to accurately measure the potential on the working electrode with respect to the reference electrode.

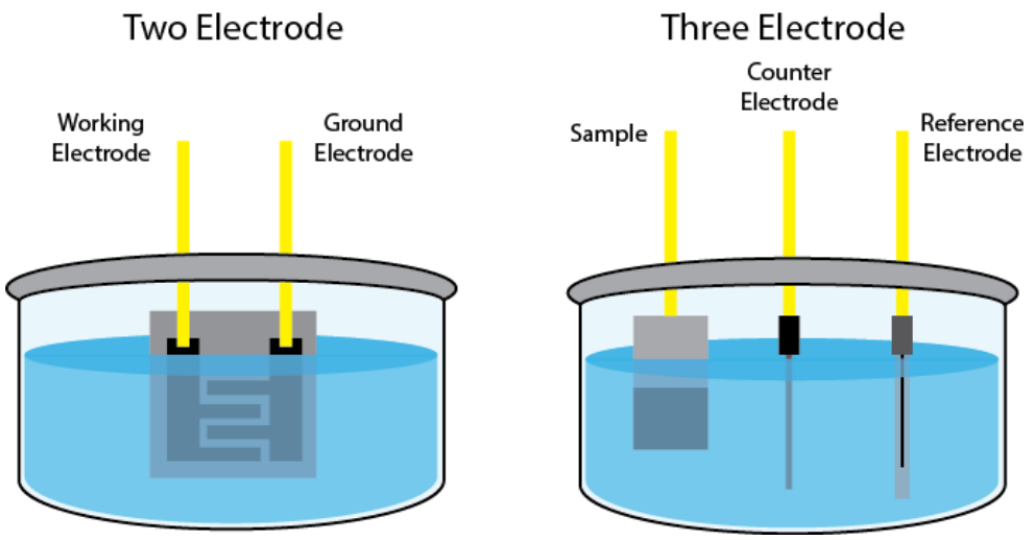

Figure 1.11 Schematic illustration of two and three-electrode measurements for on-chip supercapacitor materials

1.4 Electrochemical experiment evaluation

The electrochemical performance of a single electrode or SC device is examined by the parameters of specific capacitance (F/g), energy density (Wh/kg), power density (W/kg), charging/discharging cycling stability, equivalent series resistance (ESR) and rate capacity. Generally, cyclic voltammetry (CV), galvanostatic current charging-discharging experiments (GCD), and electrochemical impedance spectroscopy (EIS) were used to evaluate the performance of SCs.

1.4.1 Cyclic voltammetry (CV)

CV is a fundamental experiment and the most common electro-analytical technique. Generally, CV measurement is tested in a three-electrode system. A given potential is applied to the working and reference electrodes in a given electrolyte and the signature of the current-voltage behavior of the electrode material under constant

scan rates.[26] The voltage and current vary plotted against the time shown in **Figure 1.12a and 1.12b**. Since the stored charge varies linearly as a function of potential, for ideal SC, the CV shape will be a rectangle, as shown in **Figure 1.12c**. The plot of the current versus the applied voltage of the working electrode is called the cyclic voltammogram curve. However, in most cases, we are in a non-ideal environment, so **Figure 1.13** shows three common CV diagrams. The deformation of **Figure 1.13a** can be attributed to the fact that the electrons in the electrodes or the ions in the electrolyte do not have enough time for transmission to form an electric double-layer capacitance under high scan rate. The electrolyte degradation is the second limitation. There is a limited stable voltage window for a specific electrolyte solution, and the electrolyte solution will no longer be stable if this voltage is exceeded.[26] For example, the water decomposition voltage is 1.23V. If exceeding this voltage, the water will be hydrolyzed into hydrogen and oxygen. The latter one can be attributed to the unique energy storage mechanism of pseudocapacitors.

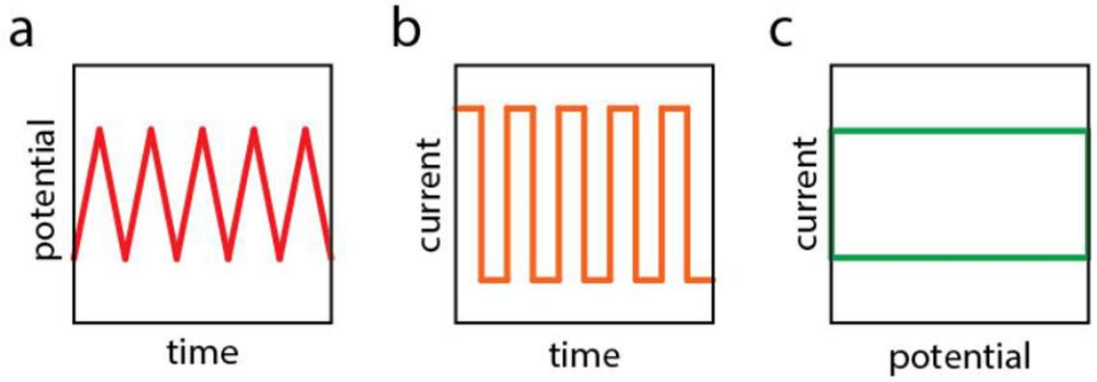

Figure 1.12 (a) Cyclic voltammetry potential sweeps plotted vs. time, (b) The resulting measured current of an ideal SC plotted vs. time, (c) The CV curve, showing the current plotted vs. potential

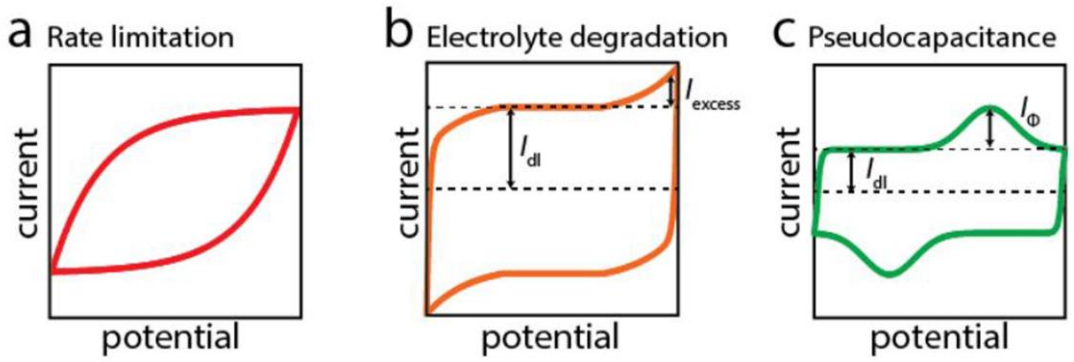

Figure 1.13 Sample SC CV non-idealities: (a) sweep rate limitations, (b) potential window that exceeds electrolyte stability window, (c) pseudocapacitive charge storage

The specific capacitance of the materials can be estimated by CV measurement, as in equation 1.15:

$$C = \frac{\int_{v1}^{v2} idV}{msΔV} \tag{1.15}$$

Where *C* is the specific capacitance (F/g); $\int idV$ is the integrated area of the CV curve; i is the discharge current (A); *m* is the mass loading of active materials on the working electrode (mg); *s* is the scan rate (mV/s); and ΔV is the voltage window (V); V_2 and V_1 are the high and low potential limits of CV tests.

1.4.2 Galvanostatic charge-discharge (GCD)

The galvanostatic charge-discharge test is the most efficient method to determine the capacitance of the electrode. Compared to the cyclic voltammetry method, the galvanostatic charge-discharge test used a constant current during the testing process, which can more accurately reflect real world performance. The typical formula used to calculate the capacitance is as follows.

$$C = \frac{I\Delta t}{m\Delta V} \tag{1.16}$$

Where *I* is a constant current (A), and Δt is the discharge/charge time (s).

The same as the CV curves, for an ideal EDLC, the GCD curves show a linear voltage versus time response (a triangular-shaped profile) during current charging/discharging (**Figure 1.14a**). And, in reality, the deformation of the curve can be attributed to the limitation of the electrolyte stability and the energy storage mechanism of the electrode (**Figure 1.14b**). The effect of high current density is the same as the high scan rates in the CV that result in a short time for transfer of ions in the electrolyte and electrons in the electrode. On the one hand, an extremely low current density induces a leakage current and self-discharge. On the other hand, an instantaneous voltage drop is observed when converting from charging to discharging, known as the IR drop, coming from the ohmic resistances that are related to the internal resistance.

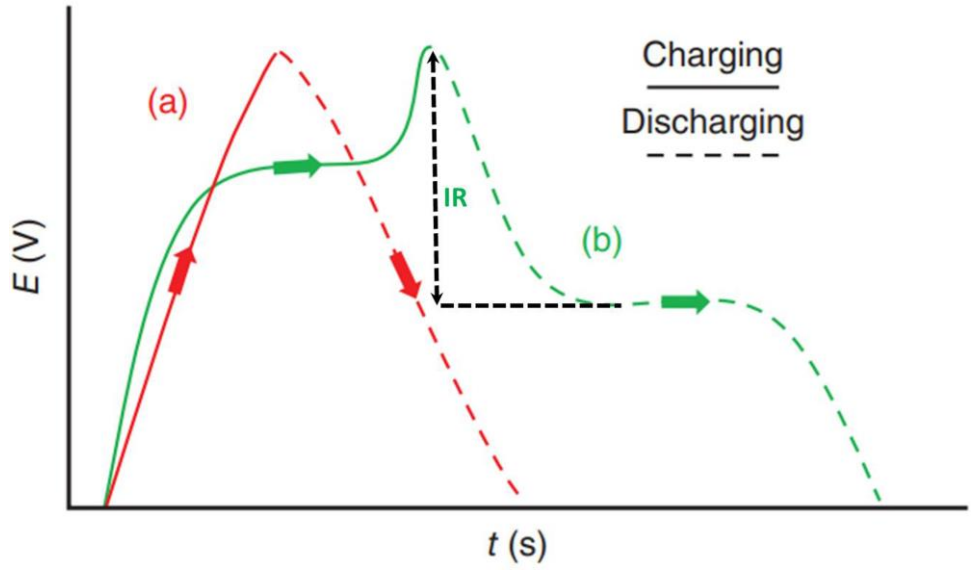

Figure 1.14 Galvanostatic charge-discharge plots of (a) EDLC and (b) pseudocapacitive material

1.4.3 Energy and power density

The energy density is the amount of energy stored per mass/unit volume of active material. For a full device, the energy density and power density are two key parameters to evaluate the overall performance of a supercapacitor. The energy density (*E*, Wh/kg) is obtained by

$$E = \frac{C\Delta V^2}{2} \tag{1.17}$$

The energy released per unit of time is the power density, which is used to evaluate the speed of the charge and discharge.

$$P = \frac{3600E}{\Delta t} \tag{1.18}$$

Where, *P* is the power density (W/kg).

The maximum power density (P_{max}) is related to the equivalent series resistance (ESR), which is comprised of the electrode resistance, the electrolyte resistance, and the diffusion resistance. The relationship is presented as follows:

$$P_{max} = \frac{V_{max}^2}{4R_s} \tag{1.19}$$

Where, *V* is the maximum voltage and R_s is the ESR. Here, the ESR is deduced from the following equation：

$$\mathrm{ESR} = \frac{\Delta V}{|I_{charge}|+|I_{discharge}|} \tag{1.20}$$

Where $\triangle V$ represents the voltage difference. I_{charge} and $I_{discharge}$ represent the magnitude of the charge and discharge currents, respectively. Normally, electrochemical impedance spectroscopy (EIS) is an effective method to determine the ESR.

The ragone plot has been widely employed to compare the performance of

different energy storage devices in **Figure 1.1**. For a fuel cell and a battery, it has high energy density, while the capacitor reveals a high power density. For an ideal device, the ragone plot should locate in the right-up hand side with high energy density at high power density.

1.4.4 Electrochemical impedance spectroscopy (EIS)

EIS measurement is a popular way to provide information about the impedance of SC at the open-circuit potential by applying a small voltage amplitude (5-10 mV) corresponding to a wide range of frequencies (10^{-2}-10^{5} Hz). The EIS can be plotted into the Nyquist plot and the Bode plot.[27] The most commonly used is the Nyquist plot that includes three regions 1) in higher frequency regions, the internal resistance caused by the intrinsic electronic resistance of the active material and current collector, the electrolyte ionic resistance and the contact resistance between the active material and the current collector; 2) the high to medium frequency is the second part, indicating the charge transfer resistance. 3) the vertical line in the low-frequency region corresponding to the Warburg impedance arising from ion diffusion at the electrolyte and the electrode interface reflects the capacitive behavior of the electrode.[28, 29] **Figure 1.15** is a typical Nyquist plot showing a semicircle in the higher frequency region and a spike in the lower frequency region. The V_2O_5 network showed the smallest semicircle compared to the stacked V_2O_5 and V_2O_5/PPy core/shell network, which could be attributed to the network structure that is beneficial to accelerate charge transfer. The V_2O_5/PPy core/shell network showed the

steepest straight line corresponding to the lowest Warburg impedance. This result is explained by the high conductivity after PPy coating.[30]

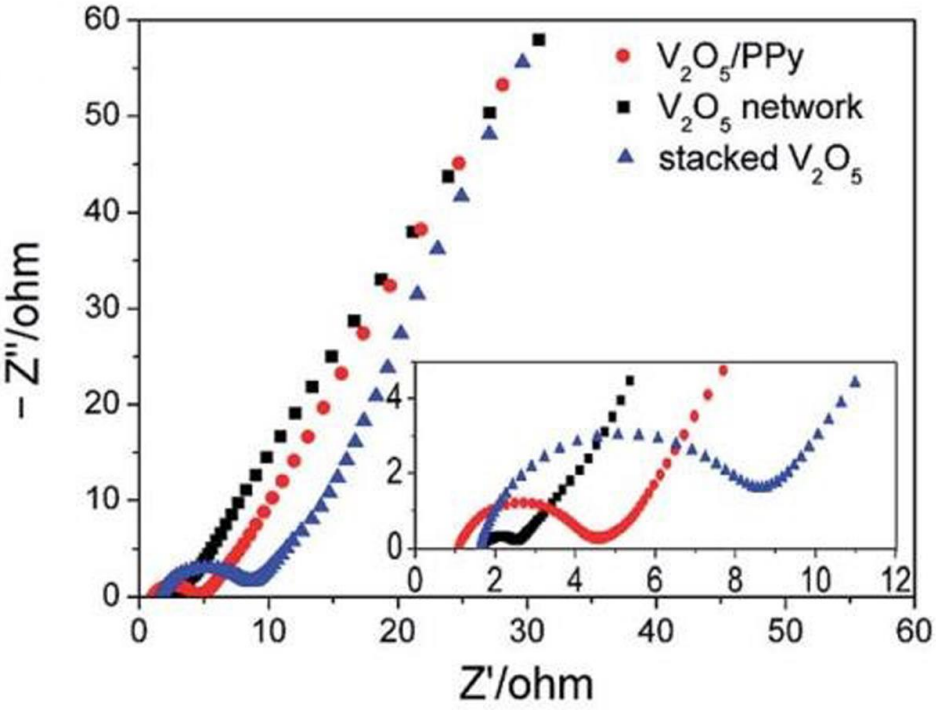

Figure 1.15 Nyquist plots of the three prepared different material electrodes

1.5 Synthetic method

To improve the SC performance, various synthesis techniques were applied to control the structures and properties of the materials for suitable electrochemical SC applications. Synthetic methods include the electrochemical deposition, sol-gel method, hydrothermal/solvothermal method, and microwave-assisted method.

1.5.1 Electrochemical deposition

The benefits of the electrochemical deposition method are low cost and precise control of the film thickness, as well as on the rate of polymerization. The working

principle of electrochemical deposition is based on the electrochemical redox reaction. When the electric current flows through the electrolyte, the ions with positive charge transfer to the cathode. After reaching the substrate, the ions obtain electrons from the substrate (cathode) and form materials through a reduction reaction. It is widely used to prepare conducting polymers (CPs) (such as polyaniline (PANI), Poly(3,4-ethylenedioxythiophene) (PEDOT), polypyrrole (PPy)), exfoliated graphene, and various metal oxides/hydroxides based composite electrode materials (**Figure 1.16**).[31-41]

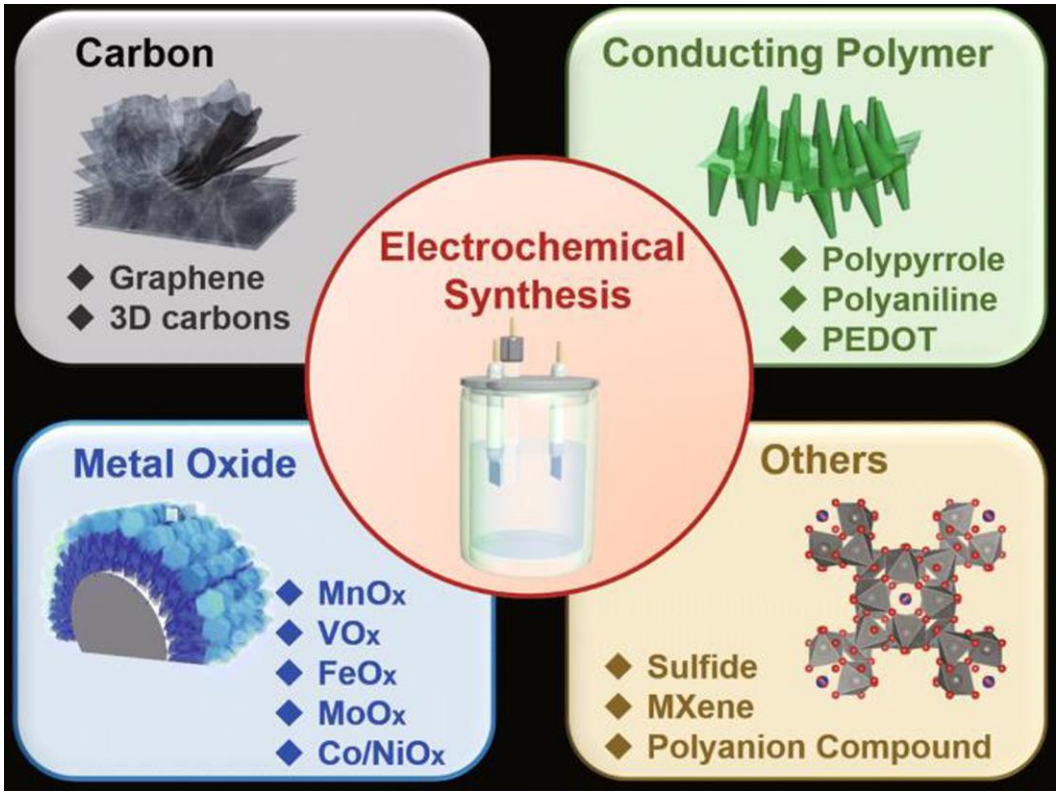

Figure 1.16 The materials prepared by electrochemical deposition method

1.5.2 Sol-gel method

Sol-gel technology is a method for converting precursor solutions into inorganic solids through chemical synthesis that provides a convenient way to prepare materials

with higher purity and uniformity. The precursors mix in a liquid (water or alcohol)，then the acid or a base as the active agent is added. The particles in the solution (sol) gather together and connect together to form an integrated network (gel) under specified conditions. We can concisely summarize the sol-gel technique into three steps: (i) preparation of precursor solutions, (ii) formation of the intermediates sol, (iii) transformation from sol to gel. The structures of electrode material can be modified by controlling the surfactants, solvents, reaction time, and temperature, to produce a better electrochemical behavior. This method has been widely used to prepare transition metal oxides (TMOs).[42-44]

1.5.3 Hydrothermal/solvothermal methods

The hydrothermal/solvothermal method is a low-temperature sintering process. When water as the solvent, we call it hydrothermal synthesis, and the water is instead by other solvents, as solvothermal synthesis. The hydrothermal/solvothermal method was widely used to synthesize the material due to simple to implement environmental friend, and scale-up and it was an ideal method to prepare high purity, crystalline, quality designer particulates with good chemical and physical characteristics. The basic principle of hydrothermal synthesis is based on the relationship between dissolution and crystallization. The specific operation method is that undissolvable compounds and solvents are put in a steel pressure vessel, also called a Teflon vial, and heated to 60 °C ~ 260 °C, at the same time the pressure of steel pressure vessel is gradually increased, and then precursors are dissolved and crystallized again with

slowly cooling. Due to low equipment requirements, many SC electrodes have been manufactured using this method, such as various transition metal oxides and metal oxide composites.[45-49] However, the reaction is carried out in a closed space, so the change of the reactants cannot be observed intuitively, thus increasing the difficulty of controlling the reaction process. In addition, the long reaction time and requirements for high temperature and high pressure also limit the application of this method.

1.5.4 Microwave-assisted method

The microwave-assisted method can overcome the disadvantages of hydrothermal and solvothermal methods, providing a simple and fast method for the fabrication of nanosized crystalline material. Microwave consists of electromagnetic radiation, which lies between radio waves and infrared frequencies, with relatively large wavelengths of 1 mm to 1 m and the frequency is from 0.3 to 300 GHz. The electromagnetic field has two components, the electric field component and the magnetic field component. Therefore, microwave heating can be divided into electric field heating which heats the substance by ionic conduction and dipolar polarization and magnetic field heating that the principal mechanisms are eddy current losses, hysteresis losses, magnetic resonance losses, and residual losses.[50] Compared to conventional heating, microwave heating directly applies the microwave energy to the molecules of the reaction mixture, energy transfer occurs in less than a nanosecond, causing a rapid rise in temperature. It reduces the reaction times from days to hours to

minutes or seconds. Besides, shortening the reaction time also reduces the occurrence of side reactions, thereby improving the purity and yield of the product. The structure and morphology of the material can be controlled by controlling the applied microwave intensity, the reaction time and the ratio of the substrate. Based on these advantages, the microwave-assisted method technique was acted as the preferred emerging technique for SCs studies nowadays. For example, a variety of porous materials inorganic, complex, and nanocrystalline particles were synthesized by the one-pot method.[51-53] In particular, coupling the microwave and solvothermal method not only can reduce reaction time, but can fabricate desired morphology leading to excellent electrochemical properties of the material.[54, 55]

1.6 Electrolyte effect

The electrolyte, including solvent and salt, is another important constituent influencing the performance of SC. An ideal electrolyte material should include the following characteristics, such as a wide potential window, low resistivity, high electrochemical stability, low solvated ionic radius, low viscosity, low toxicity, low volatility, low cost, and availability at high purity. The energy density is proportional to the square of the cell voltage and the power density is mostly influenced by the electrolyte.[56, 57] The conductivity and temperature coefficient of the electrolyte are also critical to the ESR of the capacitor. Therefore, the interaction between the electrolyte and the electrode material is a major factor that impacts the life-time and self-discharge of energy storage. Up to now, various types of electrolytes have been

widely developed and reported in the literature and can be classified as aqueous electrolytes, organic electrolytes, and ionic liquid electrolytes.

1.6.1 Aqueous electrolyte

Generally, aqueous electrolytes are the most preferred choice in the reporting due to the advantages of high ionic concentration and conductivity, inexpensiveness, lower resistance, non-flammability, safety, small ionic size, and ample proton supply. High conductivity is beneficial in reducing the ESR and power delivery of energy storage. However, when commercial applications are considered, the narrow voltage windows make aqueous electrolytes become a low choice. Normally, the voltage window for aqueous electrolytes is 1.23 V for the acidic or alkaline electrolyte and 1.6 V for the neutral aqueous electrolyte which is restricted by water decomposition.[58] The aqueous electrolytes of H_2SO_4, KOH, NaOH, and Na_2SO_4 are the most frequently used. For instance, the ionic conductivity of 1M H_2SO_4 is 0.8 S/cm at 25 ℃, which is higher than that of organic and IL electrolytes by at least one order of magnitude.[59] The maximum ionic conductivity value of 6M KOH is 0.6 S/cm at 25 ℃.[55] Between various neutral electrolytes, Na_2SO_4 has been the most broadly used neutral electrolyte, providing a wider window than acidic and alkaline electrolytes.

1.6.1.1 Organic electrolytes

The conducting salts are dissolved in organic solvents to prepare the organic solvents, which can provide the high operating potential window between 2.5 and 2.7

V.[60] From the perspective of commercial SC market, the higher operating potential window of organic electrolytes is a wise choice to improve the energy density of SCs compared to aqueous electrolytes. However, the performance of SC is still limited by the nature of organic electrolytes.[61] First, the electrolyte needs to be purified from water through the number of purification cycles, increasing the cost and posing a threat of electrode corrosion. Otherwise, the ions size of the organic electrolyte is larger than that of aqueous electrolytes. The number of ions that match the carbon pore diameter material is reduced and the maximum specific capacitance is limited. For instance, acetonitrile is toxic but can dissolve more salts than other solvents, whereas propylene carbonate has the merits including a wide operating voltage, a wide operating temperature, environmental friendliness, and good conductivity. They are the most widely used organic electrolyte solvents. Among salts, tetraethylammonium tetrafluoroborate, tetraethylphosphonium tetrafluoroborate, and triethylmethylammonium tetrafluoroborate have been widely reported.[62, 63]

1.6.1.2 Ionic liquid electrolytes

The ionic liquid electrolytes exhibit the advantages including non-toxic, high thermal, chemical and electrochemical stability, negligible volatility, non-flammability, wide operating voltage window ranging from 2 to 6 V, but low conductivity less than 10 mS/cm.[64] These characteristics profit from the dual functionality units of ionic liquids including an asymmetric organic cation and a weakly coordinating inorganic/organic anion. They not only participate in conductance, but also act as a

route for dissociation. This special composition of ionic liquids reduces the stability of the crystal lattice and is conducive to a low melting point. Moreover, because the diversity of cation and anion combinations provides a high degree of adjustability of ionic liquids, we can control properties like the melting point, viscosity, voltage window, and conductivity by adjusting their structure. In this regard, ionic liquids are called "design solvents". The anions (PF_6^-, BF_4^-, $TFSI^-$, or FSI^-) coupled with imidazolium, pyrrolidinium, and aliphatic quaternary ammonium salts are the main ionic liquids studied for energy storage applications. Some results show that the use of ionic liquids as an electrolyte is a good way to improve the performance of electrochemical capacitors.[59, 65]

1.7 Electrode material

The electrode material occupies a key position in the SCs device, which directly determines the characteristics of the SCs. Hence, the selection and design of electrode materials and their modification are very important in order to develop advanced high-performance SCs. Based on the principle of two energy storage mechanisms: EDLCs and pseudocapacitors, the electrode material should possess the following conditions:

1) High specific surface area, which increases the contact area between the electrolyte and the active material facilitating rapid ion transfer;
2) High conductivity, which reduces the charge transfer resistance;
3) High thermal and chemical stability, which impact the stable cycling ability;

4) Desirable electroactive sites, which benefit for ions intercalation/de-intercalation;
5) Low cost and environmentally friendly.

A large number of electrode materials have been studied, in which we can divide them into two subsections comprising EDLC (carbon-based materials) and pseudocapacitor materials (metal oxide and conducting polymers).[66-69]

1.7.1 EDLCs materials

EDLCs materials store the energy based on the pure electrostatic charge process, which strongly depends on the surface area, pore-size distribution, pore shape, and and surface functionality of the electrode materials, which gives a general rule to choose the SC electrode materials. Carbon-based materials have the advantages of easy availability, easy processing, large specific surface area, non-toxicity, good electronic conductivity, high chemical stability, and wide operation temperature range. They widely meet the requirements of EDLC materials.[70] Under normal conditions, a larger specific surface area of carbon-based materials provides a more effective contact area and enhances the charge accumulation capacity between the electrode and the electrolyte interface, leading to higher specific capacitance.[71, 72] However, the relationship between surface area and capacitance is nonlinear. Because the appropriate electrode pores size in different electrolytes will affect the maximum capacitance. For organic electrolytes, the size of the electrolyte ions is larger than that of aqueous electrolytes, so the pore size of 0.4 or 0.7 nm shows more charged activity in aqueous media, and the pore size above 0.8 nm is more suitable for organic

electrolytes. Hence, the pore size of the electrode should be considered. In addition, surface functionalization of electrode materials is also an effective strategy for improving the performance of the electrode material. The introduced surface functional groups or heteroatoms, on the one hand, can improve the hydrophilicity of the material and heighten the wet ability, on the other hand, it may participate in the faraday redox reaction to increase the total capacitance.[73] This section describes several common carbon-based materials.

1.7.1.1 Activated carbon (AC)

Activated carbon (AC) is the most widespread used electrode material for SC due to the low cost, easy synthesis, and high useable specific surface area (1000-2000 m^2/g). Abundant carbon sources come not only from synthetic precursors such as polymers but also from natural renewable resources (coconut shells wood, pitch, coal, or coke), and the relatively low cost and mature industrial production processes make activated carbon the preferred material for commercial applications. As we all know, the porous structure of AC can advance the surface area and facilitate ion transport, bringing a high rate capability and high power density. Nevertheless, the wide pore size distribution from micropores (<2 nm) to macropores (>50 nm) and random connected micropores hinder the performance of activated carbon.[74] Because the transport of electrolyte ions can be slow down by improper pore size, which limits the energy and power density. For example, when the pore size of activated carbon is less than 2 nm, electrolyte ions are almost inaccessible, especially in organic electrolytes.

To obtain an activated carbon material that matches the pore size of the electrolyte ion and has a high surface area, various synthesis methods are studied. Lota G *at el* modified the porous structure and chemical features of the commercial carbon surface by KOH treatment at 850℃. The effective surface areas of reactivated materials reached 1300-1500 m^2/g compared with activated carbons 700-1000 m^2/g leading to three times capacitance value than the raw carbon. The capacitance value of this material in the aqueous electrolyte was higher than that of the aprotic electrolyte (1M $(C_2H_5)_4NBF_4$/AN), because the ion size of the aqueous electrolyte was more applicable to the pore size of the material.[75] Active carbon treated by pyrolysis of a natural cellulose-based precursor (banana fibers) that has a high surface area of more than 2000 m^2/g. Zinc chloride and KOH acted as pore-forming agents that were used to form the pore structure and modify the morphology of the electrode. The electrochemical performance advanced showing a columbic efficiency of ~88 % at 500 mA/g with 500 cycles.[76]

1.7.1.2 Carbon nanotubes (CNTs)

The carbon nanotube (CNT) is a one-dimensional (1D) nanostructure made by rolling planar graphene sheet, and the more surface area is offered by the tubular structure than solid structures. According to the way of wrapping a cylinder, nanotubes are categorized as an armchair (n, m = n), zigzag (n, m =0) and chiral (n, m), where n, m are the index of vectors in the x, and y directions, called chiral indices. The carbon nanotube can be divided into single-walled nanotube (SWCNT) and

multi-walled nanotube (MWNT) depending upon the number of graphene layers present in the carbon nanotube. **Figure 1.17** displays different types of carbon nanotubes.[77] The sp^2 bonds in the carbon nanotube give it high tensile strength and elasticity, which is more conducive to resisting changes in the volume of material during charge and discharge, thereby improving the cycle stability. Contrasted with active carbon (AC), CNTs exhibit a lower equivalent series resistance (ESR) due to the open interconnected mesopores, allowing the electrolyte ions to diffuse easily into the mesoporous network. Since the power density is determined by the overall resistance of the components. It dragged a lot of attention from researchers due to its inherent high electrical conductivity, high surface area, good mechanical, thermal and chemical stability. CNT has been a significant development in electric energy storage.[78-80] However, the small specific surface area (<500 m^2/g) gives a low energy density value of CNTs. In order to have an important breakthrough in the new generation of SCs, combining pseudocapacitance materials (metal oxides or conductive polymers) with CNTs is a widely studied method. With the rapid development of wearable, portable, and miniaturized electronic, the flexible energy storage devices are ever-growing demands nowadays. The ultrathin CNT film decorated with MnO_2 nanosheets was used to fabricate the stretchable SC by Wang Q in 2019.[81] CNT-MnO_2 nanosheet as the positive electrode and CF@$FeSe_2$ nanonuts as the negative electrode, the asymmetric supercapacitor (ASC) displayed a wide operation window (0-1.7 V), high energy density (29.84 Wh/kg, at a power density of 571.3 W/kg), and good capacity retention after 8000 cycles in the two electrode

system (**Figure 1.18**). 3D N-doped CNT was synthesized by the plasma-enhanced chemical vapor deposition method, which provided higher porosity and larger surface area. Then, N-doped CNT substrate and current collector, polyaniline (PANI), was coated on the N-doped CNT by electrodeposition. The core-shell/CNT-PANI electrode showed high rate capability, with a specific capacitance of 359 F/g at 4.95 A/g.[82]

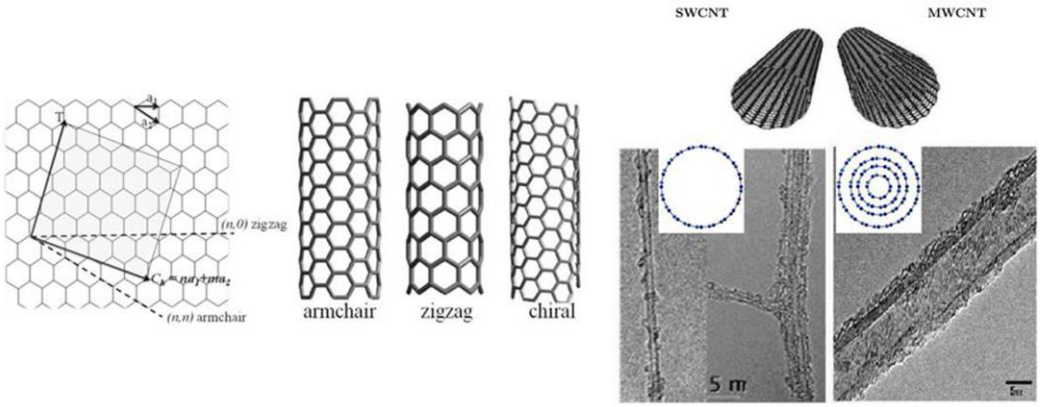

Figure 1.17 Different types of carbon nanotubes

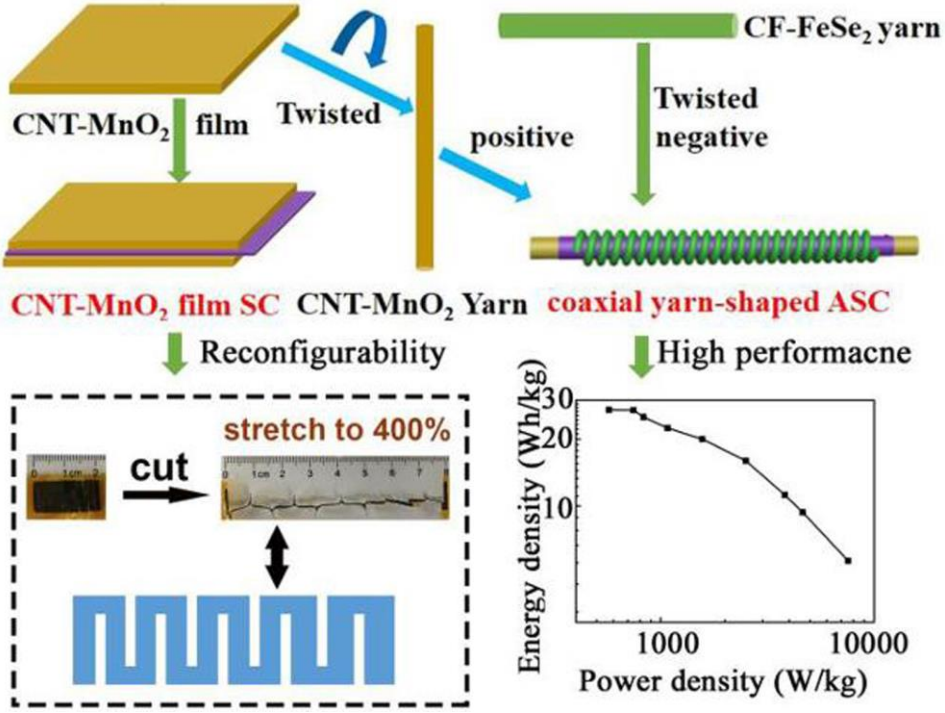

Figure 1.18 Fabrication of coaxial yarn asymmetric supercapacitor

1.7.1.3 Graphene

Graphene with thickness on the atomic scale and carbon atoms with sp^2 bonded is a two-dimensional (2D) layered honeycomb nanostructure that is the basic building block of other carbon materials, as illustrated in **Figure 1.19**.[83] The layered structure of graphene reduces the thickness of the electrode, which reduces the diffusion distance of electrolyte ions. Another advantage of the graphene layered structure is that it can make full use of both sides of the layered structure to with high surface to volume ratio. The ion transport kinetics is improved by the honeycomb nanostructure with an open pore system. Compared to AC and CNT, graphene as an electrode material reduces the dependence on the pore size distribution, which is suitable for increasing the rate capability of the electrode. It has gained significant attentions due to the large theoretical surface area, superior electrical conductivity, good electrochemical stability, outstanding intrinsic strength. However, the van der Waals interaction between adjacent layers makes graphene easy to restacking, thereby increasing the capacity loss. To avoid this shortcoming, the preparation of a composite of metal oxide and graphene and the doping of electron donors and acceptors with graphene seemed to be a good solution. Rakhi RB reported that metal oxides/graphene (SnO_2/GN, MnO_2/GN, and RuO_2/GN) improved the capacitance performance of GN due to the influence of spacers and redox reactions.[84] Chee WK fabricated polypyrrole/graphene oxide/zinc oxide (PPy/GO/ZnO) nanocomposite by electrochemical polymerization. The supercapacitor, PPy/GO/ZnO nanocomposite as electrodes, which combined the pseudocapacitance of polypyrrole and zinc oxide with

the EDLC capacitance of graphene, showed high energy (10.65 Wh/kg) and power density (258.26 W/kg) at 1 A/g.[85]

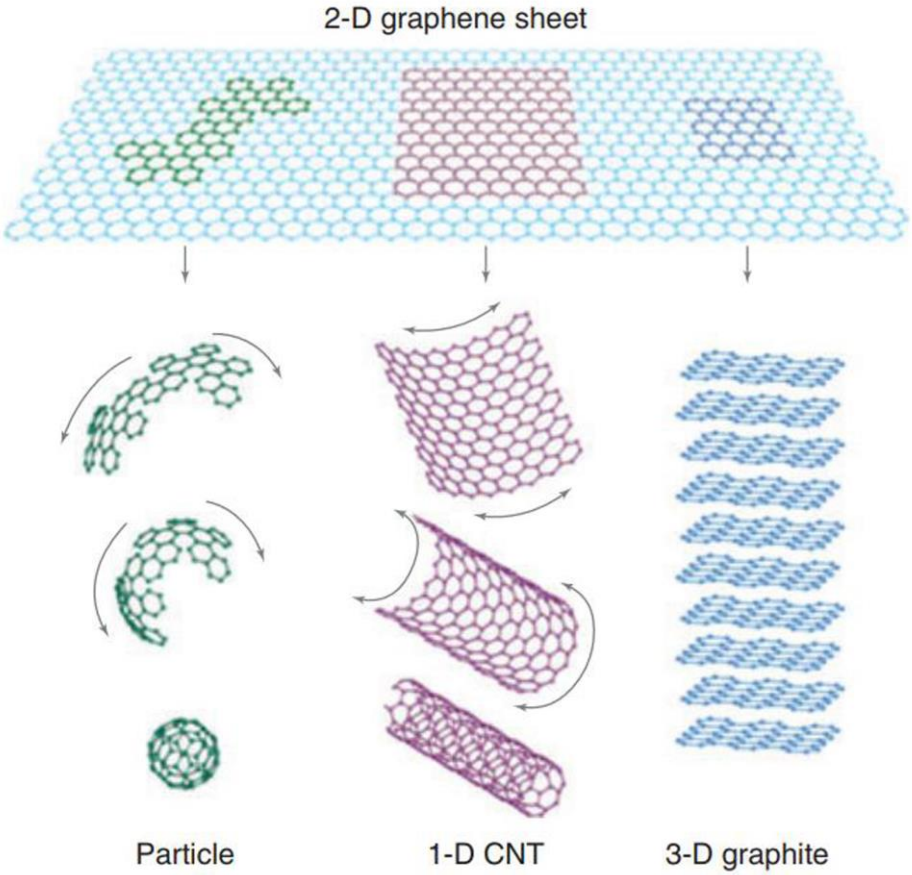

Figure 1.19 Illustration of 2D graphene sheet as the building blocks for other carbon materials such as particle, 1D CNT, and 3D graphite

1.7.2 Pseudocapacitor materials

Compared with EDLC materials, pseudocapacitor materials that store the energy through both the faradic and non-faradic processes show much higher special capacitance. Pseudocapacitor materials include mainly conducting polymers and metal oxide.

1.7.2.1 Metal oxide

Relative to various electrode materials, TMOs (transition metal oxides) with high theoretical capacitance have acted as a candidate electrode material for developing advanced performance SCs. Various transition metals have been extensively studied to improve the specific capacitance and energy density of SC in the past few decades, such as nickel oxide (NiO), cobalt oxide (Co_3O_4), manganese oxide (MnO_2), vanadium oxide (V_2O_5) etc. **Figure 1.20** shows the theoretical capacitances of the different TMOs based on cyclic voltammograms.[86] Unfortunately, easy agglomeration at high mass loading, poor rate capability, and low conductivity properties are the shortcomings of the TMOs, which hinder the further development of this kind of material. Therefore, extensive researchers have tried to incorporate the conductive materials with the TMOs or to change of the structural properties of the TMOs using various synthetic techniques to overcome these drawbacks.

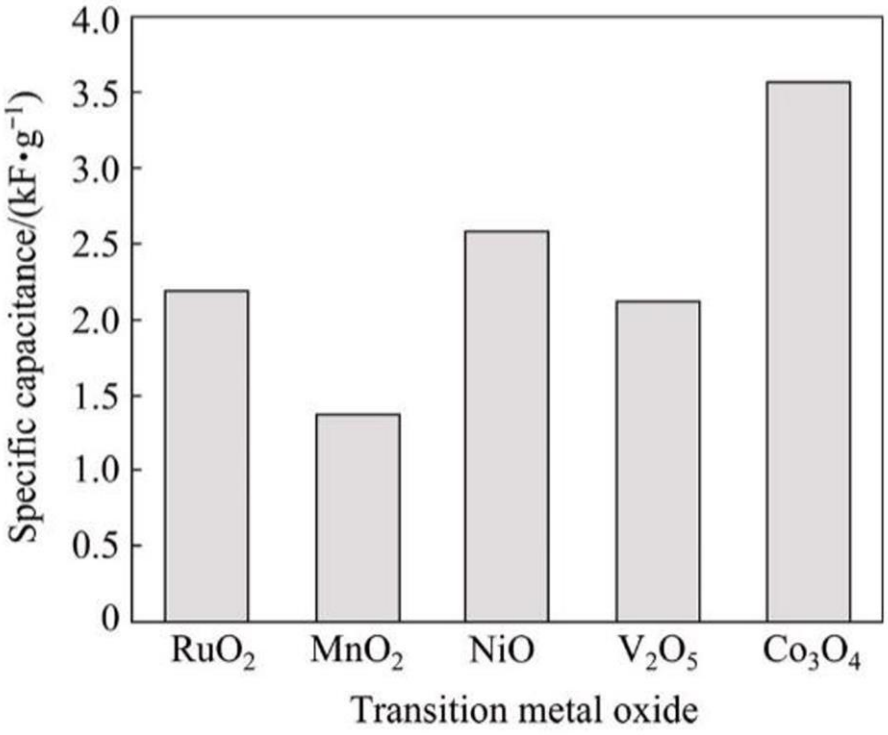

Figure 1.20 The different TMOs theoretical capacitances based on cyclic voltammograms

1.7.2.1.1 Manganese oxide (MnO_2)

MnO_2 has been widely applied in catalysis, biosensor, and energy storage due to its properties including low cost, low toxicity, eco-friendly, and abundance. The theoretical specific capacitance of MnO_2 is 1370 F/g based on one-electron redox reaction calculations. Transfer of protons and/or cations in various manganese valence states (Mn(III)/Mn(II), Mn(IV)/Mn(III) and Mn(VI)/Mn(IV)) provides a wide electrochemical window (about 0.9 ~ 1 V) . The mechanism can be expressed as:

$$MnO_2 + C^+ + e^- \leftrightarrow MnOOC$$

It shows the bulk faradaic reactions based on the insertion of electrolyte cations ($C^+ = H^+$, Li^+, Na^+, and K^+).[87, 88] Another describes the surface faradaic reaction of

the MnO_2 electrode as follows:[89]

$$(MnO_2)_{surface} + C^+ + e^- \leftrightarrow \ (MnOOC)_{surface}$$

The charge storage capabilities of manganese dioxide related to the crystal structures. The size of the tunnels controlled the intercalation of cations, and the microstructure mainly impacts the cycling stability. The available surface area and conductivity of the structure are limited by the crystalline. If the crystalline is high, the surface area is low, and the conductivity will increase, *vice versa*.[90] For example, Brousse et al. reported the capacitance of 1D tunnel structure (β- or γ-MnO_2) which stored the charge by the surface faradaic reaction depended on the Brunauer-Emmett-Teller (BET) surface area of the crystalline material. The 2D birnessite structure showed high capacitance values compared to the 1D and 3D tunnel structure. Since the charge storage process was controlled by both the surface cation insertions and partial cation insertions. The electrochemical performance of the 3D tunnel structure (λ-MnO_2) was somewhere between.[91] **Figure 1.21** shows some structure of MnO_2.[92]

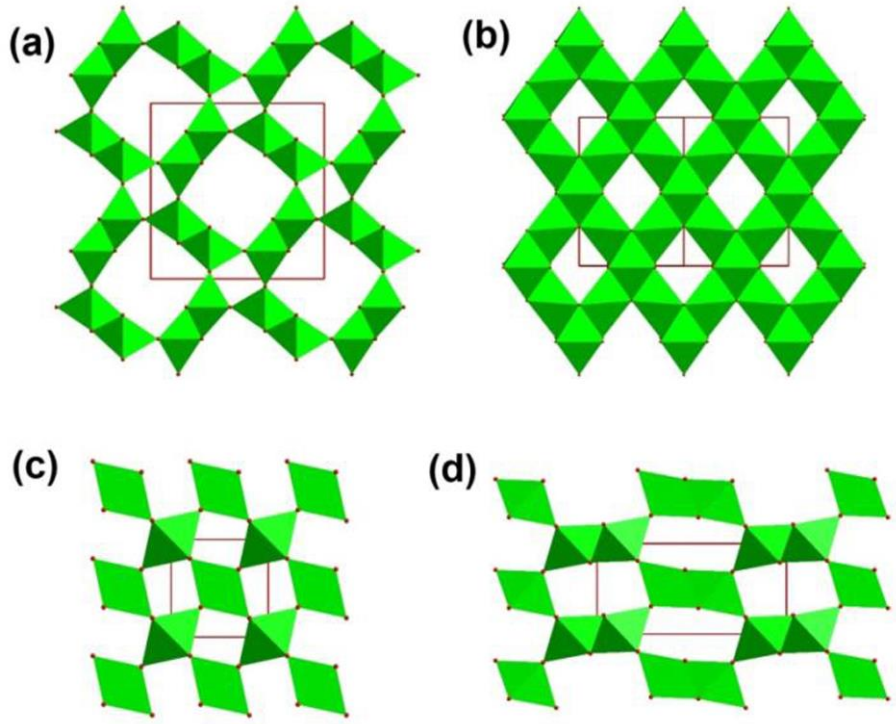

Figure 1.21 Four polymorphs of MnO_2: (a) α-MnO_2, (b) λ-MnO_2, (c) β-MnO_2, and (d) γ-MnO_2

In order to further improve the electrochemical performance of MnO_2, the strategies by incorporating other conductive materials with MnO_2 were developed to overcome the low electrical conductivity defect of MnO_2. The electrical conductivity of MnO_2 is about 10^{-5}-10^{-6} S/cm. Chen et al. reported ternary hybrid sphere powders ($Ni(OH)_2$-MnO_2-RGO) which showed a high specific capacitance of 1985 F/g due to the synergetic effect between three i) The $Ni(OH)_2$-MnO_2 constituent contributed to the pseudocapacitance output ii) The insertion of graphene sheets could inhibit excessive self-aggregation of hybrid nanosheets, improve electron transport of binary metal oxide/hydroxide and increase the specific surface area.[93]

1.7.2.1.2 Nickel oxide (NiO)

Among the various metal oxides, nickel oxide (NiO) is regarded as a promising pseudocapacitors electrode material, due to its environmental friendliness, high theoretical capacitance (2584 F/g), non-toxicity, good thermal and chemical stability, and a high surface area behavior. The structure of NiO is cubic with the space group *Fm3m* and similar to the rock-salt structure NaCl with octahedral Ni^{2+} and O^{2-} occupation.[94] NiO based electrode is applied in SC applications, the common requirements are as follows:

1) The oxide should be conductive;

2) The metal should have two or more oxidation states and can coexist within a certain potential range;

3) It should have a high specific surface area;

4) The electrolyte ions can freely intercalate/de-intercalate in the lattice on reduction /oxidation;[95]

Based on two main theories: 1) electrochemical reactions occur between NiO and NiOOH, 2) firstly, NiO changes to Ni(OH), then the energy storage process occurs between $Ni(OH)_2$ and NiOOH; the redox reaction of NiO or $Ni(OH)_2$ in the alkaline electrolyte determines the performance of nickel oxide-based pseudocapacitor electrode materials, as equations.

$$NiO + H_2O \leftrightarrow NiOOH + H^+ + e^-$$

$$NiO + OH^- \leftrightarrow 2NiOOH + e^-$$

Normally, more researchers prefer the first theory, but the second theory is more

suitable for practical applications.[55]

As mentioned above, NiO has high theoretical specific capacitance. However, the poor electrical conductivity (from 0.01 to 0.32 S/m) limits the performance of material.[94] Moreover, the energy storage process happens on or near the surface area of the electrode, so the structural features of the electrode occupied a vital role. Recently, most reports have focused on improving SC performance by modifying material construction or forming composites. Gao *et al.* prepared a binderless 3D Ni@NiO nanowire membrane by a facile filtration method and then calcination with an appropriate annealing temperature.[96] The ultralong Ni nanowire as the "core" was a highly efficient current collector and the NiO layers were "shell" served as an active material. The binder-free method was used to prepare the electrode, which could guarantee a well-welded and good conductive network to each other. With the benefit of this design, the interface electrons could transfer from NiO to Ni at a high rate. As a result, the SC showed a wonderful rate capability. 96.1% of the original capacitance was reserved at a high current density (2.048 A/cm^2). 1D NiO nanofibers were synthesized by Natarajan *et al.* and presented a reversible capacitance of 248 F/g at 1 A/g.[97] Wang *et al.* reported that NiO nanoparticles grown on highly conductive 3D graphene foam by pulsed laser deposition process, with ozone as the oxidant (**Figure 1.22**).[96] The composite showed interconnected pore structures that were conducive to rapid electron and ion transportation resulting in a high specific capacitance and a superb rate capability (68% of capacity was maintained when the current density increased from 2 A/g to 100 A/g). Using the hierarchical porous

N-doped carbon nanotubes as the negative electrode and the NiO/GF as the positive electrode to assemble the asymmetry supercapcitor (ASC) that shown a high power density of 42 kW/kg at an energy density of 32 Wh/kg and outstanding cycling stability. In addition, Das *et al.* prepared NiO/polyaniline-multi-walled nanotube core-shell nanocomposites via an in situ polymerization technique. The core-shell structure was confirmed by TEM (transmission electron microscopy). The study has shown that after NiO and multi-walled nanotube were incorporated into the polymer matrix, the material's supercapacitance value and electrochemical stability were significantly improved.[98]

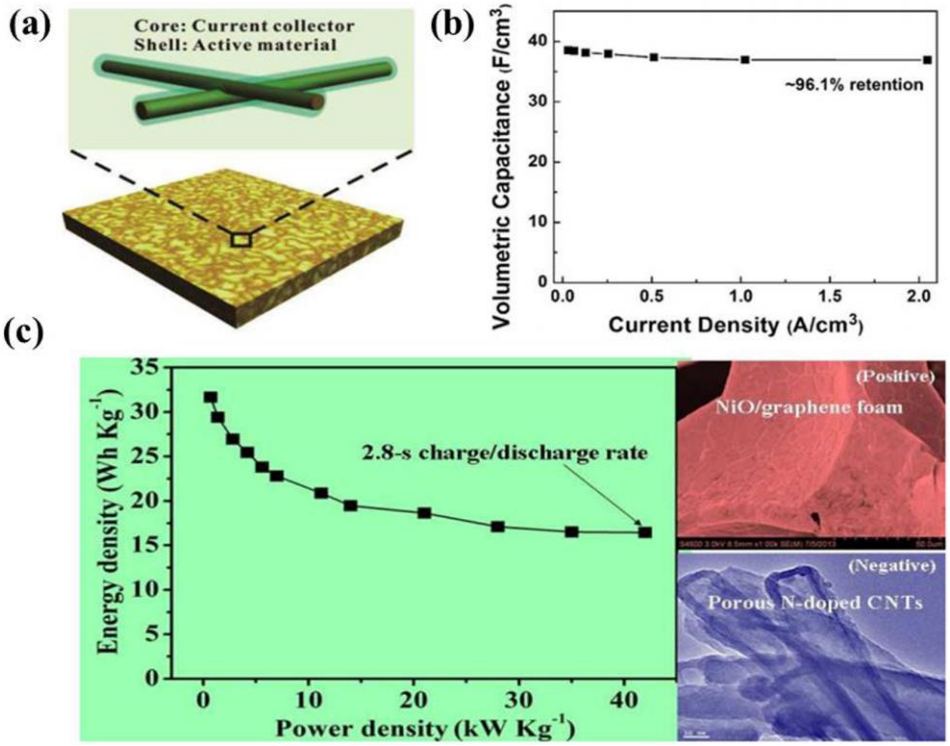

Figure 1.22 (a) 3D free-standing binder-free Ni@NiO nanowire membrane; (b) Volume capacitance with respect to the current density; (c) Energy and power density of the NiO/GF//HPNCNTs asymmetric SC and positive and negative electrode morphology

1.7.2.1.3 Cobalt oxide (Co_3O_4)

The cobalt oxide is a promising electrode material due to the good corrosion resistance, long term performance and good efficiency. The AB_2O_4 spinel structure of cobalt oxide crystallizes in a cubic system with a band gap of ~2.0 eV. The theoretical capacitance is 3560 F/g in alkaline solutions. The charge storage mechanism depends mainly on the pseudocapacitors. The redox reaction occurs not only on the surface but also throughout the bulk and can be explained as equations.[99, 100]

$$Co_3O_4 + OH^- + H_2O \leftrightarrow 3CoOOH + e^-$$

$$CoOOH + OH^- \leftrightarrow CoO_2 + H_2O + e^-$$

Therefore, the electrochemical properties of cobalt oxide are controlled by the surface area, alignment of the nanocrystalline phases, and morphology. Recently, different strategies have been applied to synthesize various forms of Co_3O_4 (microspheres, nanosheets, nanowires, nanorods, nanotubes as well as thin films) in order to increase the capacitance value of supercapacitor. In 2009, Gao. Y *et al.* prepared Co_3O_4 nanowire arrays using a template-free method, where nickel foam acted as a support and current collector. The sufficient contact between the nanowires and the foamed nickel ensured the utilization of active materials and avoided the trouble of using auxiliary conductive materials and adhesives. The increased surface area and the unique porous structure of the nanowires resulted in a high specific capacitance of 746 F/g at 5 mA /cm.[101] Wang. G *et al.* reported the Co_3O_4 nanorods with textured aggregations of nanocrystals showed a specific capacitance of 280 F/g at 5 mV/s.[102] However, the low potential window (0.45 V) and poor cycling ability

limited practical applications. Recent studies have been concentrated on coupling Co_3O_4 nanoparticles with different electrode materials to overcome these drawbacks. Kim *et al.* improved the cycling stability of Co_3O_4 by preparing the composite electrode ($CoMnO_2$/VGCNFs) using the thermal decomposition method. The high specific capacitance of 630 F/g at 5 mV/s displayed, which was attributed to the use of VGCNFs that decreased the electron transport distance between the electrode and electrolyte. This work has shown outstanding cycling stability, retaining 95 % of the initial capacitance over 10000 cycles.[103]

1.7.2.1.4 Vanadium oxide (V_2O_5)

Vanadium oxide with a layered structure, high theoretical specific capacity (2120 F/g), and multiple oxidation states that yield surface/bulk redox reactions resulting in a wide working window is regarded a good electrode material.[104] The large interlayer spacing of vanadium oxides allows easy insertion/extraction of cations with larger ionic radii (Na^+ and K^+).[105, 106] However, poor structural stability (due to high dissolution in liquid electrolyte) and low conductivity (10^{-3}-10^{-5} S/cm) are greatly hinder long-term cycling performance and capacitive performances. Considerable efforts have been devoted to mitigating these limitations. Perera. SD and coworkers combined carbon nanotube (CNT) with V_2O_5 nanowire to enhance electrochemical supercapacitors performance. The nanocomposite paper electrode (anode) and the high surface area carbon fiber electrode (cathode) used to assemble the coin cell type supercapacitor displaying a power density of 5.26 kW/kg and an

energy density of 46.3 Wh/kg.[107] But this kind of composite cannot prevent vanadium dissolution. The flexible V_2O_5@PPy core-shell nanowire membrane was fabricated by Qian. T *et al.* using in situ interfacial reactive template method. V_2O_5 as reactive (oxidative) templates guided polymerization of PPy shell uniform sheathed on V_2O_5 matrix. The binder-free and conductive additive-free V_2O_5@PPy core-shell flexible membrane shorted the distance of ion/electron transport, increased electrical conductivity and enlarged electrode/electrolyte contact area. The PPy shell can not only increase electrical conductivity, but prevent the dissolution of V_2O_5. The electrochemical activity and stability of V_2O_5 improved significantly.[30]

1.7.2.2 Conducting polymer

Conducting polymers have received an enormous amount of interest in academia and industry due to their ease of fabrication, low-cost preparation, and unique electrical properties which are between the semiconductor and metals. Compared to carbon-based electrode materials and metal oxides, conducting polymers have relatively higher electrical conductivity (10^4 S/cm) and capacitance (1000 F/g), making them an attractive choice as the electrode materials.[108-110] The commonly used conducting polymer including polyaniline (PANI), polythiophene (PTH), polypyrrole (PPy), polyacetylene (PA), and poly(3,4-ethylenedioxythiophene) (PEDOT). The structures as illustrated in **Figure 1.23**.[111] **Table 1.2** showed the theoretical and experimental capacitance data and conductivities of few selected conducting polymers.[111, 112]

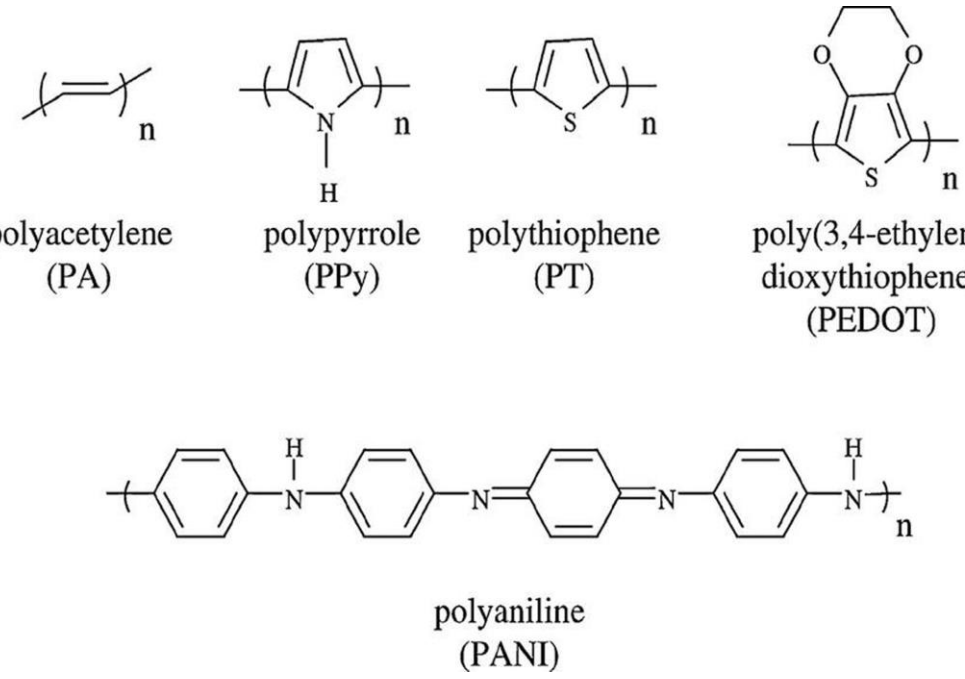

Figure 1.23 Chemical structures of common used conducting polymers

Table 1.2 The theoretical and experimental capacitance data and conductivities of few selected conducting polymers.

Conducting polymer	Theoretical capacitance (F/g)	Experimental capacitance (F/g)	Conductivity (S/cm)	Dopant level	Potential range (V)
PANI	750	240	30-200	n, p	0.7
PPy	620	530	10-7500	p	0.8
PTh	485	-	10-1000	p	0.8
PEDOT	210	92	0.4-400	n, p	1.2

The conducting polymer stores the charges through the reduction-oxidation process that occurs not only on the surface but also throughout the entire bulk. When oxidation occurs (doping), ions transfer to the polymer backbone. When reduction occurs (de-doping), the ions release back into the solution. There are two types of

conductive polymer configurations in the redox process：n-doped cations and p-doped anions. The equations are given below:[113]

$$P \leftrightarrow P^{n+}(A^-)_n + ne^- \text{ (n-doped)}$$

$$P + ne^- \leftrightarrow (C^+)_n P^{n-} \text{ (p-doped)}$$

Where P presents the polymer; A is the anion; C is the cation. **Figure 1.24** showed the charging/discharging mechanism of the conducting polymer with two doping states.[103] Conductivity can be controlled and adjusted by controlling the chemical structure of the conductive polymer. The high energy density of SC is considered due to the charge-transfer process. Nevertheless, the redox process leads to structural changes such as swelling and contraction, which limits the stability of the electrode. PANI was the first described conducting polymer in the mid-19th century, which was widely used due to the lightweight, mechanically flexible, and low cost, but limited by structure stability. To mitigate this limitation, different PANI nanostructures and their nanocomposites were engineered by researchers to advance the electric performance of conducting polymer. For example, PANI was prepared by the potentiostatic deposition method showing high stability, power and energy density, and specific capacitance. The improvement in properties can be attributed to the use of hierarchically porous carbon monoliths. The hierarchically porous carbon monoliths with large size and porosity not only acted as a current collector but also had high surface support properties that enabled the PANI to be in closer contact with the current collector. With hierarchically porous carbon monoliths as a template, the prepared PANI provided smaller particle size and more uniformly dispersed on the

support, which facilitated the fast transfer of the electrolyte ions. The composites of PANI with the carbon-based material SWCNT were prepared by Gupta V using electrochemical polymerization to enhance the conductivity of the PANI electrodes. The highest specific capacitance of 485 F/g was obtained.[114] The PANI-MnO_2 composite electrode showed a specific capacitance of 715 F/g and an energy density of about 200 Wh/kg at 5 mA/cm.[115] The electrical conductivity of PPy is 10-500 S/cm. The higher density and flexibility make it more competitive compared to other conductive polymers. The 3D nickel foam as support, the CoO_2@PPy electrode was prepared by anchoring the PPy to the CoO_2 nanowire leading to the pseudocapacitive performance boost of the electrode. The maximum voltage window of the asymmetric supercapacitor device was 1.8 V in which activated carbon film was used as the negative electrode and CoO_2@PPy as the positive electrode. The energy density was about 43.5 Wh /kg. The high power density exhibited 5500 W/kg at 11.8 Wh/kg. These benefits come from the synergetic between CoO_2 and PPy, where PPy provided high conductivity and CoO_2 with ordered mesoporous shorted the ion diffusion pathway.[116] The preparation of PEDOT can be simply achieved either chemically or by electro-polymerization. Liu K *at el* had been successfully electro-polymerized the PEDOT. The cycle life was increased to 70,000 cycles, and the cycle performance was close to that of activated carbon materials.[117] The specific capacitance was about 130 F/g. To get good electrochemical performance, some polymers (Nafion, Poly-tetrafluoroethylene, polyvinylpyrrolidone, Poly-vinylidene difluoride, Sulfonated poly-ether ether ketone,

and polyvinylidene chloride) as binder or additive were added into the electrode material.

In summary, conducting polymers are promising electrodes to advance the electrochemical performances of SCs. But the limitations of poor rate and cyclic stability need to be overcome. Although the strategy of the combination of conductive polymer with the metal oxide/hydroxide/sulfide has successfully achieved this target, there is still a lot of room for improvement in the future.

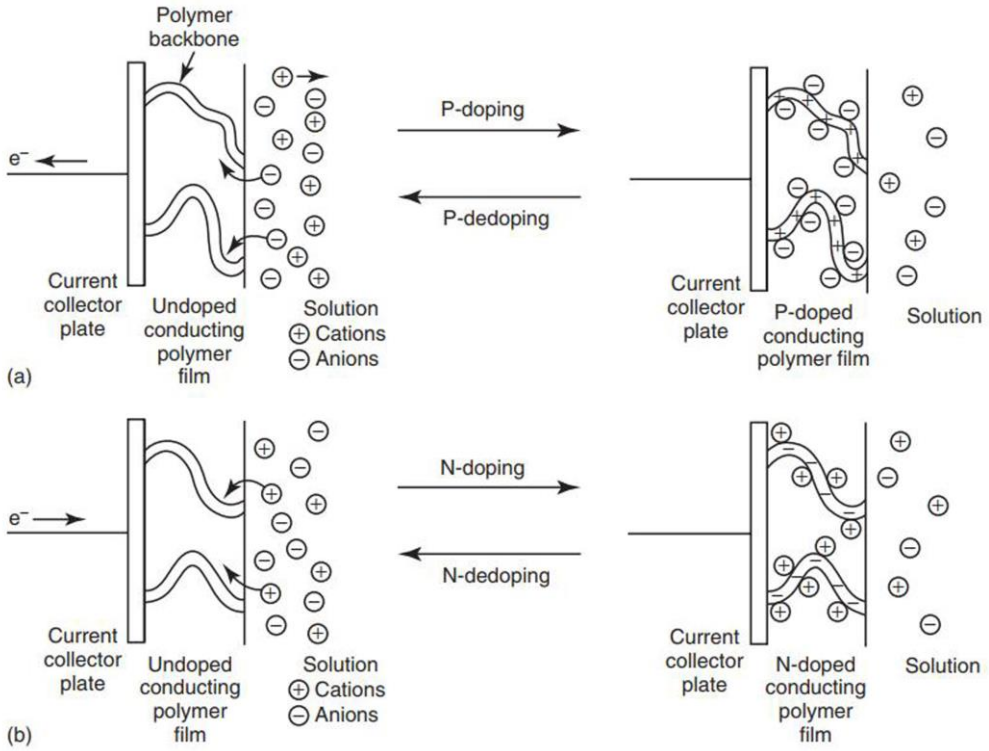

Figure 1.24 Illustration of conducting polymer's charging/discharging mechanism with two doping states: (a) p-doping and (b) n-doping

1.8 Research Objectives and Approach

It can be seen from the above that albeit the application of SCs in energy storage has made great achievements, there are still obstacles to be resolved to meet the

application requirements of high power density and energy density devices, as follows:

1) With regard to the knowledge of energy storage mechanisms, especially the characterization and understanding of electron transport and atomic transport in complex interface processes, there are many unresolved fundamental issues. Understanding the knowledge of ion storage and transport mechanisms of energy storage systems can give us a brief direction to advance the performance of devices.

2) The electrochemical performance of the electrode material is also directly related to the structure parameters of the nanocomposites. However, how to precisely control the morphology and structure of nanocomposites is still a challenge to exploit the SC electrode materials for energy storage applications. Especially for the large-scale synthesis of electrode materials, further consideration should be given to the problems of agglomeration, structural uniformity, and uniform distribution of active materials, which make the problem become more complex.

3) Other than that, considering the requirements of the final application, such as cycle life, specific energy, energy and power density, a reasonable selection of electrode materials and electrolytes should be made. A large number of reports have proved that hybrid composite materials showed better electrochemical performance than that of individual electrode materials. In this case, the synergistic effects of hybrid composite materials should be paid attention. In addition, most of the research mainly focused on the performance of the electrode and ignored the growth mechanism of the electrode, which influenced the morphology.

4) Our ultimate goal is to apply supercapacitors to practical applications, but engineering factors (such as electrode manufacturing, electrolyte choice, membrane separator, and packaging) have not been well established. For commercial applications, research on simple, green, and low cost-effective manufacturing technology is important.

The goal of this work is to find a low production cost and green electrode material with high electrochemical performance that is fabricated by a high facile, large-scale, green, low-cost, and high effective method.

Chapter 2: The microwave facile synthesis of NiO_x@graphene nanocomposites for application in supercapacitors: insights into the formation and storage mechanisms

Abstract: Recently, the strategy of combining carbon-based materials with metal oxides to enhance the electrochemical performance of electrodes has been a topic of great interest, but research focusing on the growth and charge storage mechanisms of such hybrid electrodes has rarely been conducted. In this work, a simple, reproducible, low-cost, and fast microwave heating method was used to synthesize NiO_x@graphene nanocomposites. NiO_x@graphene nanocomposites were used as a model system for exploring the growth and charge storage mechanisms of the hybrid electrode materials due to their simple preparation process, good stability, low cost, and high specific capacitance. The effects of reaction conditions (the type of metal precursor and feeding ratio between the nickel precursor and graphene) on the formation mechanism of the electrodes were examined, and it was demonstrated that the microstructure and morphology of the electrode materials were metal precursor-dependent, which was directly related to the electrochemical performance of the electrodes. Our work provides a new affordable approach to the synthesis of, and experimental support for designing, hybrid electrode architectures with a high electrochemical performance for next-generation energy storage devices.

2.1 Introduction

With the rapid evolution of the world that has led to the gradual exhaustion of fossil fuels, global warming, and pollution issues, there is an urgent need to develop a low cost, environmentally friendly, and safe electrochemical energy storage systems (EESs) to support the progress of low-carbon or zero-carbon sustainable economies in the future. A supercapacitor (SC) is a kind of energy storage device that combines the electrochemical properties of a high energy density battery and power density capacitor [55, 118]. Compared to conventional energy storage systems (batteries, capacitors, and fuel cells), SCs are promising candidates for energy storage, due to their fast delivery rate, low cost, lack of memory effect, long life cycle, and the fact that they are lightweight and environmentally safe, which makes them irreplaceable in many portable systems and hybrid electric vehicles [119, 120].

As the core of the SC, the electrode materials occupy a key position and directly determine the electron transport and electrochemical storage characteristics of the SC [11, 121]. Normally, there are three types of electrode materials, including carbon-based materials, metal oxides, and conductive polymers. The carbon-based materials have the advantages of wide availability, a large specific surface area, and a wide operating temperature range. Metal oxides are regarded as a key electrode material due to their properties of simple preparation, high theoretical capacitance, non-toxicity, and good thermal and chemical stability. Unfortunately, their propensity for agglomeration at high mass loading, poor rate capability, weak electrochemical stability, and low conductivity properties hinder their further development.

Conductive polymers with high conductivity and good mechanical properties can effectively compensate for the shortcomings of metal oxides, but their specific capacitance is too low, with a short charge-discharge life cycle. To address these problems, the use of a hybrid electrode material combining different types of materials to advance the electrochemical performance of electrodes has recently been widely proposed. For instance, the multifunctional composite materials of NiO/CNT with an interlinked porous structure were formed using a simple wet chemical method followed by thermal annealing. This composite demonstrated a high supercapacitive performance (878.19 F/g at 2 mV/s) and excellent activity in the oxygen evolution reaction. The device, known as NiO-CNT//Activated Carbon, exhibited a specific energy of 85.7 Wh/kg at a power density of 11.2 kW/kg [122]. The CoO@polypyrrole electrode was prepared by anchoring the polypyrrole to the CoO nanowire, leading to a high specific capacitance (2223 F/g) and power density (5500 W/kg at 11.8 Wh/kg). The pseudocapacitive performance boost of the electrode was derived from the synergistic effect between the mesoporous CoO nanoparticles and the high-conductive PPy [116]. Monolayer graphene/NiO nanosheets were fabricated by Jiang et al. in 2011. The hybrid structure of the composite prevented the aggregation of the NiO nanoparticles, enhancing the stability (95.4% of the initial capacity was retained after 1000 cycles) [123].

Due to the abovementioned developments, the application of hybrid electrode materials in energy storage has led to remarkable achievements. However, there are still obstacles to be resolved in order to meet the application requirements of high

power density and energy density devices, including: (1) the many unanswered fundamental questions about the energy storage mechanisms of electron transport and atomic transport in the interface processes, the answers to which can give us a direction for advancing the performance of the devices; (2) the neglect of the growth mechanism of the hybrid electrode, due to the fact that most research has focused on the performance of the electrodes; and (3) the problem that, although various techniques have been applied to synthesize the electrode materials to date, there is no single method that can meet the requirements of simplicity, green energy, large scale, and cost-effectiveness so as to realize the expected practical application goals.

Nickel oxide (NiO) is regarded as an excellent material for broad use in gas sensors, catalysis, batteries, and SCs due to its theoretical high specific capacity, high chemical/thermal stability, and the fact that it is environmentally friendly and inexpensive [124-127]. Up to now, the differences in the morphology and structure of the NiO materials (nanoflowers, nanoparticles, nanoplates, and mesoporous structure) have been produced by various methods [128-131]. However, these materials have limitations, including a low specific capacity for practical application in supercapacitors, poor conductivity, a propensity for aggregation during the preparation process, and structural instability. Presently, two approaches are widely used to solve these problems: doping foreign atoms, and hybridization with carbonaceous nanomaterials [132-135]. NiO_x@graphene composites, as electrode materials, have many advantages, such as their simple preparation process, good stability, low cost, and high specific capacitance [136-138]. NiO_x@graphene is a

sound model system that can be used to explore the growth and charge storage mechanisms of the hybrid electrode materials. In this work, we attempt to revisit NiO_x@graphene composite materials and to explore the growth mechanisms and synergistic effects of the hybrid materials, providing experimental evidence to further improve the electrochemical performance of hybrid electrode materials in the future. A simple, reproducible, affordable, and fast microwave heating method was used to anchor the NiO_x to the surface of the graphene, due to its time-saving advantages, capabilities of uniform heating, and controllable process. The electrochemical behavior of the NiO_x@graphene composites was investigated using cyclic voltammetry (CV), galvanostatic charge-discharge (GCD), and electrochemical impedance spectroscopy (EIS) tests. The structure and morphology of the NiO_x@graphene composites were characterized by X-ray diffraction (XRD) and scanning electron microscopy (SEM).

2.2 Experimental

2.2.1 Material Characterization

Scanning electron microscopy (Thermo Scientific Apreo FE-SEM, Waltham, MA, USA) and transmission electron microscopy (TEM, FEI Tecnai F20, Lausanne, Switzerland) were used to determine the morphology and microstructure of the powder samples. Powder X-ray diffraction (PXRD) patterns with a Cu target (45 kV, 40 mA) were carried out on Philips X'pert MPD (Philips, Eindhoven, Netherlands) in the 2θ range from 20 to 80, with a scan speed of 0.06◦/min to resolve the phase and

crystal structures of the materials. The electrochemical performance was measured using a CH Instrument (CHI 760D, Austin, TX, USA) potentiostat with 'Electrochemical Analyzer' software (version 15.03). The stability tests were performed using an Arbin Instrument (version 4.21). The chemical composition of the powder samples was investigated by energy-dispersive X-ray spectroscopy (EDS, EDAX Instruments, Thermo Scientific Apreo FE-SEM, Waltham, MA, USA). The elemental valence state of the thus-prepared samples was determined by X-ray photoelectron spectroscopy (XPS, Kratos XSAM 800, Thermo Scientific Apreo FE-SEM, Waltham, MA, USA). The specific surface area and pore size distribution were obtained from a N_2 adsorption-desorption analysis conducted at 77 K on Quadrasorb SI. The specific surface area was calculated by the Brunauer-Emmett-Teller (BET) method, and pore size distribution was obtained from desorption plots by a Barrett-Joyner-Halenda (BJH) analysis.

2.2.2 Materials

All chemicals and reagents were used without further treatment or purification. N,N-dimethylformamide was supplied by Macron Fine Chemicals (Sanborn, NY, USA). Poly (vinylidene fluoride), carbon black, and nickel (II) hydroxide ($Ni(OH)_2$) were prepared according to the previous literature [139]. A nickel (II) acetate tetrahydrate ($Ni(Ac)_2$ $4H_2O$) and nickel nitrate hexahydrate ($Ni(NO_3)_2$ $6H_2O$) were offered by Alfa Aesar (Burlington, NJ, USA). Sodium hydroxide was purchased from TCI America (KITAKU, Tokyo, Japan). Graphene was acquired from Magnolia Ridge

Inc. (Magnolia, TX, USA).

2.2.3 Preparation of the NiOx/Graphene Nanocomposite

A certain proportion of metal precursors ($Ni(OH)_2$, $Ni(Ac)_2 \cdot 4H_2O$, or $Ni(NO_3)_2 \cdot 6H_2O$) and graphene (25 mg) were added into a glass vial and mixed with a high-speed mixer at a speed of 2000 rpm for 2 min. Subsequently, the mixture was transferred to a domestic microwave oven (Panasonic NN-SN733B, 2.45 GHz, power 1250 W). Finally, the reactor was spontaneously cooled to room temperature and the product of the NiO_x@graphene composite was collected. During the microwave irradiation process, graphene acts as a good microwave absorber and thermally conductive layer, providing heat to promote the conversion of the metal precursor to metal oxide. The formation mechanism of NiO_x can be described as follows. Firstly, the metal precursor nanoparticles undergo intense heating when microwave energy is applied, resulting in molecular collisions. At this stage, the amorphous nuclei are formed, but the sizes of the nanoparticles are small. Following this stage, aggregation/self-assembly is caused by van der Waals interactions, leading to larger particles. Finally, the aggregate directional growth forms a specific crystal orientation and morphology due to differences in the respective surface energies. **Figure 2.1** illustrates the process of the synthesis of the NiO_x@graphene composites. In order to study the influence of the reaction conditions on the electrochemical performance, the type of metal precursor and feeding ratio between the nickel precursor and graphene were accurately controlled. The details are given in **Tables 2.1-2.3**.

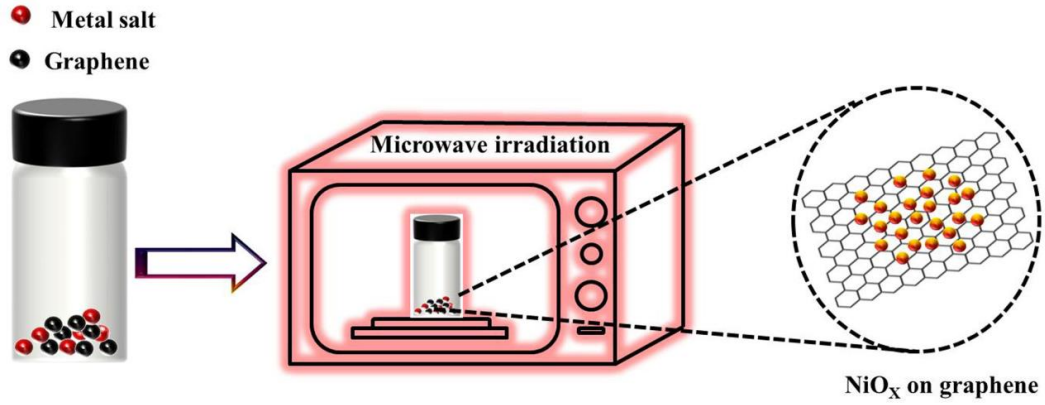

Figure 2.1 Illustration of the microwave synthesis of the NiO_x@graphene composites

Table 2.1 Operation conditions for synthesizing NiO_x@graphene

Sample	G^a (mg)	$Ni(OH)_2$ (mg)	NiO_x^b (mg)	Microwave power (W)	Heating time (min)
NiO_x@GR-A1	25	61.8	49.8	1250	5
NiO_x@GR-A2	25	46.4	37.4	1250	5
NiO_x@GR-A3	25	30.9	24.9	1250	5

[a] Mass of graphene.

[b] Mass of NiO_x calculated according to the nickel precursor.

Table 2.2 Operation conditions for synthesizing NiO_x@graphene

Sample	G^a (mg)	$Ni(Ac)_2$ $4H_2O$ (mg)	NiO_x^b (mg)	Microwave power (W)	Heating time (min)
NiO_x@GR-B1	25	165.8	49.8	1250	5
NiO_x@GR-B2	25	124.4	37.4	1250	5
NiO_x@GR-B3	25	82.9	24.9	1250	5

[a]Mass of graphene.

[b]Mass of NiO_x calculated according to the nickel precursor.

Table 2.3 Operation conditions for synthesizing NiO_x@graphene

Sample	G^a (mg)	$Ni(NO_3)_2$ $6H_2O$ (mg)	NiO_x^b (mg)	Microwave power (W)	Heating time (min)
NiO_x@GR-C1	25	193.9	49.8	1250	5
NiO_x@GR-C2	25	145.4	37.4	1250	5
NiO_x@GR-C3	25	96.9	24.9	1250	5

[a]Mass of graphene.

[b]Mass of NiO_x calculated according to the nickel precursor.

2.3 Electrochemical Measurements

The electrochemical performance was investigated using galvanostatic charge–discharge (GCD), cyclic voltammetry (CV), and electrochemical impedance spectroscopy (EIS) tests in three electrode cells. The CV curves were measured at a potential window of 0-0.6 V under different scan rates (5-50 mV/s), and GCD tests were conducted at a potential of 0-0.5 V with different current densities (0.5-5 A/g). The EIS analysis was tested with an open-circuit voltage using an AC amplitude of 0.005 V in the frequency range of 10-1 to 105 Hz. The working electrode was fabricated by mixing together the active material, carbon black, and polyfluortetraethylene in an 80:10:10 weight ratio. Then, N,N-dimethylformamide was added to the mixture as a solvent to form the homogeneous slurry, which was coated onto the pretreated nickel foam (1×1 cm^2). The electrode was dried at 60 ℃ for 24 h under a pressure of 20 MPa, and the mass loading of the active material was

about 2 mg/cm^2. The Hg/HgO electrode and platinum sheet (1 × 1 cm^2) were used as the reference electrode and counter electrode, respectively. The electrolyte was a 6.0 M KOH aqueous solution. The specific capacitance value was calculated from the GCD curves according to the following equation [140]:

$$C = I\Delta t / m\Delta V \quad (2.1)$$

Where C is the specific capacitance (F/g); m is the mass loading of the active material in the working electrode (mg); I is the constant current (A); Δt is the discharge time (s); and ΔV is the potential window (V). When the mass in the formula was replaced by the area of the electrode (cm^2), the areal specific capacitance (C_A, F/cm^2) was obtained.

2.4 Results and Discussion

The crystal structures of the NiO_x@graphene composites were characterized by PXRD. As shown in **Figure 2.2**, the peak centered at 2θ = 30.92 in the XRD patterns corresponds to the (002) reflection of graphene (JCPDS card 89-7231). The diffraction peaks appearing at 2θ = 43.5, 50.7, and 74.5 correspond to the (110), (-111), and (111) planes of NiO (JCPDS card 65-7425), respectively. The peaks marked with asterisks correspond to Ni_2O_3 (JCPDS card 14-0481), indicating that different products were produced when different metal precursors were used. Furthermore, the diffraction peaks of NiO_x@GR-A2 were markedly broader than those of NiO_x@GR-B2 and NiO_x@GR-C2, indicating a small crystallite size [141]. The average crystallite dimensions estimated by the Scherrer equation [142], based on

the (200) reflections, are approximately 1.398, 5.935, and 4.202 Å, respectively. The oxidation states of the NiO_x nanoparticles were measured by XPS. In the full survey scan spectrum (**Figure 2.3a**), the C 1s and O 1s peaks located at 285.6 eV and 530.4 eV corresponded to the graphene and the oxygen in NiO, respectively [143]. In the high (Ni 2p1/2), with two satellite peaks at 861.5 eV and 880.3 eV, respectively, indicating the existence of Ni_2O_3 and NiO in the composite (**Figure 2.3b**) [144, 145].

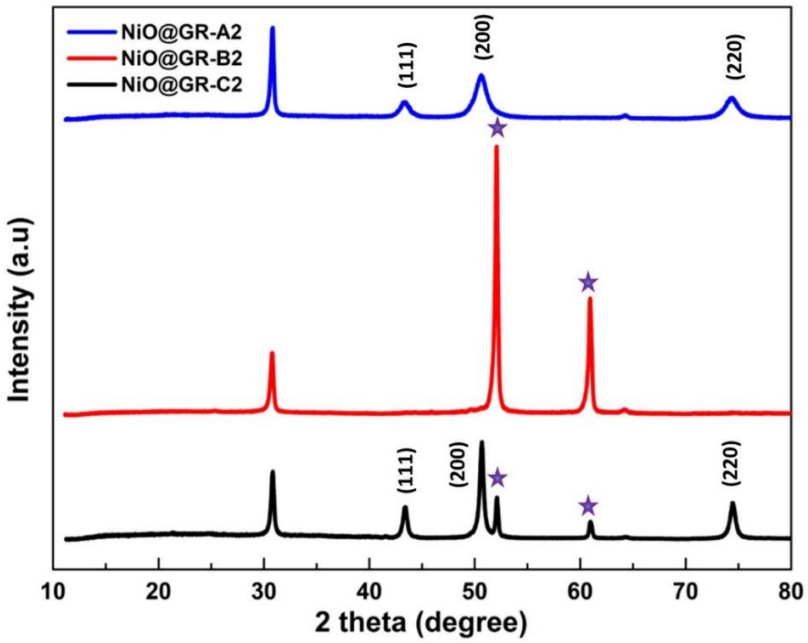

Figure 2.2 XRD patterns for NiO_x@GR-A2, NiO_x@GR-B2, and NiO_x@GR-C2

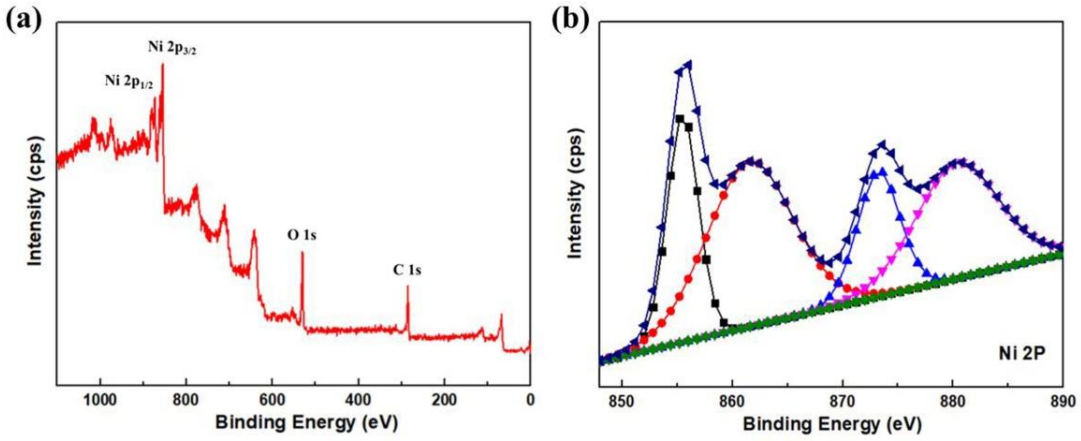

Figure 2.3 (a) XPS spectrum of the NiO_x@GR-C2; (b) High-resolution XPS spectrum of Ni 2p

The microstructure and morphology of NiO_x@graphene were characterized by SEM and TEM. **Figure 2.4** shows the SEM and TEM images of the NiO_x@graphene composites prepared using the different metal precursors, ($Ni(OH)_2$, $Ni(Ac)_2•4H_2O$, or $Ni(NO_3)_2•6H_2O$). When $Ni(OH)_2$ acted as the precursor, the NiO_x exhibited a bulk form with a crumpled surface, as shown in **Figure 2.4a and 2.4b**. When the NiO_x@graphene was prepared using $Ni(Ac)_2•4H_2O$ and $Ni(NO_3)_2•6H_2O$ as the precursors, the corresponding NiO_x exhibited a good flower-like structure (**Figure 2.4d and 2.4e**) and small particles with a fluffy surface (**Figure 2.4g and 2.4h**), individually. The TEM image further illustrates the porous and hollow structures of the NiO_x composites (**Figure 2.4c, 2.4f, and 2.4i**). The different interior structures of the NiO_x composites may arise from the different decomposition temperatures and crystal structures of the metal precursors. The decomposition processes of $Ni(Ac)_2•4H_2O$ and $Ni(NO_3)_2•6H_2O$ generate gas, which is beneficial for the formation of the porous structures. Among the three metal precursors, $Ni(NO_3)_2•6H_2O$ has the highest content of crystallization water, which hinders the absorption of microwave energy by the graphene and slows down the heating process. This leads to the creation of small-sized particles that provide a larger effective contact area. It is clear that the morphology and nanostructure of NiO_x is metal precursor-dependent. Furthermore, the EDS elemental mapping of NiO_x@GR-C2 showed a uniform distribution of carbon (C), nickel (Ni), and oxygen (O) (**Figure 2.5**), which indicates that NiO_x was homogeneously distributed throughout the composite. As is well-known, the uniform distribution of the reacting sites is a key factor in ensuring electrode stability and

electron transfer, which helps to avoid unnecessary resistance and energy loss.

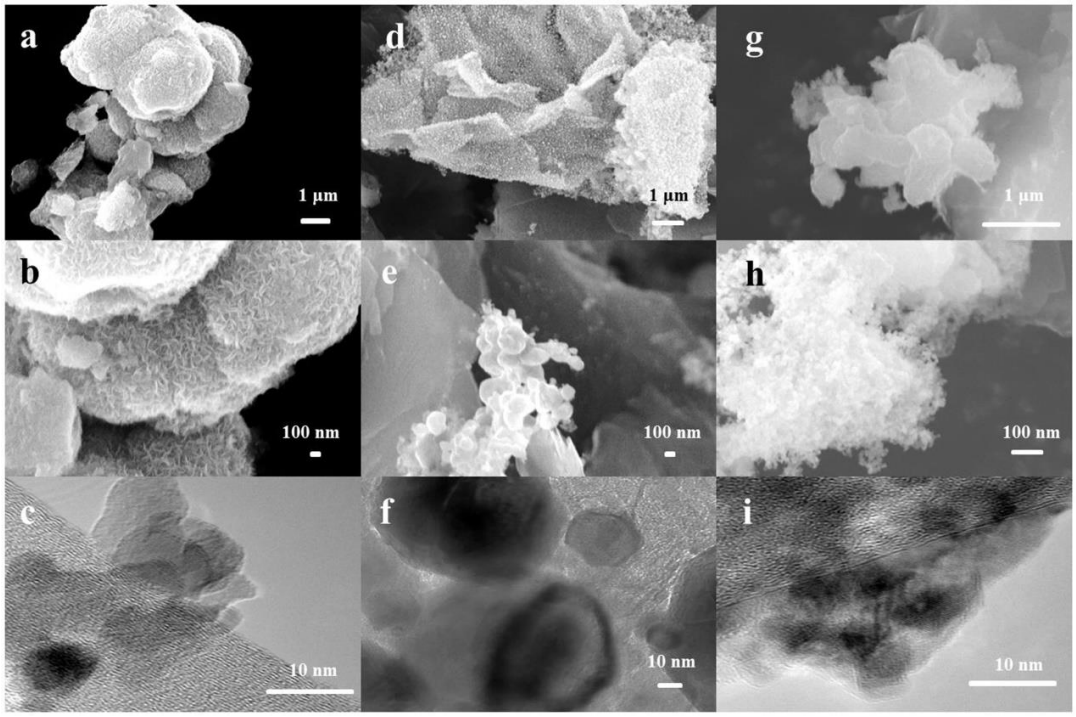

Figure 2.4 SEM images of (a),(b) NiO_x@GR-A2, (d),(e) NiO_x@GR-B2, and (g),(h) NiO_x@GR-C2 at different magnifications. TEM images of (c) NiO_x@GR-A2, (f) NiO_x@GR-B2, and (i) NiO_x@GR-C2

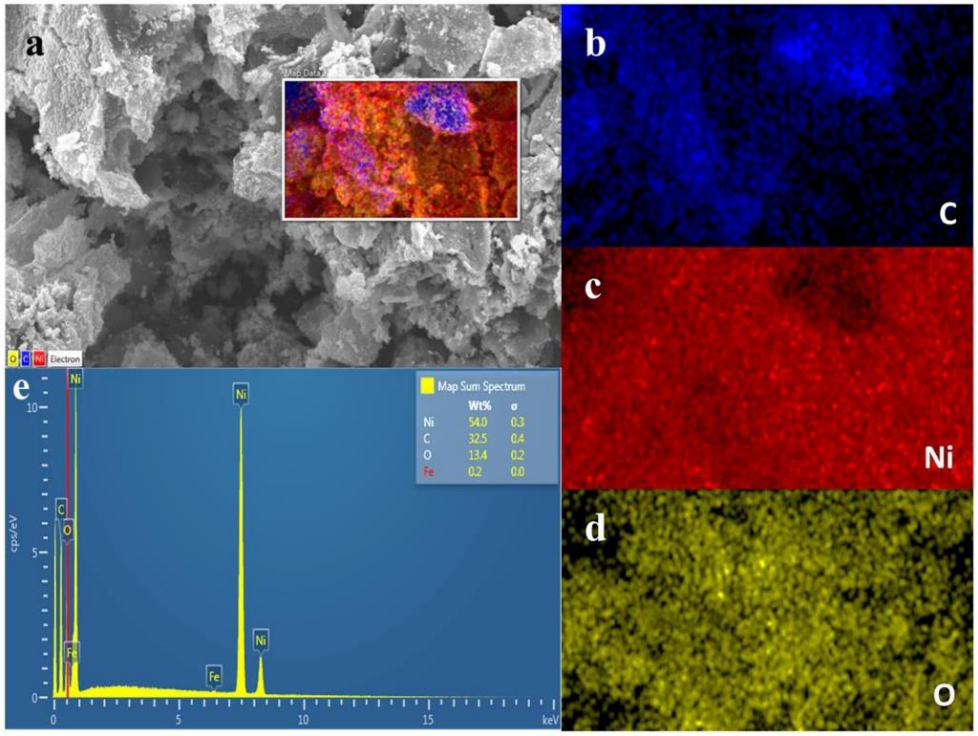

Figure 2.5 (a) SEM image of NiO_x@GR-C2 (inset: EDS composite elemental map); elemental mapping: (b) carbon (C), (c) nickel (Ni), (d) oxygen (O); (e) EDS spectrum

The specific surface areas and porosity distribution characteristics of these three samples were tested by nitrogen sorption isotherm technique. All samples exhibit IV type isotherms and H3 hysteresis loops, as shown in **Figure 2.6a.** The specific surface areas were 43.0 m^2/g, 30.0 m^2/g, and 57.3 m^2/g for NiO_x@GR-A2, NiO_x@GR-B2, and NiO_x@GR-C2, respectively. **Figure 2.6b** showed the pore distribution of NiO_x@GR-A2, NiO_x@GR-B2, and NiO_x@GR-C2. It can be seen that most pores are distributed in a narrow range from 4 to 7 nm, suggesting that all samples exhibited porous structures mainly composed of mesopores (according to IUPAC classification).

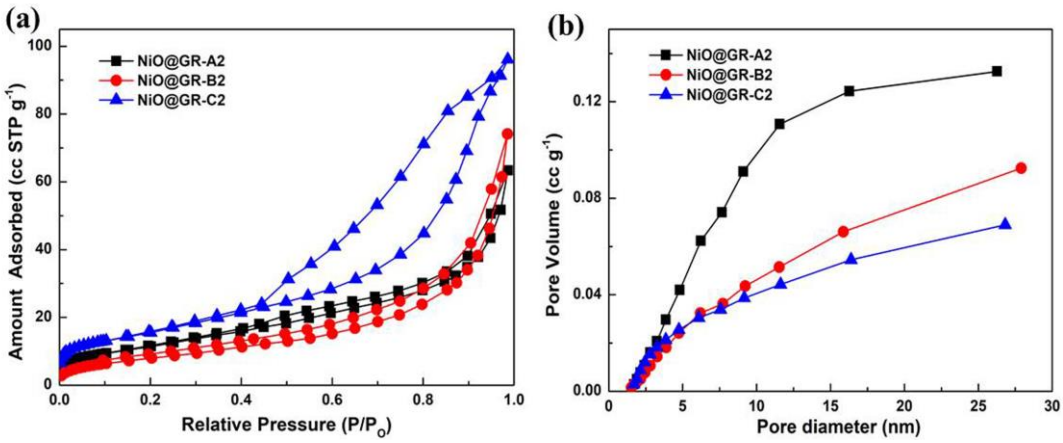

Figure 2.6 (a) N_2 adsorption-desorption isotherms and (b) the BJH pore size distribution plots of NiO_x@GR-A2, NiO_x@GR-B2, and NiO_x@GR-C2

By controlling the reaction conditions (the type of metal precursor and feeding ratio between the nickel precursor and graphene), we can better examine the trends of the electrochemical properties of the materials. The specific capacitance was calculated based on the GCD curves. **Figure 2.7** indicates the dependence of the specific capacitance of the NiO_x@graphene nanocomposites prepared using different metal precursors at different current densities. With the increase in the feeding ratio of the nickel precursor to graphene, the specific capacitance initially increased and then decreased. The reason for this result is probably the increased content of generated NiO_x after the decomposition of the nickel precursor. However, as the amount of added metal precursor increased, the energy required for the complete decomposition of the metal precursor also increased accordingly. Based on the graphene content supplied in this case (25 mg), the amount was not sufficient to produce enough energy to completely decompose all the metal precursors, and finally resulted in the decrease in the electrochemical properties.

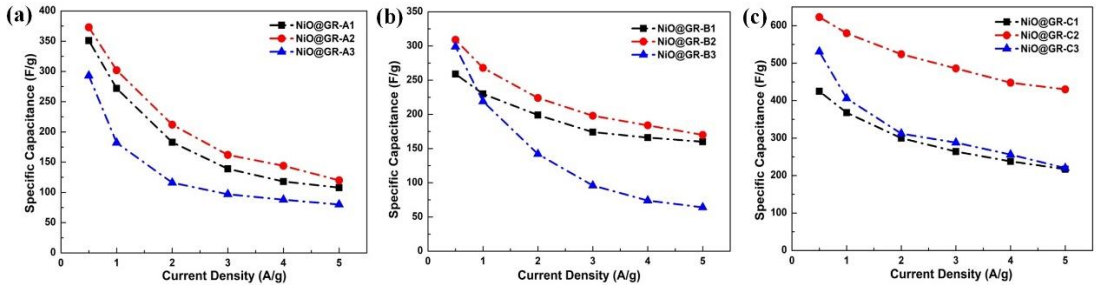

Figure 2.7 Specific capacitance of the NiO_x@GR nanocomposites at different current densities: (**a**) NiO_x@GR-A1, NiO_x@GR-A2, and NiO_x@GR-A3; (b) NiO_x@GR-B1, NiO_x@GR-B2, and NiO_x@GR-B3; and (**c**) NiO_x@GR-C1, NiO_x@GR-C2, and NiO_x@GR-C3

When comparing the electrochemical performance of the NiO_x@GR nanocomposites prepared using the different metal precursors under the optimal ratio (NiO_x@GR-A2, NiO_x@GR-B2, and NiO_x@GR-C2), NiO_x@GR-C2 exhibited the highest specific capacitance, corresponding to the largest integral area in the CV curves and the longest discharge time in the GCD curves at the same scan rate and current density (**Figure 2.8a-c**). This is most probably due to the highest specific surface area of NiO_x@GR-C2, which can boost the exposed active sites, facilitating contact with electrolytes, and the porous structure, which provides more pathways for ion transport, consequently promoting the faraday reaction. The effects of the metal precursors on the cyclic stability of the composite were also investigated at the current density of 1 A/g (**Figure 2.8d**). It can be seen that the capacitance retentions were 72.8%, 58.6%, and 62.2% for NiO_x@GR-A2, NiO_x@GR-B2, and NiO_x@GR-C2, respectively, after 4000 cycles in each case. The relatively high capacitance retention might be due to the synergistic effect between the graphene and the metal oxide,

which benefited from the buffering of the mechanical stress during the charge-discharge processes and increased the redox efficiency [146, 147]. Among the prepared composites, NiO_x@GR-A2 presented with the highest cycle stability, which may be attributed to the distribution of more large-sized pores in the NiOx@GR-A2 structure. Moreover, in **Table 2.4**, the electrochemical properties of NiO_x@GR prepared through microwave heating are compared with previously reported approaches. It is obvious that the microwave heating method shortens the reaction times from hours to minutes and exhibits a higher specific capacitance. The improved capacitance of NiO_x@GR may be attributed to the strong interaction between the NiO_x and the graphene sheets, resulting in an enhanced charge transport [148].

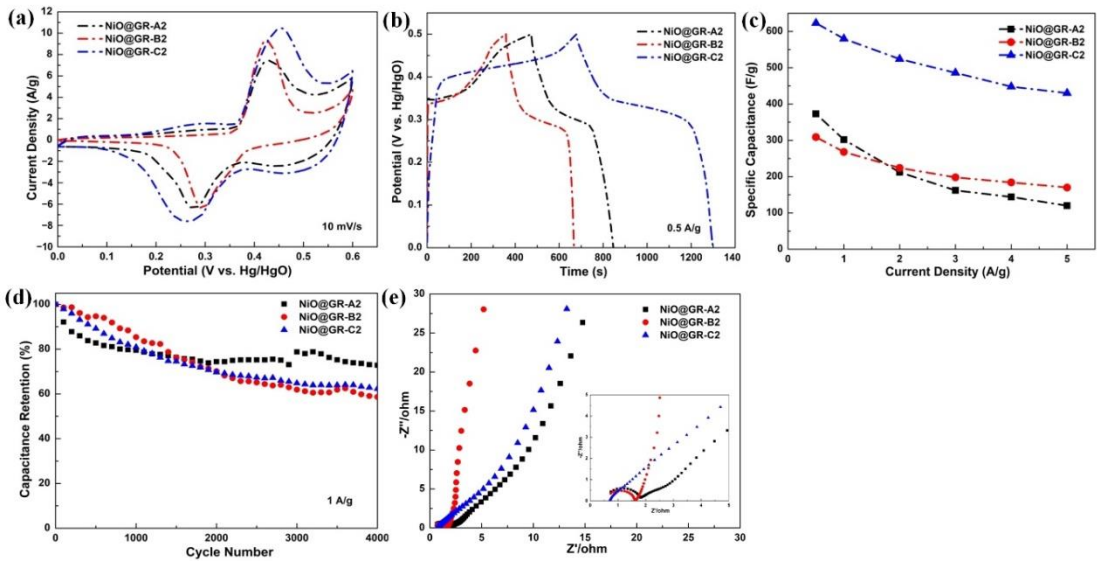

Figure 2.8 (a) CV curves, (b) GCD curves (c) specific capacitance, (d) Cyclic stability, and (e) Nyquist plots of the EIS (The inset shows the enlarged EIS of the electrodes) of NiO_x@GR-A2, NiO_x@GR-B2, and NiO_x@GR-C2

Table 2.4 Comparison of the electrochemical properties of NiO_x@GR prepared through microwave heating with previously reported approaches

Method	Specific Capacitance	Stability	Reaction Time	Ref
Thermal decomposition	417 F/g, 13A/g	85.5%, 3000 cycles	10 min	[149]
Hydrothermal and thermal decomposition	430 F/g, 0.2A/g	86.1%, 2000 cycles	4 h	[150]
Solvothermal	587 F/g, 1A/g	98%, 1000 cycles	12 h	[151]
Sol-gel	628 F/g, 1A/g	82.4%, 3000 cycles	24 h	[148]
Hydrothermal	500 F/g, 5 mV/s	84%, 3000 cycles	2 h	[152]
Microwave heating	623 F/g, 0.5A/g	62.2%, 4000 cycles	5 min	**Our work**

EIS analysis was conducted to investigate the electrochemical characteristics between the electrode and the electrolyte interface. The Nyquist plots consist of two parts: a small semicircle in the high-frequency region, and a straight line in the low-frequency region. In general, the semicircle is presented according to the charge transfer resistance of the electrode and the diameter of the semicircle is equal to the electrode resistance (R_{ct}). The vertical line corresponding to the Warburg impedance reflects the capacitive behavior of the electrode [28, 29, 153]. NiO_x@GR-C2 exhibited a smaller semicircle diameter

than NiO_x@GR-A2 and NiO_x@GR-B2 in the high-frequency region, which indicates that it had a lower charge transfer resistance. Furthermore, the NiO_x@GR-B2 electrode presented a nearly vertical linear shape in the low-frequency region, indicating that it had a better capacitive behavior than the other two electrodes due to the rapid ion diffusion (**Figure 2.8e**).

Figure 2.9 shows the CV curves of the NiO_x@GR-C2 electrode in the potential range of 0 to 0.6 V at various scan rates. A pair of oxidation/reduction peaks can be clearly observed, corresponding to the pseudocapacitance of the electrode. This was mainly due to the faradaic conversions between Ni (II) and Ni (III) in an alkaline medium, which can be elaborated by the following reaction:

$$NiO+OH^- \leftrightarrow 2NiOOH+e^- \quad (2.2)$$

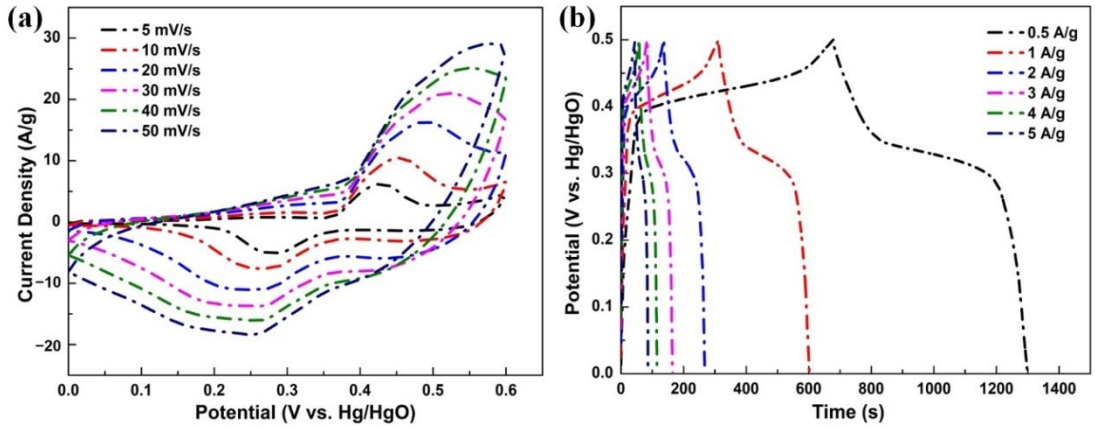

Figure 2.9 (a) CV curves of NiO_x@GR-C2 at varied scan rates. (b) GCD curves of NiO_x@GR-C2 at different current densities

As the scan rate increased, a slight shift in the peaks was observed, which may be ascribed to the polarization effect of the electrode [154]. In addition, the shape of the CV curves continued to indicate that the electrode had a good rate

capability (**Figure 2.9a**) [155]. The GCD curves presented with a similar plateau, matching the redox peaks of the CV curves **(Figure 2.9b).** As the current density decreased, the discharge time increased corresponding to the increase in the specific capacitance of the electrode. It can be concluded that, at a low current density, the charge had enough time to diffuse into the inner core of the electrode and access the active sites. Comparatively, at a higher current density, the current density increased rapidly, which caused a large number of ions to gather at the solid/liquid interface, increasing the internal diffusion resistance of the electrode [156, 157]. From 0.5 to 5 A/g, the specific capacitance of NiO_x@graphene shifted from 623 F/g (1.24 F/cm^2) to 430 F/g (0.86 F/cm^2). This value was higher than those previously reported for pure NiO [123, 125, 158].

When compared to previously reported NiO_x@graphene composites, our work still showed a higher value, as **Table 2.5.** The reason for the good rate capability and high capacitance of NiO_x@graphene might be the combination of the characteristics of metal oxide and graphene. The highly conductive graphene with a high area surface not only offered high electrical conductivity, but also provided more active sites and more interfacial contact for the redox reaction. The NiO_x with a highly porous structure offered more charge transfer channels. The increased contact area and evenly distributed porous structure can shorten the ion migration pathway and facilitate the transportation of electrons. Moreover, graphene, as a carrier, can give the metal oxides physical

support, increasing the stability of the nanocomposites during the charging and discharging processes [150, 159].

Table 2.5 Comparison of the electrochemical properties of NiO_x@GR with previously reported work

NiO Topography	Specific Capacitance	Stability	Ref
Aerogel	587.3 F/g, 1A/g	3000, 85.5%	[151]
Nanosheets	525 F/g, 0.2A/g	1000, 95.4%	[123]
Microsphere	555 F/g, 1A/g	20 000, 90.8%	[158]
Flowerlike	406 F/g, 5 A/g	5000, 65.4%	[160]
Nanowires	628 F/g, 1A/g	3000, 82.4%	[161]
Nanoflakes	240 F/g, 5A/g	1500, 100%	[162]
Nanoparticle	623 F/g, 0.5A/g	62.2%, 4000 cycles	**Our work**

To further gain insight into the reaction mechanisms, we can distinguish the effect of the capacitance on the electrode by kinetic analysis of the CV curves at various scan rates. The capacitive effect of the electrode can be described by plotting the relationship between the peak current and the sweep rate, with the following equation [95]:

$$i = av^b \tag{2.3}$$

where a and b are variable constants. By determining the value of b, we can determine the contribution of the diffusion control and capacitive effect to the total capacitance. When the b value is close to 0.5, the total capacitance is dominated by the diffusion-controlled faradaic process. When the b value is

close to 1, the charge storage process is controlled by the capacitive effect. As the value of b is between 0.5 and 1, this proves that the electrochemical process benefits from both the capacitive and diffusion-limited redox processes. The contributions of the capacitive effect and diffusion-controlled contribution to the total capacitance can be quantified using Dunn's method [18]:

$$i_{total} = k_c v + k_d v^{0.5} \quad (2.4)$$

Where $k_c v$ is the capacitive effect and $k_d v^{0.5}$ is the diffusion-controlled contribution. Then, transforming the equation into:

$$i_{total}/v^{0.5} = k_c v^{0.5} + k_d \quad (2.5)$$

through plotting $i_{total}/v^{0.5}$ versus $v^{0.5}$, the k_c and k_d can be determined. As shown in **Figure 2.10b**, the b values of the oxidation and reduction peaks were 0.6626 and 0.5544, respectively, suggesting that the charge storage of NiO_x@GR-C2 benefited from both the diffusion-controlled contribution and capacitive effect. The capacitive current separated from the total measured currents under the scan rate of 20 mV/s is displayed in **Figure 2.10a**. The details of the capacitive effect and diffusion-controlled contribution at different scan rates are shown in **Figure 2.10c**. At 5 mV/s, the percentage of the diffusive mechanism contribution was 93.4%. As the scan rate decreased, the capacitive contribution increased, while the diffusive contribution increasingly depressed. This was due to the fact that the ions did not have enough time to intercalate inside the material structures. However, in this system, the percentage of the pseudocapacitance contribution still remained at 90.2% at 50 mV/s; thus, the

pseudocapacitance contribution was believed to be dominative.

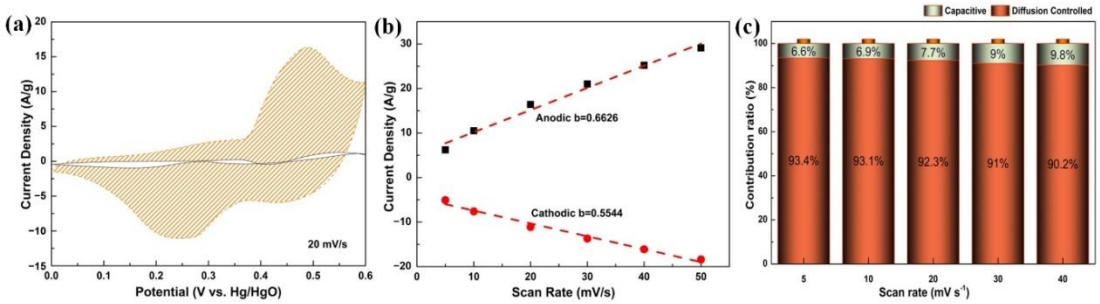

Figure 2.10 (a) CV graph indicating the capacitive contribution of NiO_x@GR-C2 at 20 mV/s. (b) The calculated b values at different scan rates. (c) A stacked bar graph showing the percentage of the total capacitance attributed to the diffusion-limited and capacitive contributions

2.5 Conclusions

In our work, we reported a simple, reproducible, low-cost, and fast approach to microwave synthesis for the preparation of hybrid electrode architectures. The synthesized nanocomposites were characterized using XRD, TEM, SEM, BET and EDS methods. The effect of the reaction conditions (the type of metal precursor and feeding ratio between the nickel precursor and graphene) on the formation mechanism of the electrode was demonstrated. The results proved that the microstructure and morphology of the electrode materials were metal precursor-dependent, which was related to the electrochemical performance of the electrodes. In addition, kinetic analysis was used to gain insight into the charge storage mechanisms at the interface between the electrode and the electrolyte during the energy storage process, which can give us a direction for advancing the performance of the devices. This work can serve

as a model for understanding the growth mechanisms and the synergistic effects of hybrid electrode materials consisting of carbon-based materials and metal oxides, and offers experimental support for the designing of hybrid electrode materials with an excellent electrochemical performance in the future.

Chapter 3: Fabrication of V_2O_5@PPy core-shell nanofiber electrode for supercapacitor

Abstract: To address the dissolution problem and further enhance the cycling stability and capacitive performance of V_2O_5, V_2O_5@PPy core-shell nanofiber was synthesized by combining a low-cost, easily processing, and eco-friendly sol-gel with *in situ* polymerization method in this work. V_2O_5@PPy showed a high specific capacitance of 307 F/g at 1 A/g and good cycling life (82 % capacity retention up to 1000 cycles). This benefited from the PPy coating layer with high conductivity facilitating charge transfer and protecting the dissolution of V_2O_5 in the aqueous solution. The synergistic effect between the V_2O_5 and PPy and the individual role of each component in the electrochemical process were studied to further explore the growth mechanism and provide the rational design electrode material fundamental in the future. Also, the two-electrode symmetric V_2O_5/PPy device exhibited a maximum energy density of 37 Wh/Kg when the power density was 161 W/kg.

3.1 Introduction

To address key issues such as energy crisis and environmental pollution, renewable, sustainable, and environmentally friendly energy storage devices including rechargeable batteries [153, 163-165] and supercapacitors, [166-168] have been intensively studied due to their superior power density, long cycle life, and high reversibility. [169, 170] However, compared to batteries and fuel cells, supercapacitors typically deliver an unsatisfactory energy density (<10 W h/kg),

which is considered as the greatest obstacle to supercapacitors for practical applications. Currently, the development of supercapacitors with high energy density to meet the increasing demand for energy storage is critically needed.

The key component of supercapacitors is the electrode. Vanadium pentoxide (V_2O_5) possesses a layered structure, high theoretical specific capacity (2120 F/g), and multiple oxidation states of vanadium (V^{2+}, V^{3+}, V^{4+}, and V^{5+}) corresponding to a wide working window (up to 1.2 V in H_2O). [106, 171] In addition to all the above-mentioned great features as an electrode candidate material, the large interlayer spacing of V_2O_5 allows easy insertion/extraction of cations with larger ionic radii (Na^+ and K^+). [172, 173] V_2O_5 is believed to be one of the most promising electrode materials for the preparation of supercapacitors. Therefore, diverse morphologies of V_2O_5 nanomaterials (such as nanowire, nanotube, nanofiber, nanowire, and nanorod) have been reported. [79] For example, a simple hydrothermal method was used for the preparation of V_2O_5 nanorods by Balamuralitharan et al. The electrode showed a high specific capacitance (417.3 mF/cm^2) and good cycling stability (80% capacitance retention after 3000 cycles).[174] Ahirrao and co-workers have synthesized V_2O_5 nanowires and the composite of V_2O_5 nanowires with highly conductive graphene sheets (V_2O_5-NW-G) by facile hydrothermal method. V_2O_5-NW-G revealed a high gravimetric capacitance of 1002 F/g and an excellent energy density of 116 Wh/kg.[173] However, the high dissolution in the liquid electrolyte and the exchange of valence during the charge and discharge process resulting structural instability, greatly hindered long-term cycling performance and capacitive performance. To

mitigate these limitations, V_2O_5 hybrid nanomaterials have been considered recently. Generally, due to low cost, abundant raw materials, and chemical and mechanical stability, carbonaceous materials are regarded as good candidates for combining with V_2O_5. For example, V_2O_5/reduced graphene oxide composites were synthesized by a coprecipitation method leading to a high specific capacitance (484 F/g at 0.5 A/g), and 52 % capacitance retention from 0.5 A/g to 10 A/g. After 1000 cycles, 83 % initial capacitance was retained. [175] Three-dimensional (3D) V_2O_5/multiwalled carbon nanotubes (MWCNTs) core/shell structure with hierarchical porous structure, and high specific surface area was developed through a one-pot sol-gel process. [176] The hybrid nanocomposites exhibited enhanced specific capacitance (625 F/g) and outstanding cycle performance (> 20000 cycles). However, this kind of composites still cannot solve the dissolution and cyclic stability problem of V_2O_5.

Recently, the combination of conducting polymer with active materials to form “core-shell” structures is proven a good strategy to enhance the stability of electrodes. First, the core-shell structure can merge the functionalities from the intrinsic properties of each component, which benefits higher electrical conductivity, shorter ionic transport, and better cycling stability of the electrode. Second, the aggregation and side reactions of active materials can be restrained by the coating layer through lower the surface energy.[177, 178] For example, Jabeen et al. reported core-shell $NiCo_2O_4$@polyaniline ($NiCo_2O_4$@PANI) nanorod arrays with a high specific capacitance of 901 F/g and outstanding capacitance retention of ~91% after 3000 cycles.[179] $NiCo_2O_4$ with highly porous and highly conductive as the

conductive core provided fast electron transport. PANI layer as a protective shell effectively shielded the dissolution and collapse of $NiCo_2O_4$ structure in acidic electrolyte. Ti-doped Fe_2O_3@poly(3,4-ethylenedioxythiophene) (Ti-Fe_2O_3@PEDOT) core-shell has been developed and yielded a remarkable large areal capacitance of 1.15 F/cm with outstanding rate capability and ultrahigh cycling durability (96% of its initial capacitance was retained after 30000 cycles).[180] The excellent cycling performance of Ti-Fe_2O_3@PEDOT could attribute to the PEDOT that not only provided high conductivity to the material but also acted as a protective layer offering additional protection to prevent the architecture from being destroyed.

In this work, we introduce conducting polymer, polypyrrole (PPy), to decorate V_2O_5 forming V_2O_5/PPy core-shell nanofibers. The hydrophobic PPy forms a shield layer effectively preventing the dissolution of V_2O_5 in the water. In addition, the high conductivity of PPy is also beneficial to the energy storage and ion/electron transport. In order to allow the PPy uniformly coated on V_2O_5, the V_2O_5 nanofibers are developed through an easy processing, low cost, and ecofriendly sol-gel method, firstly. The prepared V_2O_5 nanofibers are then used as a reactive template for the uniform coating of the PPy on the out layer of V_2O_5 by *in situ* polymerization process. The ratio of PPy to V_2O_5 is optimized to make the electrochemical properties of the material reach the maximum value. And also, the impact of PPy thickness on the overall performance of the electrode is analyzed. To further explore the growth mechanism and provide the rational design electrode material fundamental in the future, the synergistic effect between the V_2O_5 and PPy and the individual role of each

component in the electrochemical process is studied.

3.2 Experimental

3.2.1 Materials Characterization

The morphologies of the samples were confirmed by Scanning Electron Microscopy (SEM; Apreo FE). Energy dispersive X-ray spectroscopy (EDS; EDAX Instruments) was used to investigate the chemical composition of the samples. Fourier transform infrared (FTIR) spectra were measured on a Nicolet 6700 using KBr disk in the region of 400-4000 cm^{-1}. Thermogravimetric analysis (TGA) was performed on TA Instruments TGAQ500 with a ramp rate of 40 ℃/min from 20 ℃ to 800 ℃ under a nitrogen atmosphere.

3.2.2 Materials

Ammonium metavanadate was obtained from J.T. Baker. Dowex Marathon C (Hydrogen, H^+ Form), ammonium peroxydisulfate (APS), poly(vinylidene fluoride), and carbon black were purchased from Alfa Aesar. Pyrrole monomer was offered by Tokyo Chemical Industry. Hydrochloric acid came from VWR, USA. Sodium dodecylbenzene sulfonate (SDBS) was from TCI America.

3.2.3 Preparation of V_2O_5 nanofiber

The V_2O_5 nanofibers were synthesized by a simple sol-gel method. In a typical process, ammonium metavanadate (0.8 g) and Dowex (8 g) were dissolved into 140

ml distilled water under constant magnetic stirring for 10 min and continued to react for another two weeks at room temperature. Then, the yellow gel solution was obtained, which indicates the successful fabrication of V_2O_5 nanofiber.

3.2.4 Preparation of V_2O_5@PPy nanofibers

For the synthesis of V_2O_5@PPy nanofiber, varied volume (40, 20, and 10 ml) of V_2O_5 nanofiber suspension solution and 20 mg of SDBS were dispersed into 30 ml of deionized water under stirring for 10 min, respectively. Then, 0.1 ml of pyrrole monomers and 115 mg of APS were added into the above mixture at room temperature. After 3-4 hours, the polymerization reaction was completed. The solution color turned from orange to black, and the black products were collected by filtrating and washed with deionized water, ethanol, and acetone three times, respectively. The SDBS on the one hand acted as a surfactant that enhanced the dispersing of the V_2O_5 in the water, on the other hand, served as a dopant to connect the V_2O_5 and protonated pyrrole via electrostatic interaction. The detailed preparation was given in **Table 3.1**.

Table 3.1 Operation conditions for synthesizing V_2O_5@PPy-n composites

Sample	V_2O_5 Sol	Pyrrole	SDBS
V_2O_5@PPy-0	0 ml	0.1 ml	0 mg
V_2O_5@PPy-1	10 ml	0.1 ml	20 mg
V_2O_5@PPy-2	20 ml	0.1 ml	20 mg
V_2O_5@PPy-3	40 ml	0.1 ml	20 mg

3.2.5 Electrochemical measurements

The electrochemical performance was investigated by galvanostatic charge-discharge (GCD), cyclic voltammetry (CV), and the electrochemical impedance spectroscopy (EIS) test. The working electrode is fabricated by mixing the active material, carbon black, and poly(vinylidene fluoride) in an 80:10:10 weight ratio together. Then N,N-dimethylformamide as a solvent is added to the mixture to form the homogeneous slurry which is coated onto the pretreated nickel foam (1.0 cm × 1.0 cm). The electrode is dried at 60 ℃ for 24 h under a pressure of 20 M Pa and the mass loading of active material is about 1 mg/cm^2. The Ag/AgCl electrode and platinum sheet (1 × 1 cm^2) are used as the reference electrode and counter electrode, respectively. The electrolyte is 1 M Na_2SO_4 aqueous solution. The symmetric cell is assembled by two identical electrodes used in a three-electrode system. The specific capacitance (C_s, F/g) of electrode is calculated according to galvanostatic discharge curves as: [181]

$$C_s = I \times \Delta t / \Delta V \times m \tag{3.1}$$

Where I is the discharging current (A), Δt is discharge time (s), ΔV is the potential window (V), and m is the mass of active material (g).

The energy density (E, Wh/kg) and power density (P, W/kg) are obtained by

$$\mathrm{E} = C_s V^2 / 2 \tag{3.2}$$

$$\mathrm{P} = E \times 3600 / \Delta t \tag{3.3}$$

3.3 Results and discussions

Thermogravimetry analyses (TGA) were carried out to determine the mass content of V_2O_5. As the amount of V_2O_5 solution added increases, the content of V_2O_5 in V_2O_5@PPy nanocomposites also increased. According to the TGA curves of V_2O_5@PPy-n (**Figure 3.1**), the mass content of V_2O_5 is 36 %, 26 %, 8.4 %, and 1.9 % for V_2O_5@PPy-3, V_2O_5@PPy-2, V_2O_5@PPy-1, and V_2O_5@PPy-0, respectively. Obviously, the addition of surfactant can promote the contact of V_2O_5 and PPy, showing a higher percentage of V_2O_5 compared to surfactant-free.

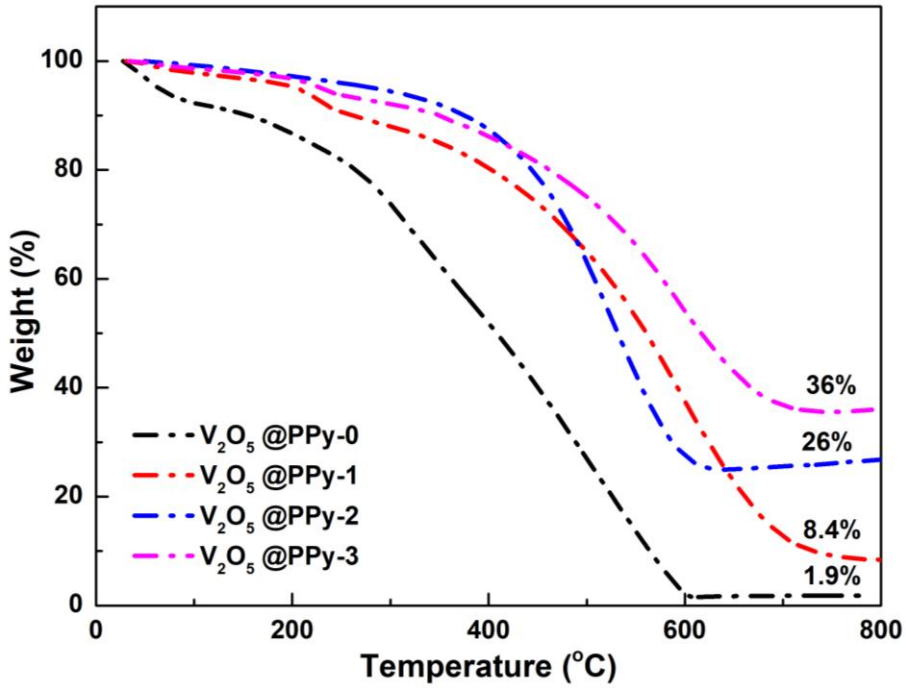

Figure 3.1 The TGA curves of the V_2O_5@PPy-n (n = 0, 1, 2, 3)

Figure 3.2 shows the FTIR spectrum of V_2O_5@PPy. The characteristic peak at 1033 cm^{-1} can attribute to the V=O stretching vibration. The peak located at 877 cm^{-1} is related to the stretching vibration of doubly coordinated oxygen (bridge oxygen) bonds. The symmetric and asymmetric vibrational modes of O-V-O are presented at

782 cm^{-1} and 671 cm^{-1}, respectively. The C=C/C-C stretching vibrations mode of PPy appears at 1544 cm^{-1} and 1448 cm^{-1}. The peaks at 1294 cm^{-1} and 1166 cm^{-1} are assigned to the C-N stretching vibrations and in-plane deformations of C-H. [182, 183]

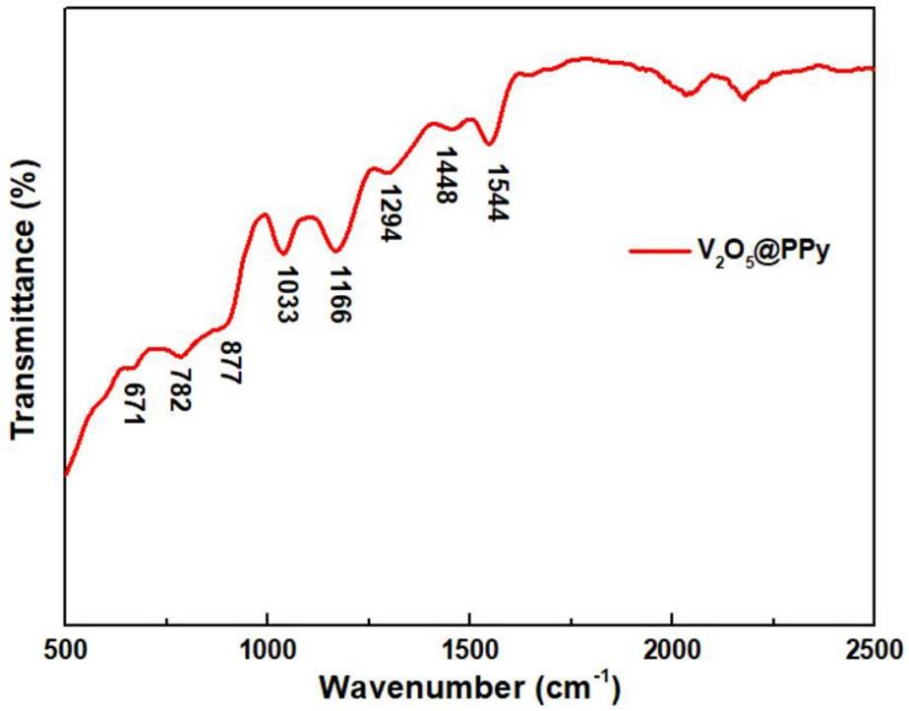

Figure 3.2 FTIR spectra of V_2O_5@PPy

The morphology of V_2O_5@PPy composites was confirmed using SEM. As seen in **Figure 3.3a**, V_2O_5@PPy presents nanofiber morphology. The TEM image proves that the PPy nanofibers are homogenously sheathed onto the surface of the V_2O_5 forming a core-shell structure (**Figure 3.3b**). The highly conductive shell of PPy can effectively avoid the dissolution of V_2O_5 increasing the cycling stability of the electrode. In addition, we could clearly observe the 3D-interconnected and interpenetrating structure of the V_2O_5@PPy, which benefits the charge transfer. **Fig. 3c** shows the elemental maps of V_2O_5@PPy composites, where carbon (C) and

nitrogen (N) present a uniform dispersion throughout V_2O_5, which agrees well with the TEM result.

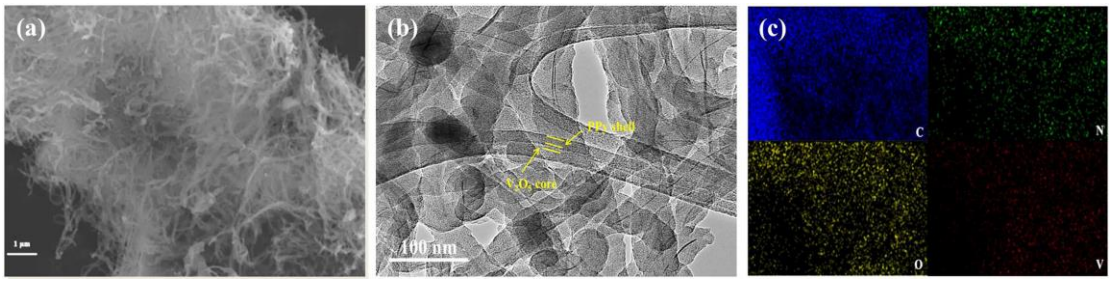

Figure 3.3 (a) SEM and (b) TEM image of V_2O_5@PPy; (c) Elemental mapping images of vanadium (V), carbon (C), nitrogen (N) and oxygen (O)

3.4 Electrochemical characterization

The three-electrode system was used to investigate the electrochemical performance of the as-prepared V_2O_5@PPy electrodes. **Figure 3.4** shows the CV curves of V_2O_5@PPy-n composites at different scan rates from 10-50 mV/s in a potential range of -0.2 to 0.7 V. All curves present a good symmetrical shape implying superior reversible redox capabilities (**Figure 3.4a-c**). [184] There were no distinctly redox peaks observed, which suggested that the fast electron and ion transferred throughout the electrodes. The electrochemical charge-storage mechanism occurring at V_2O_5 electrodes could be expressed as follows:[183]

$$V_2O_5 + xNa^+ + xe^- \rightarrow Na_xV_2O_5$$

With the increase of the scan rates, the shape of the CV curves only has a small distortion, which proves that the V_2O_5@PPy composites have good rate capability. Additionally, the specific capacitance was inversely proportional to the increment of the scan rate. At a low scan rate, the ions have enough time to diffuse into the internal

channel of the electrode and access the active site to complete the redox reaction, thereby generating a good specific capacitance. At high scan rates, the current density increases rapidly thus there is less time for ion diffusion, which decreases the degree of the accessibility of ions and active sites. [190] On the other hand, a large number of ions are concentrated at the solid/liquid interface, leading to the polarization performance of the electrode, which presents a decrease in electrode capacitance value and an increase in the internal resistance of the electrode. The same results can be observed in the GCD curves (**Figure 3.4d-f**). As the current density decreases, the corresponding discharge time increases indicating the ions transfer between the electrolyte and the surface of the electrode required sufficient time to complete. All curves show an ideal linear shape with a small resistance drop, again demonstrating that the electrode possesses superior pseudocapacitive behavior. Moreover, the approaching symmetrical charging and discharging time corresponds to the good reversibility of electrodes during the cycling process.

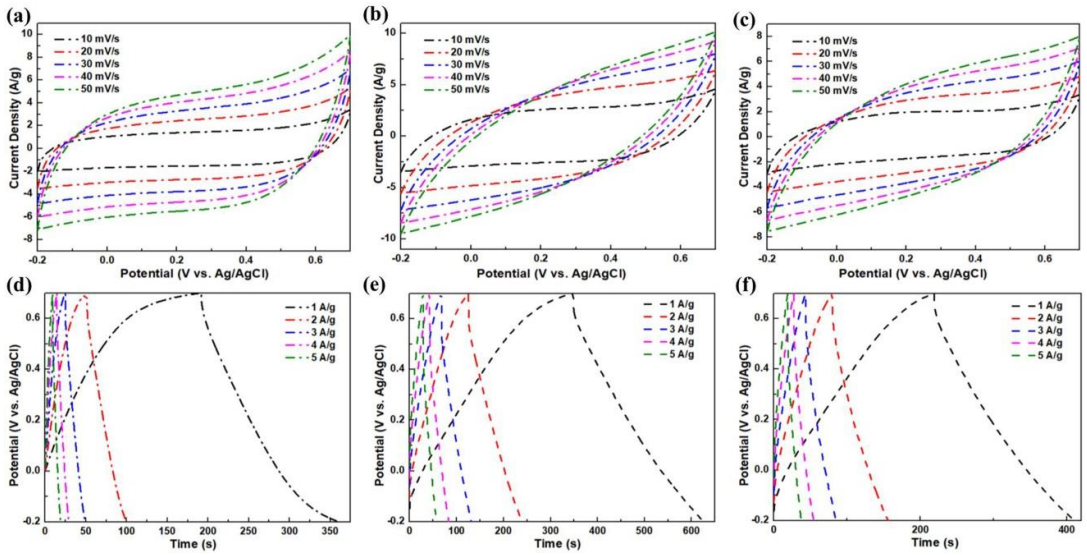

Figure 3.4 CV curves of (a) V_2O_5@PPy-1; (b) V_2O_5@PPy-2; (c) V_2O_5@PPy-3 at different scan rates; Charge-discharge curves of (d) V_2O_5@PPy-1; (e) V_2O_5@PPy-2; (f) V_2O_5@PPy-3 at different current density

Figure 3.5a displays the CV curves of V_2O_5@PPy electrodes with different V_2O_5-to-PPy mass ratios at 20 mV/s. As the thickness of PPy increases, the integrated area of CV curves first increases and then decreases. This result is probably due to the excessively thick overcoat PPy layer which might diminish the effective contact area between electrolytes and metal oxides and limit the transport of ions. [191] The specific capacitance values of electrodes are estimated from the GCD curves. V_2O_5@PPy-2 shows the highest specific capacitance of 307 F/g at 1 A/g than those of V_2O_5@PPy-1 (186 F/g) and V_2O_5@PPy-3 (212 F/g) (**Figure 3.5b)**. This capacitance value (307 F/g) is higher than those of pure PPy (100 F/g) and stacked V_2O_5 (143 F/g). [30, 192, 193] The improved electrochemical properties can be attributed to the PPy decoration which not only provides high conductivity that enhances electron

migration but also makes pseudocapacitance contribution to the overall capacitance. [191, 194]

Further, the cycling stability is an important criterion for the practical application of supercapacitor. The specific capacitance retention of electrode materials are investigated at a current density of 3 A/g and shown in **Figure 3.5c**. It is found that V_2O_5@PPy-3 shows a higher stability than V_2O_5@PPy-1 and V_2O_5@PPy-2. After 1000 cycles, 82 % of its initial capacitance is maintained. A possible reason behind relatively high capacitance retention may be due to the strong synergistic effect between V_2O_5 and PPy. On the one hand, the PPy sheath layer can suppress the dissolution of V_2O_5 in the aqueous electrolyte. On the other hand, the interpenetrating structure of PPy@V_2O_5 can reduce the agglomeration of the individual components of the composites, and resist the volume change of the electrode material during the charging and discharging process. [191] V_2O_5@PPy-1 has the worst stability among the three, with only 64 % of initial capacitance value retention after 1000 cycles. This can be attributed to the thick PPy coating that is more likely to form shear cracks on the surface reducing the stability of V_2O_5@PPy. [191]

To understand the electrochemical activities between the electrode and electrolyte interface, the electrochemical impedance spectroscopy (EIS) analysis was conducted at open-circuit voltage using AC amplitude of 0.005 V in the frequency range of 10^{-1} to 10^5 Hz. The Nyquist plots is presented in **Figure 3.5d** and fitted based on the equivalent circuits. In the medium-high frequency region, the semicircle is presented, corresponding to the charge-transfer resistance (R_{ct}) of the electrode, which

is caused by the discontinuity of electronic and ionic conductivity during the charge transfer process. [195] The semicircle diameter of V_2O_5@PPy-2 is smaller than those of V_2O_5@PPy-1 and V_2O_5@PPy-3 indicating a lower charge-transfer resistance. [196] The decrease in electrode resistance of V_2O_5@PPy-2 may be affected by the thickness of the PPy coating. A slope considered as the transition between the medium-high frequency region and the low-frequency region can be attributed to the Warburg impedance that arises from the diffusion of ions into active materials. [197] At the low-frequency region, when the phase angle equal to 90 ° presenting the ideal of electrochemical double-layer capacitors. All the curves yielded a 45 ° slope indicates the electrode materials have a pseudocapacitive behavior [28]. V_2O_5@PPy-2 shows a steeper straight line indicating a smaller ionic diffusion resistance than other samples. [29]

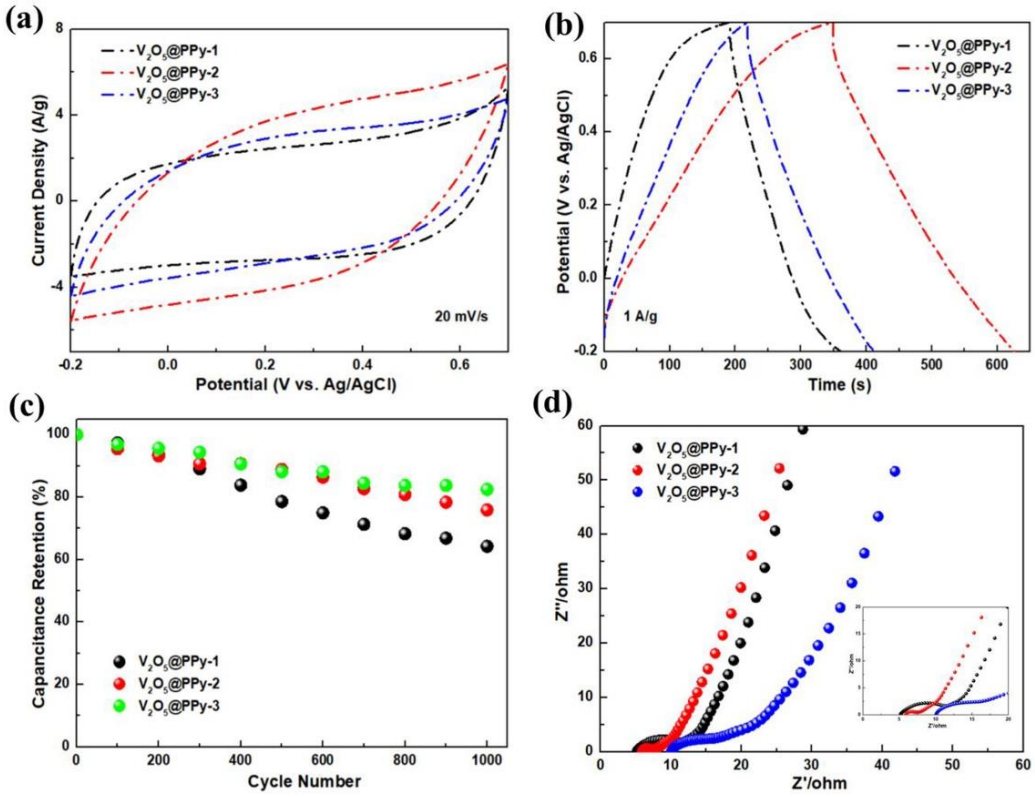

Figure 3.5 (a) CV and (b) GCD curves for V_2O_5@PPy-n; (c) The cycling stability of V_2O_5@PPy-n at 3 A/g; (d) Nyquist plots for V_2O_5@PPy-n. The inset shows the enlarged view of the intercepts of the corresponding EIS curves at the real axis at the medium-high frequency region

The charge storage mechanisms were further studied by the kinetic analysis based on the CV curves in the three-electrode system. The b-values of oxidation and reduction peaks are calculated according to: [16, 198]

$$i = av^b \tag{3.4}$$

Where a and b are constants, and v is scan rate. Typically, the value of b is equal to 0.5 standing for that the current is controlled by a diffusion process. The b value is 1, indicating that the current is controlled by the surface-controlled. As shown in **Figure 3.6a**, the b values of V_2O_5@PPy-1 are 0.767 and 0.139, respectively,

suggesting that charge storage benefits from both the diffusion-controlled and capacitive. In case of V_2O_5@PPy-2 and V_2O_5@PPy-3, the capacitive process contributes to the charge storage since the obtained b values are very close to 0.5 (**Figure 3.6b and 3.6c)**. The contribution detail of capacitive and diffusion-controlled contribution at different scan rate can be distinguished according to Dunn's method. [18, 199]

$$i = k_1 v + k_2 v^{1/2} \tag{3.5}$$

In all types of samples, with the increase of the scan rates, the capacitive contribution increases, while the diffusive contribution is depressed (**Figure 3.6d-f)**. This is due to the fact that ions cannot get enough time to intercalate inside the material structures. With the increase of V_2O_5-to-PPy, the diffusion-controlled contribution increases and the surface capacitive contribution decreases. The decrease of the diffusion-controlled contribution can be attributed to the over-thick PPy coating layer resulting in the surface area decreasing and restricting the contact between the electrolyte and electro-active sites.

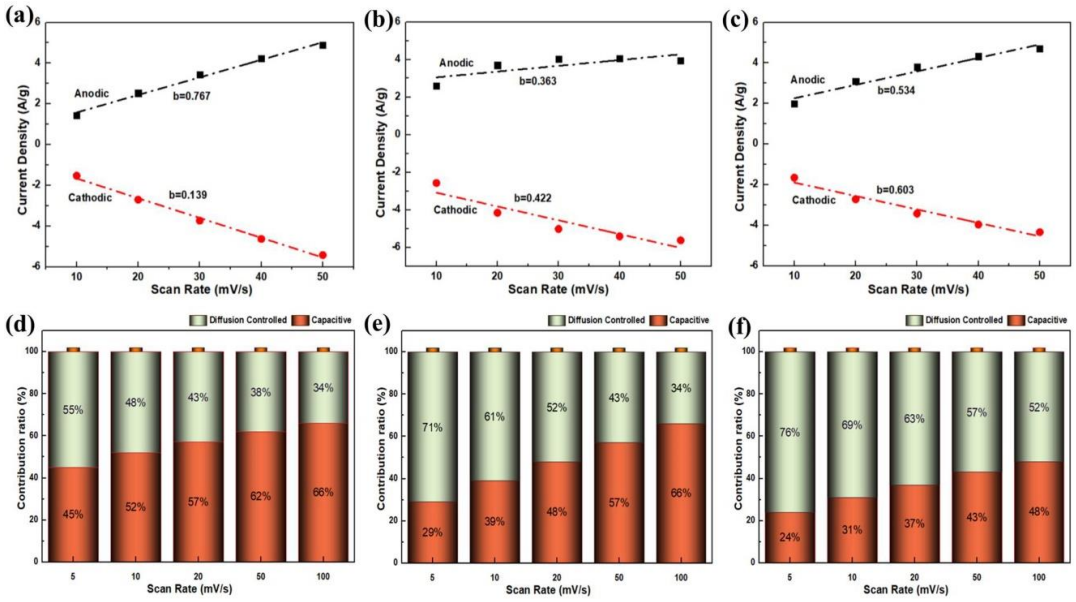

Figure 3.6 The calculated b values during the anodic and cathodic scans for (a) V_2O_5@PPy-1; (b) V_2O_5@PPy-2; (c) V_2O_5@PPy-3; and the contribution detail of surface capacitive and diffusion limited for (d) V_2O_5@PPy-1; (e) V_2O_5@PPy-2; (f) V_2O_5@PPy-3

To explore the practical application of V_2O_5@PPy, an aqueous symmetric supercapacitor was assembled using two pieces of V_2O_5@PPy-2 electrode (the mass loading of each piece is 1 mg). **Figure 3.7** illustrates the schematic structure of the symmetric supercapacitor. **Figure 3.7a and 3.7b** displays the CV and GCD curves of V_2O_5@PPy//V_2O_5@PPy. All CV curves are highly symmetrical at different scan rates corresponding to the excellent reversibility of the electrode. The specific capacitance is calculated according to the GCD curves by considering the total active mass of the device. The highest specific capacitance of 91 F/g is delivered by V_2O_5@PPy//V_2O_5@PPy device, demonstrating a good electrochemical property. The cycling performance is exhibited in the **Figure 3.7c**. With 64% of the initial specific capacitance is retained after 1000 cycles at 0.5A/g (**Figure 3.7d**). The overall

performance of a symmetric supercapacitor device is evaluated by the ragone plot (energy density vs. power density). As shown in **Figure 3.7e**, the energy density of device achieves 37 Wh/Kg when the power density is 161 W/kg. When compared with other V_2O_5 hybrid materials, our device shows a better performance than most of the previous V_2O_5 composites electrodes reported. [193, 200-205] The above results indicate the PPy coated V_2O_5 could be a great potential electrode material candidate for a variety of energy storage applications.

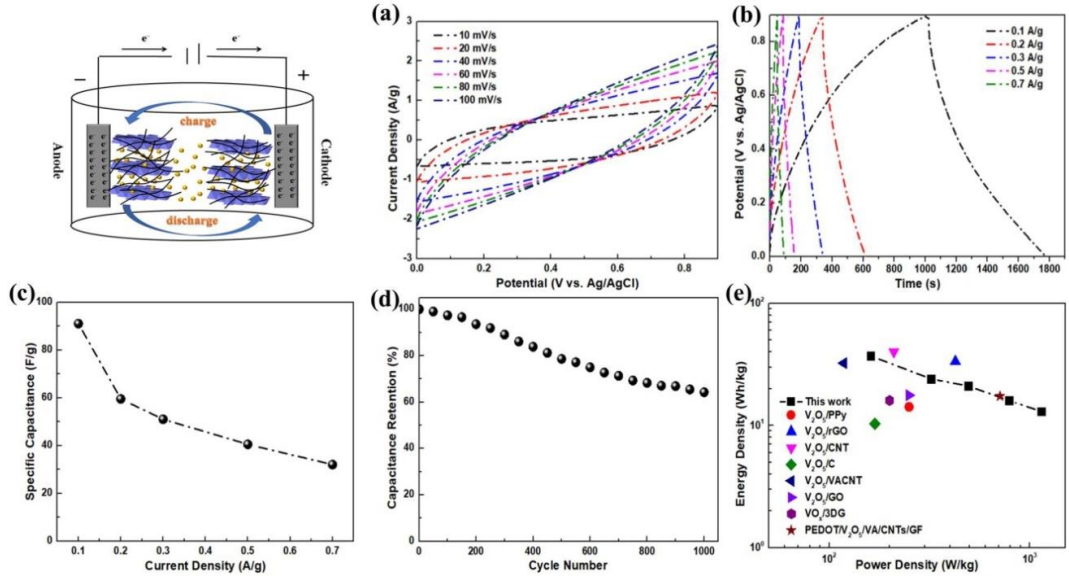

Figure 3.7. (a) CV and (b) GCD curves of V_2O_5@PPy//V_2O_5@PPy; (c) The cycling stability and (d) specific capacitance of V_2O_5@PPy//V_2O_5@PPy; (e) The Ragone plot

3.5 Conclusion

In summary, a low-cost, easy processing, and eco-friendly sol-gel method is used to synthesize the PPy-coated V_2O_5 nanocomposites. The PPy coating layer can not only offer a high conductivity to facilitate charge transfer but also protect the dissolution of V_2O_5 in the aqueous solution. A high specific capacitance, good cycling

stability performance, and excellent energy density are presented for the V_2O_5@PPy benefiting from the enhanced conductivity, the synergistic between V_2O_5 and PPy, and the more stable form of composites. Besides, the influence of the PPy coating layer on the electrochemical properties of the hybrid electrodes is systematically studied by the electrochemical method (CV, GCD, and EIS), and the role effect of the electrode in each part is analyzed in the electrochemical process.

Chapter 4: High performance flexible freestanding conductive nanopaper based on PPy:PSS nanocellulose composite for supercapacitors

Abstract A freestanding, binder-free flexible PPy:PSS/cellulose nanopaper (PPy:PSS/CNP) electrode is successfully fabricated by a low-cost, simple, and fast vacuum filtration method for the first time. The hierarchical structure of cellulose (CNF) with high surface area and good mechanical strength not only provides a high electroactive region and shortens the diffusion distance of electrolyte ions, but also prevents the volumetric expansion/shrinkage of the polypyrrole (PPy) during the charging/discharging process. The optimized PPy:PSS/CNP exhibits a high areal specific capacitance of 3.8 F/cm^2 (corresponding to 475 F/cm^3 and 240 F/g) at 10 mV/s and good cycling stability (80.9% capacitance retention rate, 5,000 cycles). The cyclic voltammetry curves of PPy:PSS/CNP at different bending angles indicate prominent flexibility and electrochemical stability of the electrode. Moreover, a symmetric supercapacitor device is assembled and delivers a high areal energy density of 122 μWh/cm^2 (15 Wh/cm^3) at a power density of 4.4 mW/cm^2 (550 mW/cm^3), which is superior to other cellulose-based materials. The combination of high supercapacitive performance, flexibility, easy fabrication, and cheap advantages of the PPy:PSS/CNP electrodes offers great potential for developing the next generation of green and economical portable and wearable consumer electronics.

4.1 Introduction

Supercapacitors, a type of energy storage systems, have attracted enormous attention from the academic and industry communities due to the fast charge-discharge rate, long cycling life, good operational safety, and high power density [206, 207]. With the boosted development of rechargeable consumer electronics, portable and wearable electronic devices are rapidly appearing in our life such as roll-up displays, smart textiles, etc., and the flexible supercapacitor market has become an emerging field. In general, flexible supercapacitors not only need to meet the fundamental standard of the conventional capacitors but also possess promising properties including lightweight and extra mechanical flexibility [208, 209]. In the past a few years, many researches have focused on fabricating the flexible supercapacitors with high electrochemical performance. Nevertheless, the challenges originating from the intended end-use are faced such as the high cost of raw materials, flexibility, complicated fabrication procedures, toxicity, and the screening of the substrate with high conductivity still need to be overcome [210]. Therefore, the development of flexible supercapacitors with low-cost, lightweight, good mechanical properties, environmental beingness, and outstanding electrochemical properties is urgently necessitating.

As the central component of a flexible supercapacitor, flexible electrodes are considered to have a key impact on the performance of the flexible supercapacitors. Polypyrrole (PPy) as a kind of conductive polymer has been extensively studied as a promising component of electrode materials due to its low-cost, environment-

friendliness, facile and simplistic preparation, good redox property, and high theoretical specific capacitance [211, 212]. Nevertheless, the poor conductivity, weak solubility in common solvents and the instable structure of PPy have limited its practical application. To address these issues, numerous strategies have been applied to modify the interconnected microstructure and improve the performance of PPy. One typical strategy is to blend or composite PPy with highly conductive carbon-based materials (i.e., active carbon, carbon nanotube (CNT), and graphene) to cushion the molecular chain damage of PPy during the repeated adsorption/desorption of electrolyte ions [213, 214]. In addition, polymeric surfactants with different sulfonating groups have been used as additives to improve thermal and mechanical stabilities, solubility and dispersity, and electric conductivity of PPy during the polymerization process [215, 216]. Especially, the water soluble sulfonated polymeric surfactant (polystyrene sulfonate (PSS)) with excellent mechanical flexibility and tunable electrical conductivity has attracted intense attention among various surfactants [217-219]. For instance, Nanocolloidal polypyrrole/poly(styrene sulfonate) (PPy:PSS) composites were prepared through a dispersion polymerization technique by Maruthamuthu, S et al [220]. The conductivity and solubility of PPy were easily controlled by the concentrations of PSS. When the weight ratio of PSS was 15% with pyrrole, the product exhibited improved dispersion, a higher dielectric constant, and relatively low dielectric loss. Although the water-dispersible and conductivity properties of PPy have been effectively improved, the lack of the ability to form stable chemical bonds and entangled networks made them easily broken and difficult

to form films. Moreover, the fabrication of flexible supercapacitor electrodes usually needs binder, conductive additive, and current collector. However, these constituents would increase the weight and resistance of the electrode, and reduce the accessible surface of the electrode. Therefore, many efforts should be focused on developing freestanding, binder-free flexible thin film electrodes which can also function as current collectors themselves displaying high electrochemical performance, and good mechanical properties.

Cellulose nanofibers (CNFs) existing in cell walls of plants are the most abundant natural polymer on earth and are considered as a promising alternative advanced material for the next generation petroleum-based materials in the context of increasing consumption of non-renewable resource petroleum with outstanding properties including abundant raw material, low-cost production, high specific surface area, great biocompatibility and biodegradability, etc [221, 222]. Recently, CNFs are considered promising supporting substrates for energy storage devices. The flexible conducting film electrode of multiwalled carbon nanotube/poly(3,4-ethylenedioxythiophene):PSS/cellulose was prepared by supramolecular assembly showing a high specific capacitance (485 F/g, at 1 A/g) and good cycling stability (95% initial capacitance remained after 2000 cycles) [223]. The freestanding electrode PPy/functionalized carbon nanotubes/cellulose composite films were prepared through a facile and green freeze and thaw process, where CNF and functionalized carbon nanotubes as matrices not only provided a large interfacial area for the storage/release of charge carriers but also formed a porous structure through

interfacial hydrogen bonding between the functionalized carbon nanotubes and CNF to provide charge transfer channels. The as prepared composites exhibited high areal capacitance (2147 mF/cm^2 at 1 mA/cm^2), and outstanding cycling stability [224].

In this work, a low-cost and environmentally-friendly nanocellulose was chosen as the support substrate to synthesize the freestanding, binder-free flexible PPy:PSS/CNF nanopaper (PPy:PSS/CNP) electrode by a simple and fast vacuum filtration method. Considering the practical applications, the mechanical and electrochemical properties of the electrodes were adjusted by controlling the weight ratio of PPy:PSS and CNFs. The optimized PPy:PSS/CNP exhibited a high areal specific capacitance, good cycling stability, and prominent flexibility. Moreover, a symmetric supercapacitor device was assembled and delivered a high areal energy density of 122 μWh/cm^2 (15 Wh/cm^3) at a power density of 4.4 mW/cm^2 (550 mW/cm^3), which was better than those of other cellulose-based materials. In light of high supercapacitive performance, flexibility, low cost, and ease of large-scale manufacturing, the PPy:PSS/CNP electrode has a promising application in the next green, economical generation of portable and wearable consumer electronics.

4.2 Experimental section

4.2.1 Materials

The CNFs were purchased from University of Maine (Lot no-U31, 3wt%, grade-91% fines). Pyrrole monomer (99%) was obtained from Tokyo Chemical Industry. Poly(sodium-4-styrenesulfonate) (PSS, 99%) was purchased from Acros,

USA. Ammonium peroxydisulfate (APS, 98%) was purchased from Alfa Aesar. Sulfuric acid (95%-98%) and hydrochloric acid (36.5%-38%) were acquired from VWR, USA. All the chemicals were directly used without any purification.

4.2.2 Preparation of cellulose nanopaper (CNP)

The CNP was prepared by a simple vacuum filtration method according to our previous work [225]. Briefly, the CNFs suspension was diluted to a concentration of 0.5 wt.% with 1 M HCl. The diluted CNFs suspension (40 ml) was continuously stirred for 2 h, then a well dispersed suspension was obtained. Subsequently, the suspension was filtered using a polypropylene filter membrane (diameter of 10 cm, pore size of 0.45 μm). Another polypropylene filter membrane was used to cover the wet CNFs film and dried using a hot plate at 105 ℃ for 2 h to obtain the CNP.

4.2.3 Preparation of PPy:PSS/CNP

The schematic formation of PPy:PSS/CNF composite was shown in **Figure 4.1**. In a typical synthesis process, 40 ml of CNFs suspension (0.5 wt.%) and 20 ml 1 M HCl were added to a reaction vessel and stirred for 30 min to form a well-dispersed suspension. Then pyrrole monomer and PSS were dissolved into the mixture and stirred for another 10 min. Next, APS, acted as an oxidant, was added to initiate the polymerization of pyrrole. The polymerization was carried out for 3-4 h at room temperature under constant magnetic stirring. The as-synthesized PPy:PSS/CNF composite was centrifuged and washed several times with deionized water. Later, the

product was diluted to 200 ml with deionized water and sonicated for 5 min at a power input of 500 W. Finally, the PPy:PSS/CNF suspension was filtered using a polypropylene filter membrane (diameter of 10 cm, pore size of 0.45 μm) by vacuum filtration. Another polypropylene filter membrane was used to cover the wet PPy:PSS/CNF film and dried using a hot plate at 105 ℃ for 2 h to obtain the PPy:PSS/CNP. The weight percentage of PPy:PSS in the PPy:PSS/CNP was calculated following equation (4.1):

$$\text{Wight ratio} = (m - 0.2/m) \times 100\% \quad (4.1)$$

Where *m* was the dry weight (g) of the PPy:PSS/CNP.

In order to obtained optimal performance of composites, the different weight ratio of PPy:PSS in PPy:PSS/CNP were added. The detail was given in **Table 4.1**.

Table 4.1 Operation conditions for synthesizing PPy:PSS/CNP

Sample	CNF (g)	Pyrrole (ml)	PSS (g)	APS (g)	Weight ratio of PPy:PSS (%)
PPy:PSS/CNP-1	0.2	0.1	0.0097	0.228	9.5 ±0.5
PPy:PSS/CNP-2	0.2	0.2	0.0194	0.456	30.6 ±1.1
PPy:PSS/CNP-3	0.2	0.3	0.0291	0.684	44.8 ±1.5
PPy:PSS/CNP-4	0.2	0.4	0.0388	0.912	54.1 ±2.0
PPy:PSS/CNP-5	0.2	0.5	0.0485	1.140	61.6 ±2.3

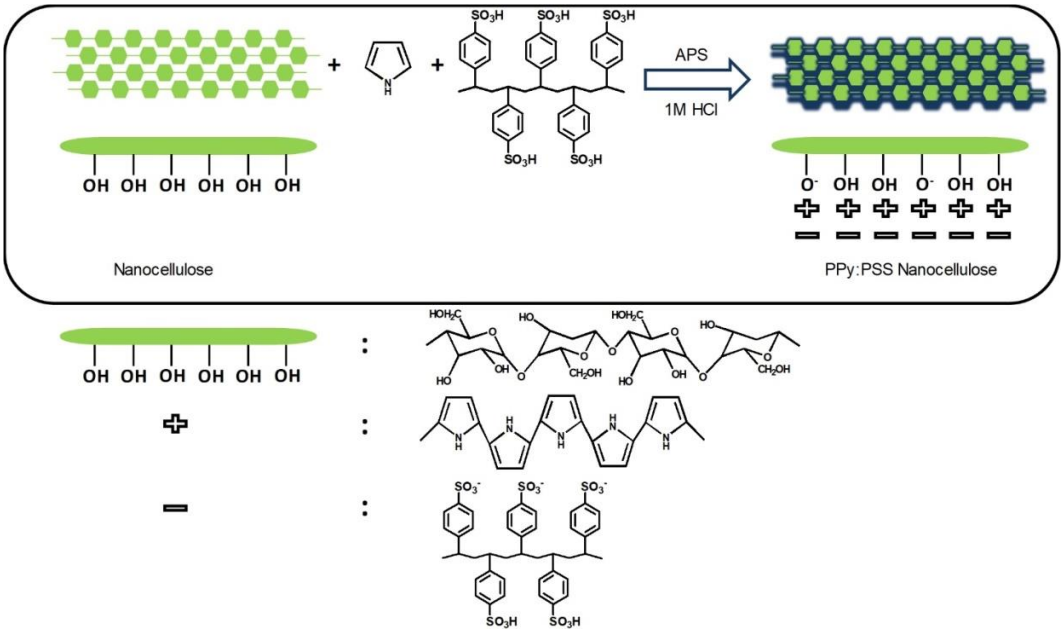

Figure 4.1 The schematic formation of PPy:PSS/CNF composite

4.2.4 Tensile test

Tensile test was carried out by a TA Instrument dynamic mechanical analyzer RSA III with the ASTM standard D882-18 test method. The samples with 1 cm (width) × 5.5 cm (length) segments were used to test. The crosshead speed was 6 mm/min and the gauge length was 15 mm. The data was obtained by averaging three measurements for each sample.

4.2.5 Conductivity measurement

The sheet resistance (R_s) was measured on square specimens (1.5 × 1.5 cm^2) by the four-point probe method using a digital multimeter (RIGOL DM3068). The average value was calculated after five measurements for each sample. The conductivity (ρ, S/cm) was calculated based on equation (4.2) shown as follows [226]:

$$\rho = 1/(R_s \times t) \quad (4.2)$$

Where t is the thickness of the film in centimeter and R_s is the resistance in Ohm.

4.2.6 Electrochemical measurements

The electrochemical measurements were carried out using CHI electrochemical workstation (CHI 760D) in three-electrode and two-electrode systems at room temperature and all the tests were performed in 1 M H_2SO_4. For the three-electrode system, the Ag/AgCl electrode, platinum sheet (1 × 1 cm^2) and PPy:PSS/CNP (1 cm × 1 cm × 0.08 mm, about 15.8 mg) were used as the reference electrode, the counter electrode, and the working electrode, respectively. Cyclic voltammetry (CV) and Galvanostatic charge/discharge (GCD) curves were measured at potentials window of -0.2-0.8 V. The electrochemical impedance spectroscopy (EIS) analysis was conducted at open-circuit voltage using alternative current (AC) amplitude of 0.005 V in the frequency range of 10^{-1} to 10^5 Hz. The stability tests were performed on Arbin Instrument (version 4.21). The symmetric supercapacitor was fabricated by two pieces of film (1 cm × 1 cm × 0.08 mm, about 16 mg) and tested in the two electrode system. CV and GCD curves were recorded over the potentials window of 0-1 V. The areal specific capacitances (C_A, F/cm^2) of electrode can be estimated as equation (4.3) [227],

$$C_A = \int I d_V / A \Delta V s \quad (4.3)$$

Where I is the discharging current (A), $\int I d_V$ is the integrated area of CV curve, A is the area of the electrode (cm^2); s is the scan rate (V/s); and ΔV is the potential

window (V). For the gravimetric capacitance (C_g, F/g) and the volumetric capacitance (C_V, F/cm^3), the area in the formula needed to be replaced by the volume or mass of the electrode, respectively. The energy density was the amount of energy stored per mass/unit volume of active material. For a full device, the energy density and power density were the two key parameters to evaluate the overall performance of a supercapacitor. The areal energy ensity (E, Wh/cm^2) was obtained by

$$\mathrm{E} = C_A \Delta V^2 / (2 \times 3600) \tag{4.4}$$

The energy released per unit time was the power density, which was used to evaluate the speed of the charge and discharge.

$$\mathrm{P} = (3.6 \times E \times s) / \Delta V \tag{4.5}$$

Where, P was the power density (W/cm^2). For the volumetric energy density (Wh/cm^3), the area in the formula needed to be replaced by the volume of the electrode.

4.2.7 Materials Characterization

Scanning Electron Microscopy (SEM; Apreo FE) was used to confirm the morphologies of the samples. The compositional elements were investigated by energy dispersive X-ray spectroscopy (EDS; EDAX Instruments). Fourier transform infrared (FTIR) spectra were measured on a Nicolet 6700 using KBr disk in the wavenumber range of 400-4000 cm^{-1}.

4.3 Results and discussions

4.3.1 Materials characterization

FTIR analysis provided insight into the molecular structure of CNP, PPy:PSS, and PPy:PSS/CNP as shown in **Figure 4.2**. In the spectrum of pure CNP, the bands at 1764, 1616, 1430, 1313, 1161, 1105, 1050, and 894 cm^{-1} were attributed to the stretching of C=O bonds, bending mode of the absorbed water, symmetric bending of $-CH_2$, C-O symmetric stretching, the asymmetric stretching of C-O, C-OH skeletal vibration, pyranose C-O-C stretching, and C-H deformation vibrations out of plane of aromatic ring, respectively [228]. The characteristic vibrational bands of PPy:PSS presented at 1542, and 1440 cm^{-1} corresponding to the stretching of C-C and C-N in the pyrrole ring, respectively. The peak exhibited at 1310 cm^{-1} was assigned to the deforming vibrations of C-H and N-H. The doping state of PPy was confirmed by the peaks at 1170 and 960 cm^{-1}. The absorption peak at 1033 cm^{-1} was due to the sulfur dioxide group stretching vibrations [219, 220, 229]. For PPy:PSS/CNP, the FTIR spectra retained the typical characteristic peaks of PPy:PSS and the cellulose peaks almost disappeared indicating the PPy:PSS was homogeneously coated on the surface of CNFs. Moreover, all the major peaks shifted to the lower frequency, suggesting that the hydrogen bonding formed between CNFs and PPy:PSS. These results confirmed the successful formation of the PPy:PSS/CNP.

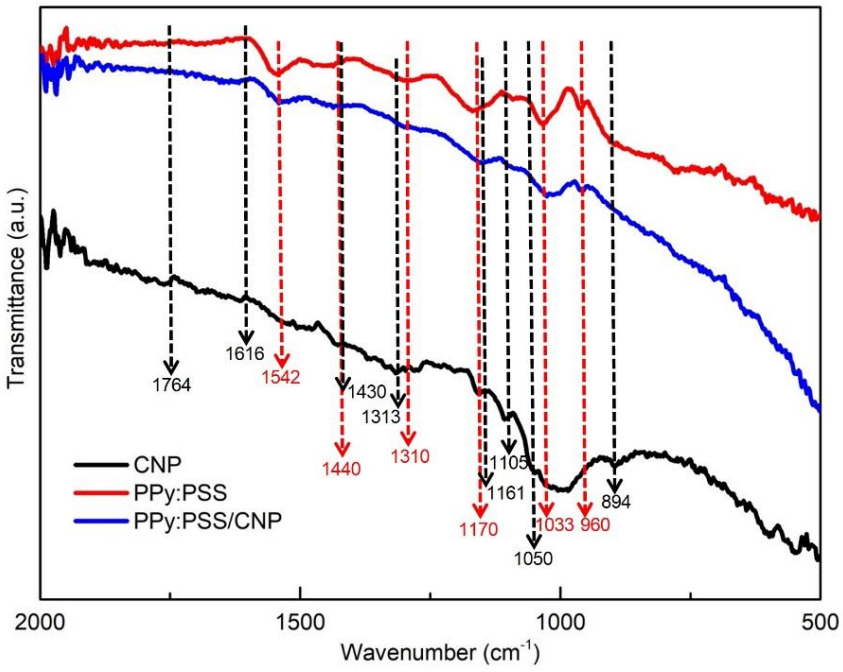

Figure 4.2 FTIR spectra of CNP, PPy:PSS, and PPy:PSS/CNP

The surface and cross-sectional morphology of the pure CNP and PPy:PSS/CNP were examined by SEM under different magnifications. As revealed in **Figure 4.2a**, the pure CNP exhibited a smooth surface and randomly entangled CNFs. The cross-sections showed a compact multilayer configuration that was formed by CNFs tightly entangled with each other through the strong hydrogen bonding (**Figure 4.2b and 4.2c**). These abundant hydrogen bonds provided strong interactions between layers, which reflected the high mechanical properties of CNP. After the introduction of PPy:PSS, the PPy:PSS particles were tightly attached to the surface of CNP, which was mainly due to the hydrogen bonds formed between CNFs and PPy chains, leading to a rougher surface of PPy:PSS/CNP than the pure CNP (**Figure 4.2d**). Besides, EDS proved the existence of sulfur (S) element in PPy:PSS/CNP, further indicating the successful introduction of PPy:PSS on the surface of CNP (**Figure 4.3**). Compared with the pure CNP, the cross-sectional morphology of PPy:PSS/CNP displayed

obviously expanded interior lamellar structures and slightly loose structure, which was probably due to the PPy:PSS within the CNP interrupting the interfibrillar hydrogen bond among CNFs and the refilled PPy:PSS particles enlarging the distance among CNFs (**Figure 4.2e and 4.2f**). The loose structure was expected to favor the electronic transfer and improved the electrochemical performance of active electrode materials.

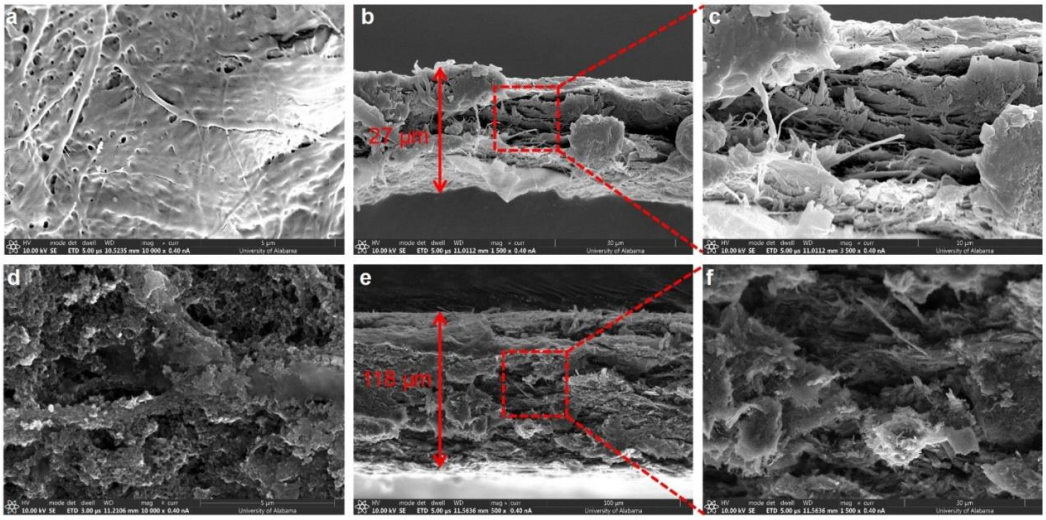

Figure 4.2 SEM surface and cross-section images of (a, b, and c) pure CNP, and (d, e, and f) PPy:PSS/CNP

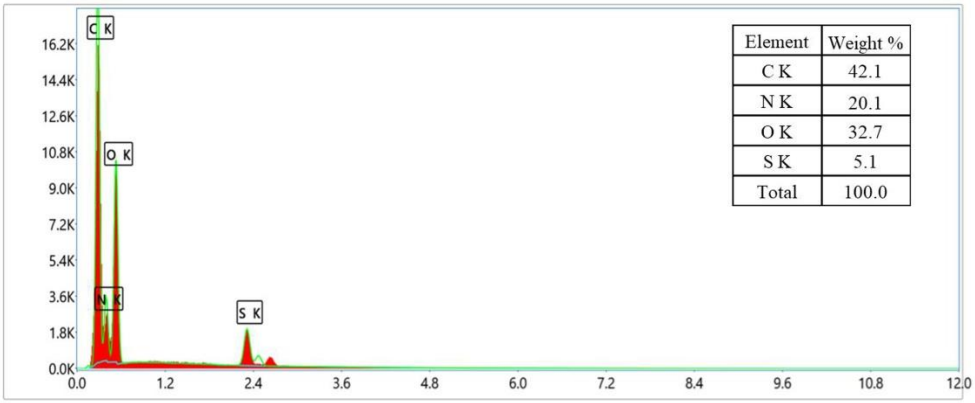

Element	Weight %
C K	42.1
N K	20.1
O K	32.7
S K	5.1
Total	100.0

Figure 4.3 EDS spectra of PPy:PSS/CNP

4.3.2 Mechanical property

The stress vs strain curves and tensile properties of the pure CNP and PPy:PSS/CNP as shown in **Figure 4.4a and 4.4b**. Compared with the pure CNP, the tensile mechanical response of PPy:PSS/CNP decreased distinctly after introducing the PPy:PSS. This result might mainly be due to the disruption of the original CNFs connecting network and the formation of new hydrogen bonds between PPy:PSS and CNFs. It was clear that the connection between the PPy:PSS and CNFs were weaker than the hydrogen bonding interaction among CNFs in CNP, leading to diminished mechanical properties of PPy:PSS/CNP. In addition, the number of intermolecular and intramolecular hydrogen bonds in nanocellulose would be reduced due to the presence of negatively charged PSS (SO^{3-}) between nanocelluloses [230]. With the weight ratio of PPy:PSS increasing, the tensile strength and elongation at break of PPy:PSS/CNP reduced from 42.6 to 9.9 MPa and from 10.17 % to 6.9 %, respectively, since the more amount of PPy:PSS incorporated into the CNP, the fewer the CNF interfibrils connections. This result evidenced that the mechanical properties of PPy:PSS/CNP were affected by the number of hydrogen bonds between fibers. Interestingly, even the weight ratio of PPy:PSS reached 54.1 %, the PPy:PSS/CNP strip with the width and thickness of 10 mm and 0.08 mm, separately, could still lift up a static load of 800 g. By comparing with other conductive polymer/CNF composites, our work presented good mechanical nature [225, 226, 230-232]. It implied that nanocellulose was a promising substrate for the preparation of the flexible electrode.

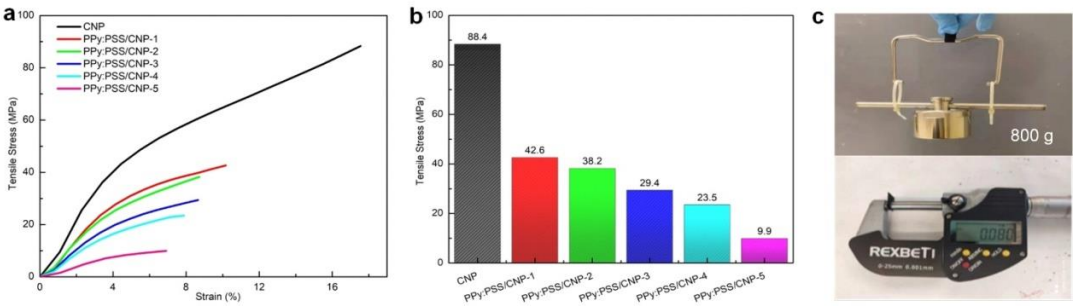

Figure 4.4 (a) Stress vs strain plot and (b) Tensile strength for CNP and PPy:PSS/CNP with different PPy:PSS mass loading; (c) Snapshots of PPy:PSS/CNP-4 strip, which can still lift up a static load of 800 g

4.3.3 Conductivity

As shown in **Figure 4.5a,** the electrical conductivity of PPy:PSS/CNP increased continuously with the increasing amount of PPy:PSS. When the weight ratio of PPy:PSS was 61.6%, the conductivity reached 5.776 S/cm, which suggested that the conductivity of PPy:PSS/CNP mainly attributed to the content of PPy:PSS. However, despite a high mass loading of conductive active material could improve the supercapacitor performance, the poor mechanical strength nature of PPy:PSS/CNP-5 that might limit its practical application still should be considered. It is worth noting that even the mass load of PPy:PSS was reduced to 54.1%, the PPy:PSS/CNP could still exhibit high conductivity of 4.456 S/cm in this work, which was higher than many similar conductive composites reported previously, such as PPy/CNF (0.26 S/cm), CNF/poly(3,4-ethylenedioxythiophene) (PEDOT):PSS (2.58 S/cm), and PPy/acrylic acid (AA) grafted nanocrystal cellulose hydrogel (PPy/NCC-g-AA) (8.8 $\times 10^{-3}$ S/cm) [226, 230, 233]. **Figure 4.5b** demonstrated that PPy:PSS/CNP-4 as a

connecting lead could light LED bulb very well under different bending angles, suggesting their splendid conductance stability and flexibility. Combining the mechanical strength of PPy:PSS/CNP-4, it was an optimal electrode candidate used for the electrochemical test.

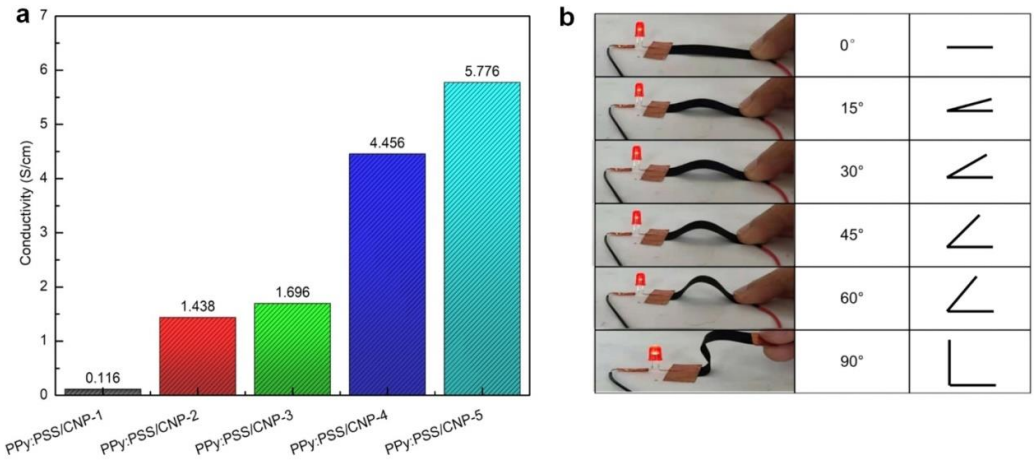

Figure 4.5 (a) Conductivity and (b) Photographs of PPy:PSS/CNP-4 films with different bending angles

4.3.4 Electrochemical characterization

Figure 4.6a presented the CV curves of PPy:PSS/CNP-4 at various scan rates. A quasi-rectangular shape was exhibited under lower scan rates, corresponding to a good pseudocapacitive response. With the increasing of scan rates, the curves distorted into a leaf-like shape. The deviation of CV curves was mainly due to the controlled ion diffusion process impeding the accessibility of ions and active sites and causing the charge collection at the solid/liquid interface, which increased the internal diffusion resistance of the electrode. There are no obvious redox peak observed, suggesting that the fast electron and ion transfer throughout the electrodes [234-236].

The charge-discharge performance of PPy:PSS/CNP-4 was shown in **Figure 4.6b**. All the GCD curves were found to be nearly triangular shapes with a very small voltage drop indicating superior pseudocapacitive behavior and excel lent reversibility of ion transfer and diffusion properties for the electrode. Based on the CV curves, the specific capacitances for the area, volume, and weight were calculated as shown in **Figure 4.6c and 4.6d**. The maximum specific capacitance value was 3.8 F/cm^2 (475 F/cm^3, 240 F/g) at 10 mV/s. Compared with other cellulose-based conductive nanopapers in the **Table 4.2**, our work had a highest value. From 10 to 40 mV/s, and 62 % of initial area capacitance was retained. The loss of capacitance could be explained by the increase of the internal resistance due to the diffusion limitations of electrolyte ions into electrode material which could not match the rate of the electron transfer of electrode materials. The superior rate performance of PPy:PSS/CNP-4 was ascribed to the high conductivity of PPy and the synergistic effect between PPy:PSS and CNFs, which could lower interfacial charge-transfer resistance and facilitate the transportation of electrons. EIS was conducted to analyze the intrinsic charge storage of the electrode. As displayed in **Figure 4.6e**, the Nyquist plot showed a small semicircle in the high-frequency region that related to the charge transfer resistance of the electrode and a straight line in the low-frequency region corresponding to Warburg impedance reflecting the capacitive behavior of the electrode. This observation further proved that the PPy:PSS/CNP-4 electrode possesses a low charge transfer resistance and a fast charge transfer rate performance. Moreover, PPy:PSS/CNP-4 demonstrated remarkable cycling stability (80.9% capacitance retention, 5,000 cycles) due to the

incorporation of cellulose network with good mechanical strength that could effectively overcome the shortcomings of the volume expansion/shrinkage for PPy during the charging/discharging processes (**Figure 4.6f**). The mechanical properties of PPy:PSS/CNP-4 were further confirmed after the cycling stability test (5,000 cycles) in the three-electrode system. As displayed in **Figure 4.7**, the tensile stress of PPy:PSS/CNP-4 remarkably decreased from 23 MPa to 4.8 MPa. The decreasing tensile stress for PPy:PSS/CNP-4 might mainly attribute to the water molecule that interrupts the hydrogen bond among composites[237]. **Figure 4.8a and 4.8b** presented the CV curves and digital photos of PPy:PSS/CNP-4 at different bending angles. The CV curves showed a minimal deformation further demonstrating the stable performance of the electrode.

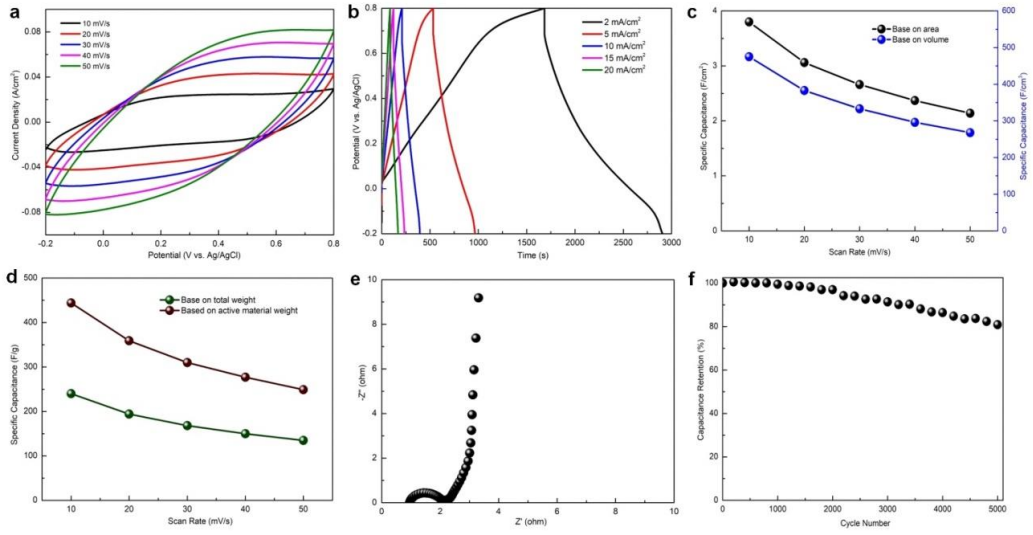

Figure 4.6 The electrochemical performance of PPy:PSS/CNP-4 electrode in 1 M H_2SO_4 electrolyte. (a) CV curves; (b) GCD curves; (c) Specific capacitance based on areal and volume as functions of current density; (d) Specific capacitance based on total weight and active material weight as functions of current density; (e) Nyquist plot; (f) Cycling stability at 10 mA/cm^2

Table 4.2 Comparison of PPy:PSS/CNP electrode with reported nanocellulose supported conductive material based supercapacitors

Electrode materials	Specific capacitance	Capacitance retention (Cycles)	Ref
CNF/CNT/PANI	315 F/g, at 1 A/g	10000, 92.0%	[238]
CF-CNF/AC/MWCNT	1.74 F/ cm^2, at 1 mA/cm^2	3000, 96.7%	[239]
PPy/rGO/CNF	304 F/g, at 0.5 A/g	1000, 81.8%	[240]
PPy/cellulose	129.6 F/g, at 0.48 A/g	7000, 99.3%	[241]
RGO/cellulose	212 F/ g, at 0.5 A/g	14000, 94.0%	[242]
PEDOT/Cellulose Paper	115 F/g, at 1 A/g	2500, 91.0%	[243]
PEDOT:PSS/CNP	854.4 mF/cm^2 (106.8 F/cm^3) (159.7 F/g), at 5 mV/s	10000, 95.5%	[225]
PPy/GR/CNF	264.3 F/g, at 0.25 A/g	1000, 85.7%	[244]
PPy:PSS/CNP	3.8 F/cm^2 (475 F/cm^3, 240 F/g) at 10 mV/s	5000, 80.9%	**This work**

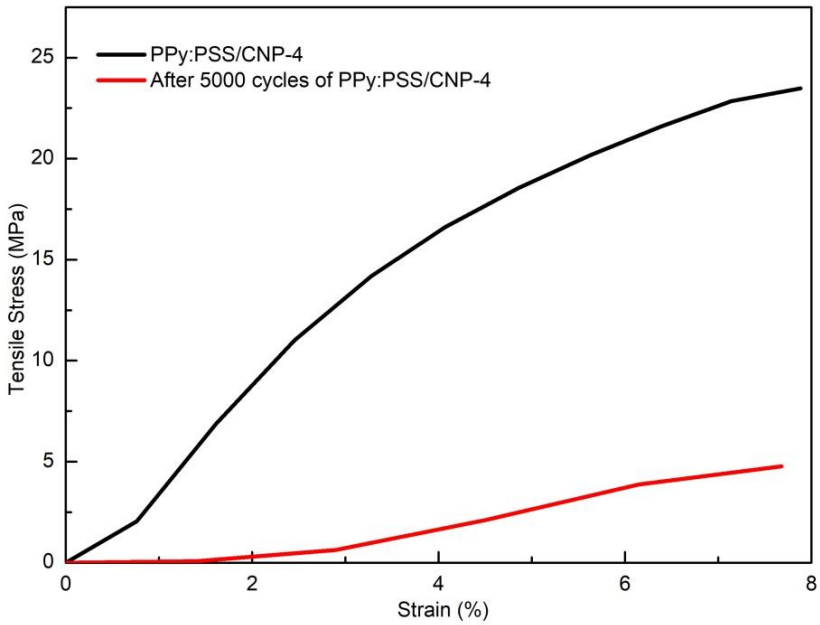

Figure 4.7 Stress vs strain plot of PPy:PSS/CNP-4 and PPy:PSS/CNP-4 after the cycling stability test (5000 cycles) in the three-electrode system

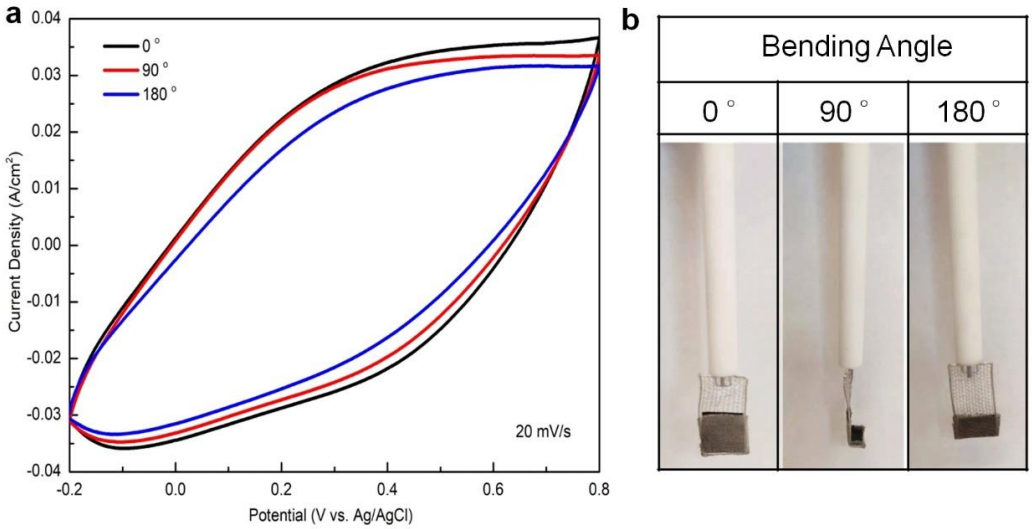

Figure 4.8 (a) CV curves and (b) digital photos of PPy:PSS/CNP-4 at different bending angles

To evaluate the practical application of PPy:PSS/CNP-4 film electrode, the electrochemical characterization of the symmetric supercapacitor that assembled by two pieces of PPy:PSS/CNP-4 electrode (1×1 cm^2) was performed. The symmetric

device exhibited the symmetrical shape of CV curves and negligible deformations with the increasing scan rates, indicating the ideal capacitive, excellent rate feature, and good reversibility (**Figure 4.9b**). GCD curves displayed nearly triangle shape with low voltage drops which further proved a typical electric double layer capacitor (EDLC) nature of energy storage (**Figure 4.9c**). In addition, as the current density increases, the shape of the GCD curves remained, indicating that the device had good redox reversibility. The capacitance values of PPy:PSS/CNP-4 device based on area, volume, and weight were plotted in **Figure 4.9d and 4.9e** to value the performance of supercapacitors. At 10 mV/s, the maximum areal capacitance was 880 mF/cm^2 (110 F/cm^3, 50.8 F/g). The results of the cyclic performance indicated that the device showed 74% capacitance retention after 5800 cycles at 5 mA/cm^2 **(Figure 4.9f)**. As shown in the Ragone plots (**Figure 4.10a and 4.10b**), the maximum energy density could reach 122$\mu Wh/cm^2$ (15 Wh/cm^3) with the power density of 4.4 mW/cm^2 (550 mW/cm^3), which was comparable to or even higher than the previous SCs devices based on similar cellulose materials, demonstrating the satisfied electrochemical performance [40-49][132, 160, 245-252]. The impressive findings suggested that the PPy:PSS/CNP was a promising material for high performance energy storage devices.

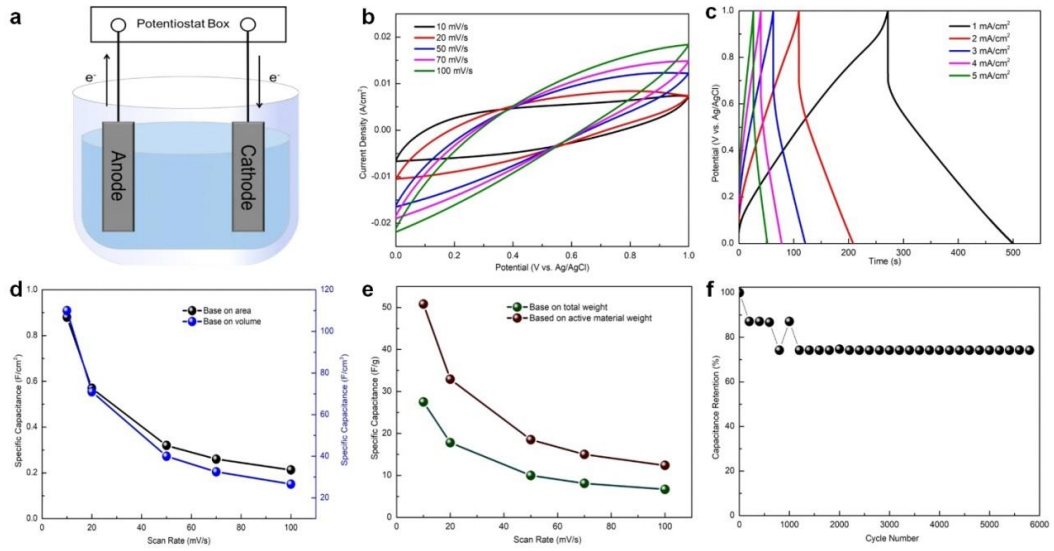

Figure 4.9 (a) Schematic illustration of the PPy:PSS/CNP supercapacitor device; (b) CV curves at different scan rate; (c) GCD curves at different current density; (d) Specific capacitance based on area and volume; (e) Specific capacitance based on total weight and active material weight; (f) Cycling stability at 5 mA/cm^2

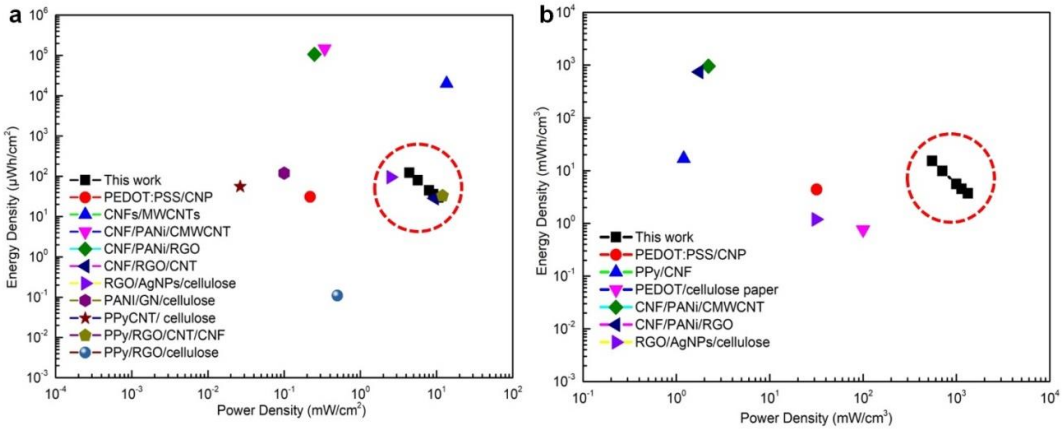

Figure 4.10 Ragone plots the symmetrical PPy:PSS/CNP supercapacitor device based on (a) area and (b) volume in comparison with other cellulose materials

4.4 Conclusions

In this study, the low-cost and environmentally friendly nanocellulose were used as building blocks for PPy:PSS to fabricate the freestanding, binder-free flexible

PPy:PSS/CNP electrode using the vacuum filtration method. Due to the synergistic effect of three constituents, the PPy:PSS/CNP exhibited excellent flexibility and outstanding electrochemical properties. When the weight percentage of PPy:PSS to PPy:PSS/CNP was 54.1%, the electrode exhibited the maximum specific capacitance value (3.8 F/cm^2, 475 F/cm^3, 240 F/g, at 10 mV/s) and good cycling stability (80.9% capacitance retention rate, 5,000 cycles). The good flexibility and electrochemical stability of the electrode was proved by the CV curves of PPy:PSS/CNP at different bending angles. Furthermore, the symmetric supercapacitor device of PPy:PSS/CNP was assembled, which offered the highest areal energy density of 122 $\mu Wh/cm^2$ (15 Wh/cm^3) along with the power density of 4.4 mW/cm^2 (550 mW/cm^3). Our work provides a novel design idea to synthesize free-standing flexible nanopaper electrode with good mechanical strength and electrochemical performance for energy storage applications in the future. Moreover, the simple and economical preparation process may bring new opportunities in reducing the production cost of flexible electrodes for portable and wearable consumer electronics.

Chapter 5: Flexible and freestanding PANI: PSS/CNF nanopaper electrodes with enhanced electrochemical performance for supercapacitors

Abstract: A novel freestanding, binder-free flexible polyaniline:poly(sodium 4-styrene sulfonate)/cellulose nanopaper (PANI: PSS/CNP) electrode was prepared by combining in situ polymerization with a simple and fast vacuum filtration method. The low-cost and environmental-friendly nanocellulose with a three-dimensional (3D) hierarchical porous structure was chosen as the support substrate not only effectively reduced the production cost but improved the electrolyte absorption property, flexibility, and mechanical strength for PANI: PSS/CNP. The free-standing and binder-free structure simplifying the preparation process and increasing the mass loading of the active material in the electrode is beneficial to maximizing electrode utilization. Due to the effective combination of the cellulose (CNF) and PANI: PSS complex, the optimized PANI: PSS/CNP electrode exhibits high specific capacitance (2.56 F/cm^2) with good cycling stability (81.5% capacitance retention, 8000 cycles), excellent mechanical strength, good conductance stability, and flexibility. A symmetric supercapacitor constructed with two pieces of PANI: PSS/CNP electrodes shows outstanding areal specific capacitance of 460 mF/cm^2 and high energy density of 40.9 $\mu Wh/cm^2$. Our work offers a scientifically and economically efficient approach for the production of low-cost and energy-efficient flexible electrodes used for future green flexible electronics devices through straightforwardly fabricating conductive compounds using cellulose of natural origin.

5.1 Introduction

With the rapidly growing industries and markets of portable and wearable consumer electronics such as foldable displays, electronic skin, and electric paper, the demand for flexible and renewable energy storage devices with low-cost, lightweight, environmental friendliness, and superior energy efficiency is clearly increasing [153, 163-165]. Among various energy storage devices, flexible supercapacitors have been widely recognized as promising candidates due to their high power density, long cycling life, robust mechanical flexibility, and good operational safety [166-168, 253, 254]. As the most important part of flexible supercapacitors, the flexible electrode is considered as a key impact on the successful fabrication of high-performance flexible supercapacitors.

Polyaniline (PANI) as a promising electrode material has been studied extensively in supercapacitors owing to its high specific capacitance, facile and simplistic preparation, easy control of doping level and conductivity, good environmental stability, and low cost [255, 256]. However, the weak solubility in common solvents, structural instability, and poor mechanical performance of PANI limit its applications in flexible electronic devices. A common method used to overcome the insolubility problem of conducting polymer is to combine polymeric surfactants with different sulfonating groups and conducting polymer to form complexes [257, 258]. For instance, the polyaniline: poly(sodium 4-styrene sulfonate) (PANI: PSS) with excellent solution-processability and unique redox behaviors has been widely applied in supercapacitors. A hybrid electroactive material formed by

iron oxide-decorated few-layer graphene/PANI: PSS composite films through a simple dip-coating procedure showed excellent capacitive performance [259]. The "sandwich-like" nanocomposites multiwalled carbon nanotubes/polyaniline/ poly(sodium 4-styrenesulfonate)-graphene (MWCNTs/PANI/PSS-GR) demonstrated a high specific capacitance [260]. In addition, extensive work has been done to modify and improve the electrochemical performance of PANI such as preparing different morphologies of PANI, making composites with carbon-based materials, and depositing active conducting materials on flexible, porous, and light-weight substrates [261-266].

Cellulose (CNF), the most abundant natural polymer on earth, has received great attention, in light of its abundant and renewable raw materials source, high surface area, superior mechanical strength, non-toxicity, great biocompatibility and biodegradability, and prospect for environmental sustainability, etc [208]. The three-dimensional (3D) hierarchical porous structures of cellulose formed through the intramolecular and intermolecular hydrogen bonds among cellulose molecules provide rich ion absorptive sites and more diffusion channels for charge transfer, which is beneficial for enhancing the performance of supercapacitors [267]. Furthermore, the hydroxyl groups can be easily modified and provide a good platform for the construction of new materials to broaden their potential applications. Compared with other flexible substrates, CNF is widely regarded as an ideal building block to reduce production costs and building environmental-friendly processes for fabricating the functional flexible electrodes. A series of cellulose-based functional

materials have been fabricated and applied in flexible energy-storage devices. For example, Deng et al. prepared multiwalled carbon nanotube (MWNT)/activated CNF (ACNF) whose capacitance was 1.38 times higher than that of pure ANCF, when adding 6 wt% MWNTs in CNFs. In addition, 94% initial capacitance was retained over 1000 cycles at the current density of 2 A/g [268]. Uniform cellulose/graphene/polypyrrole (CNF/GN/PPy) microfibers were prepared with a convenient wet-spinning strategy. This microfiber electrode manifested excellent tensile strength (364.3 MPa), high specific capacitance (334 mF/cm^2), and good cycling stability (capacitance retaining nearly 100% after 2000 charge-discharge cycles) [269].

In this study, we aim to develop a sustainable and inexpensive strategy to synthesize flexible electrodes with high electrochemical performance to meet the requirements of the global markets for flexible and renewable energy storage devices. Here, we designed and prepared a new freestanding, binder-free flexible polyaniline: poly(sodium 4-styrene sulfonate)/cellulose nanopaper (PANI: PSS/CNP) electrode through in situ polymerization and a fast vacuum filtration method, which combines the solution-processable PANI: PSS complexes as the active material with CNF as the flexible substrate. The cheap and green CNF as a substrate can not only effectively reduce the production cost but also improve the flexibility and mechanical strength of electrodes. The optimized PANI: PSS/CNP electrode exhibited high tensile strength, where the sample strips (10 mm wide and 0.1 mm thick) could still lift up a static load of 800 g. The free-standing and binder-free construction eliminates the need for

binders, conductive additives, and current collectors while simplifying the preparation process and increasing the mass loading of the active material in the electrode, and maximizing electrode utilization. The optimized PANI: PSS/CNP demonstrated a high areal specific capacitance of 2.56 F/cm^2 and good cycling stability (81.5 % capacitance retention, 8000 cycles). A symmetric supercapacitor assembled with two pieces of PANI: PSS/CNP electrodes delivered a high areal energy density of 40.9 μWh/cm^2 (4.09 mWh/cm^3) at a power density of 100.5 μW/cm^2 (10.05 mW/cm^3). This research opens a new avenue for developing low-cost and free-standing flexible electrodes of supercapacitors.

5.2 Experiments

5.2.1 Materials

The CNFs with a concentration of about 3 wt% were purchased from the University of Maine, USA. (Lot Number U31). Aniline monomer (99%) and ammonium peroxydisulfate (APS, 98%) were purchased from Alfa Aesar. Poly(sodium-4-styrenesulfonate) (PSS, 99%) was purchased from Acros, USA. Sulfuric acid (H_2SO_4, 95%-98%) and hydrochloric acid (HCl, 36.5%-38%) were purchased from VWR, USA. All the chemicals were directly used without further purification.

5.2.2 Preparation of cellulose nanopaper (CNP)

The preparation of CNP was carried out according to our previous work [225]. In

short, the CNFs suspension with a concentration of 0.5 wt% was diluted by 1 M HCl. The diluted CNFs suspension (40 ml) was magnetically stirred for 2 h to obtain a uniform suspension. Then, the suspension was filtered using a polypropylene filter membrane (diameter of 10 cm, pore size of 0.45 μm) by a vacuum filtration method. Finally, another polypropylene filter membrane was covered on the wet CNF film and dried at 105 ℃ for 2 h to obtain the CNP.

5.2.3 Preparation of PANI: PSS/CNP

40 ml of CNF suspension (0.5 wt%) was dispersed in 20 ml 1 M HCl and stirred for 30 min to form a homogeneous suspension. Then aniline monomer and PSS were introduced into the suspension and stirred for another 10 min. Next, the oxidant of APS was added into the mixture to initiate the polymerization of aniline. The reaction was carried out for 3-4 h under constant magnetic stirring at room temperature. The resultant solid was centrifuged and washed several times with deionized water. After that, the product was diluted to 200 ml with deionized water and sonicated for 5 min at a power input of 500 W. Finally, the PANI: PSS/CNF suspension was filtered by vacuum filtration using a polypropylene filter membrane (diameter of 10 cm, pore size of 0.45 μm). The PANI: PSS/CNP was obtained by drying the wet PANI: PSS/CNF film that was covered by another polypropylene filter membrane at 105 ℃ for 2 h. The schematic of forming the PANI: PSS/CNP is shown in **Figure 5.1**, where PSS acts a as surfactant as well as a dopant in the composite. The weight percentage of PANI: PSS in the PANI: PSS/CNP was calculated following Equation (5.1):

$$\text{Wight ratio} = (m - 0.2/m) \times 100\% \quad (5.1)$$

Where *m* is the dry weight (g) of the PANI: PSS/CNP.

To obtain optimal performance of composites, the weight ratio of PANI: PSS in PANI: PSS/CNP was accurately controlled. The detail was given in **Table 5.1**.

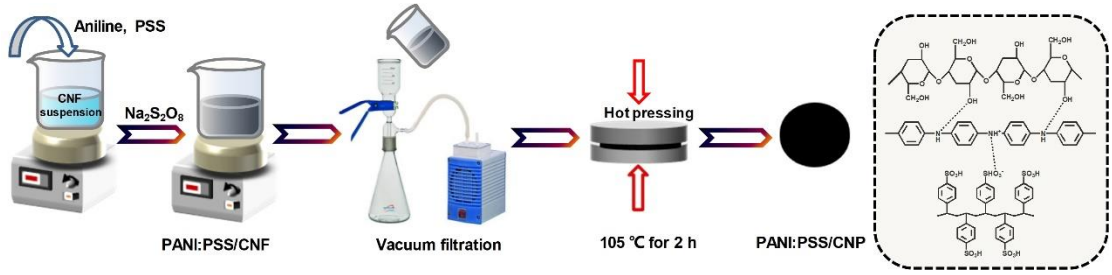

Figure 5.1. The schematic formation of PANI: PSS/CNP

Table 5.1 Operation conditions for synthesizing PANI: PSS/CNP

Sample	CNF (g)	Aniline (ml)	PSS (g)	APS (g)	Weight ratio of PANI: PSS (%)
PANI: PSS/CNP-1	0.2	0.1	0.0097	0.228	7.7 ± 0.3
PANI: PSS/CNP-2	0.2	0.2	0.0194	0.456	29.0 ± 0.8
PANI: PSS/CNP-3	0.2	0.3	0.0291	0.684	46.8 ± 1.2
PANI: PSS/CNP-4	0.2	0.4	0.0388	0.912	54.1 ± 1.5
PANI: PSS/CNP-5	0.2	0.5	0.0483	1.140	62.2 ± 1.8

5.2.4 Tensile test

The mechanical properties of PANI: PSS/CNP samples were examined by the TA Instrument dynamic mechanical analyzer RSA III with the ASTM standard D882-18 test method. The specimens were cut into the 1 cm (width) × 5.5 cm (length) segments used to test. The crosshead speed and gauge length were 6 mm/min and 15 mm,

respectively. Three measurements data were averaged to obtain the value for each sample.

5.2.5 Conductivity measurement

The electric conductivity (ρ, S/cm) of PANI: PSS/CNP was examined by the four-point probe method using a digital multimeter (RIGOL DM3068) and calculated by Equation (5.2) [226],

$$\rho = 1/(R_s \times t) \quad (5.2)$$

Where R_s is the sheet resistance in Ohm, which is the average value after five square specimens (1×1 cm^2) measured for each sample. t is the thickness of the film in centimeter.

5.2.6 Electrochemical measurements

All the electrochemical tests were carried out on a CHI electrochemical workstation (CHI 760D) using three-electrode or two-electrode systems in 1 M H_2SO_4. The reference electrode, the counter electrode, and the working electrode were Ag/AgCl electrode, platinum sheet (1×1 cm^2), and PANI: PSS/CNP (1 cm × 1 cm × 0.10 mm, 11 mg), respectively. Cyclic voltammetry (CV) and Galvanostatic charge/discharge (GCD) curves were conducted with the potentials window from 0 to 0.8 V. The PANI: PSS/CNP electrode (1 cm × 1 cm × 0.10 mm, 11 mg) was employed as both cathode and anode to build the symmetric supercapacitor. Electrochemical impedance spectra (EIS) were obtained at open-circuit voltage using

AC amplitude of 0.005 V in the frequency range of 10^{-1} to 10^{5} Hz. The stability tests were performed on Arbin Instrument (version 4.21). The areal specific capacitance (C_A, F/cm^2) of the electrode was estimated by the Equation (5.3) from the GCD curves [270],

$$C_A = I\Delta t / A\Delta V \tag{5.3}$$

Where I is the discharge current (A), Δt is discharge time (s), A is the area of the electrode (cm^2), and ΔV is the potential window (V). When the area in the formula is replaced by the volume or mass of the electrode, the gravimetric capacitance (C_g, F/g) and the volumetric capacitance (C_V, F/cm^3) will be obtained.

The energy density (E, Wh/cm^2) and power density (P, W/cm^2) were calculated according to the following Equations 5.4 and 5.5:

$$\mathrm{E} = \mathrm{C}\Delta V^2/(2 \times 3600) \tag{5.4}$$

$$\mathrm{P} = (3600 \times E)/\Delta t \tag{5.5}$$

5.2.7 Materials Characterization

Scanning Electron Microscopy (SEM; Apreo FE) and energy dispersive X-ray spectroscopy (EDS; EDAX Instruments) were used to confirm the morphologies and compositional elements of the samples, respectively. The function groups were investigated by Fourier transform infrared spectroscopy (FTIR) on a Nicolet 6700 using KBr disk in the region of 400-4000 cm^{-1}. X-ray photoelectron spectroscopy (XPS, Kratos XSAM 800) was used to determine the elemental valence state of the samples.

5.3 Results and discussions

5.3.1 Materials characterization

Structural characterization of CNP, PANI: PSS, and PANI: PSS/CNP was investigated by FTIR as shown in **Figure 5.2**. The pure CNP exhibits a few peaks including the bending mode of the absorbed water at 1645 cm^{-1}, symmetric bending of $-CH_2$ at 1430 cm^{-1}, O-H bending at 1369 cm^{-1}, C-O symmetric stretching at 1315 cm^{-1}, asymmetric stretching of C-O at 1161 cm^{-1}, C-OH skeletal vibration at 1105 cm^{-1}, pyranose C-O-C stretching at 1050 cm^{-1}, and deformation vibrations out of the plane of the aromatic ring at 896 cm^{-1}, respectively [228]. In the spectrum of PANI: PSS, the bands at 1556, and 1483 cm^{-1} correspond to C=C stretching vibrations of the quinoid and benzenoid rings, respectively. The peak presented at 1290 cm^{-1} is assigned to C-N stretching of secondary aromatic amine. The peaks at 1108, 1029, and 1002 cm^{-1} belong to the benzene ring in-plane vibration. The absorption peak at 663 cm^{-1} is due to the C-S stretching vibration of the benzene ring of PSS [271-273]. The FTIR spectrum analysis confirmed the successful doping of PSS into PANI. As shown in the spectrum of PANI: PSS/CNP, typical characteristic peaks of PANI: PSS (C=C (quinoid rings), C=C (benzenoid rings), and C-N) are observed, and the cellulose peaks almost disappear, indicating that PANI: PSS is uniformly coated on the CNF surface. Furthermore, compared with the spectrum of PANI: PSS, the peaks of PANI: PSS/CNP is slightly shifted to low frequencies, which can be attributed to the formation of hydrogen bonds between CNF and PANI: PSS. This result proves the

successful synthesis of the PANI: PSS/CNP.

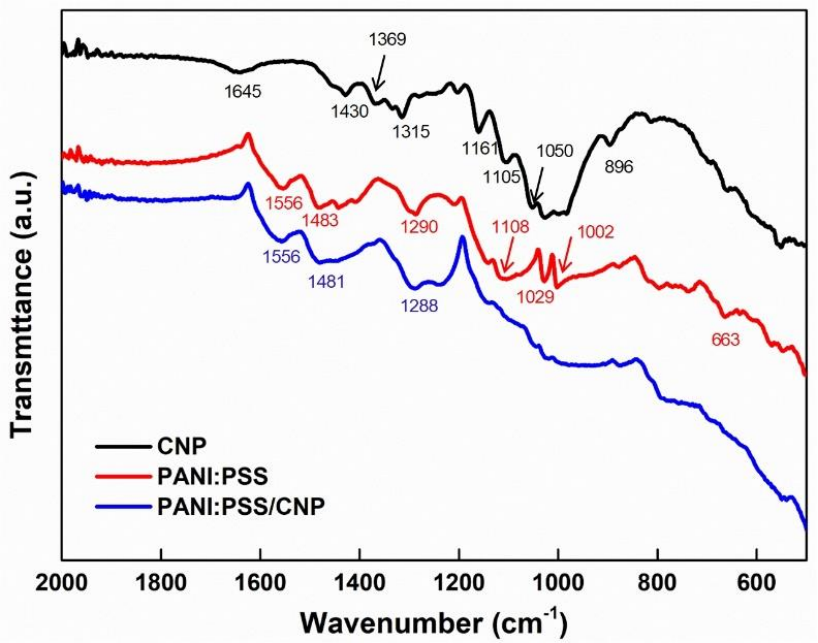

Figure 5.2 FTIR spectra of CNP, PANI: PSS, and PANI: PSS/CNP

XPS analysis was further performed to elucidate the chemical structure of PANI: PSS/CNP. As presented in **Figure 5.3a**, the XPS survey spectra of PANI: PSS/CNP exhibits four main peaks located at 532 eV, 399 eV, 284 eV, and 164 eV corresponding to O1s, N1s, C1s, and S2p, respectively [228, 274]. The peak for N1s is from PANI, while the S2p is attributed to PSS. The N1s core-level spectrum is divided into three peaks situated at 401.06 eV (−N^+−), 399.81 eV (−NH−), and 398.88 eV (−N=), respectively (**Figure 5.3b**) [275, 276]. Additionally, the ratio of N^+/N is 50.6% indicating a high N-doping level of PANI, which is beneficial to improving the pseudocapacitive performance of electrodes [250].

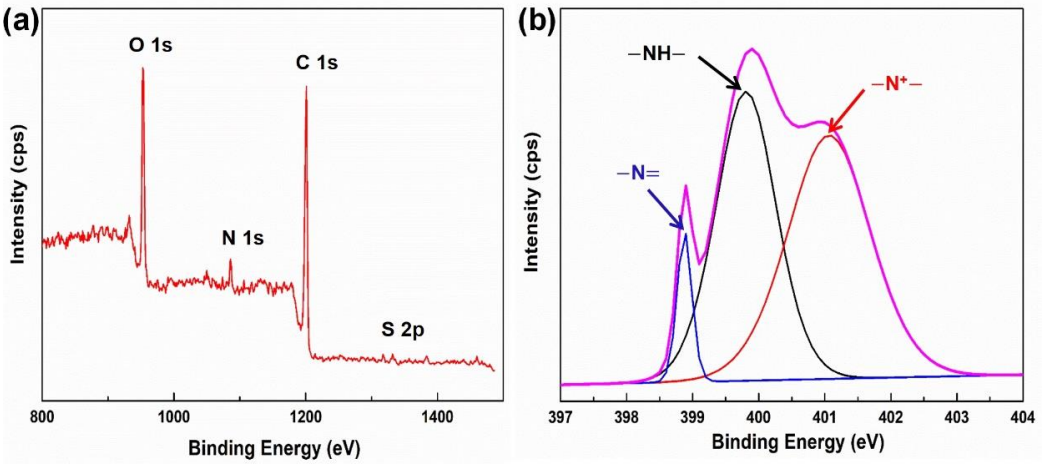

Fig.2. (a) XPS survey spectra of PANI: PSS/CNP; (b) N1s spectra of PANI: PSS/CNP

The morphology of pure CNP and PANI: PSS/CNP was investigated by SEM. As shown in **Figure 5.4a**, the surface of pure CNP is smooth and shows an entangled nanofiber network. The cross-sectional images display a lamellar structure formed by CNFs tightly entangled with each other through the strong hydrogen bonding (**Figure 5.4b and 5.4c**). CNP with a compact multilayer configuration is chosen as the flexible substrate, which is beneficial for high mechanical properties and fast electrolyte ions diffusion of the electrode [224, 277]. **Figure 5.4d** confirms that PANI: PSS particles aggregate on the surface of CNP resulting in a rougher surface of PANI: PSS/CNP after the introduction of PANI: PSS compared to pure CNP, which gives the electrode a high surface area to perform a better contact with the electrolyte [250]. Moreover, the EDS elemental mappings of carbon (C) and nitrogen (N) further demonstrate the formation of PANI: PSS on the surface of CNP (**Figure 5.5**). The uniformly distributed PANI: PSS particles on the surface of CNF may be attributed to the hydrogen bond between CNF and PANI chains [244]. The expanded interior lamellar cross-sectional structures of PANI: PSS/CNP evidenced that PANI: PSS particles

penetrated into the substrate, not only coated on the surface of CNP. Such structure offers the obtained electrode excellent electrical conductivity and shorts the diffusion distance of ions, leading to high electrochemical properties.

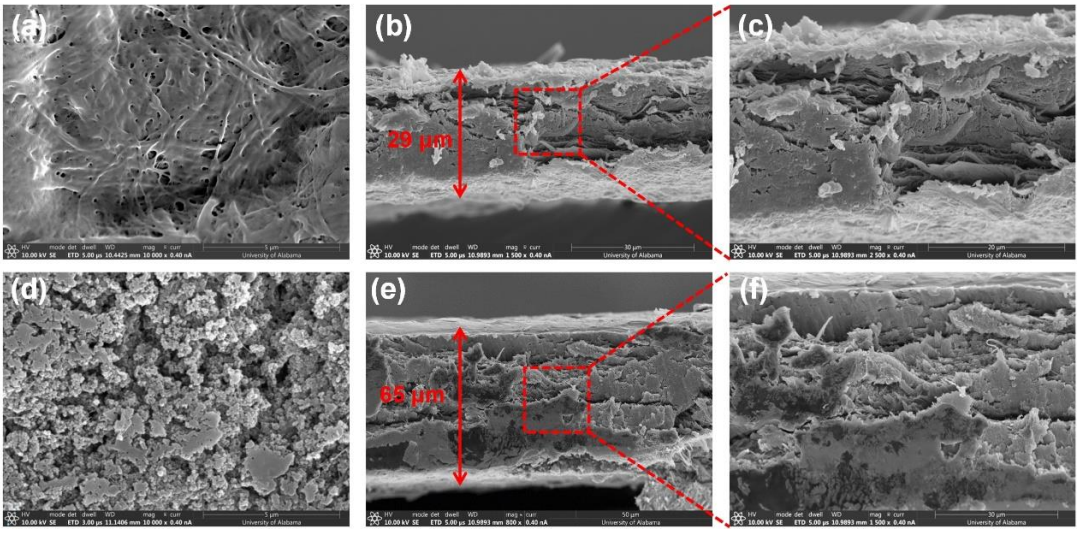

Figure 5.4. (a, b, and c) SEM surface and cross-section images of pure CNP, and (d, e, and f) PANI: PSS/CNP

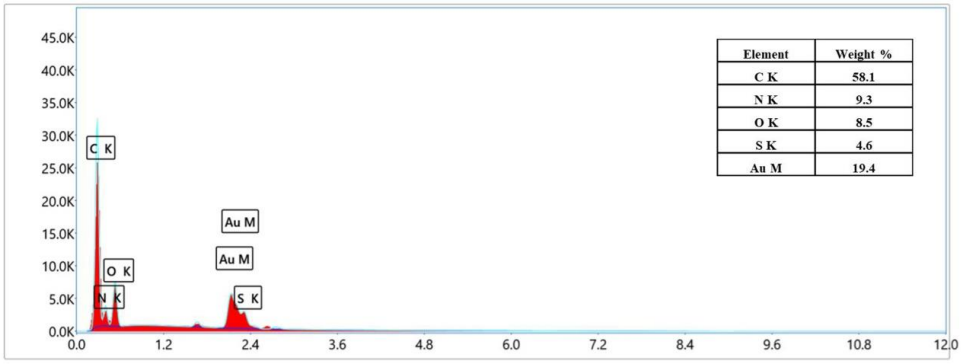

Figure 5.5 EDS spectra of PANI: PSS/CNP

5.3.2 Mechanical property

The mechanical characteristics of pure CNP and PANI: PSS/CNP was investigated by a stress-strain experiment. As shown in **Figure 5.6a and 5.6b,** the tensile stress and strain of PANI: PSS/CNP decreased distinctly compared with pure

CNP. This degraded behavior of PANI: PSS/CNP in terms of mechanical properties may be related to the disruption of the original CNF connecting network and the formation of new hydrogen bonds between PANI: PSS and CNF after the introduction of PANI: PSS. This result is matching with FTIR. It is obvious that the PANI: PSS-CNF interactions are inherently weaker than CNF-CNF, resulting in decreased mechanical properties of PANI: PSS/CNP [278-280]. Furthermore, with the increase of PANI: PSS content, the tensile strength of PANI: PSS/CNP decreases from 49.98 MPa with a fracture strain of 14.11 % to 14.28 MPa with a fracture strain of 6.83 %. This phenomenon can be explained by the percentage reduction of CNFs content in PANI: PSS/CNP. The higher percentage content of CNFs in the composites typically leads to more intramolecular and intermolecular hydrogen bonds among CNFs in the PANI: PSS/CNP, which endows the composites with higher mechanical strength. Conversely, the existence of PANI: PSS will prevent the formation of a large number of hydrogen bonds, and therefore lower the mechanical strength [281]. This result evidences that the number of hydrogen bonds among CNFs affects the mechanical properties of PANI: PSS/CNP. In addition, when the PANI: PSS/CNP was sliced into 10 mm wide with 0.1 mm thick strips, the sample could still lift up a static load of 800 g, where the weight ratio of PANI: PSS is 54.1 % in PANI: PSS/CNP. It implies that PANI: PSS/CNP has excellent mechanical strength, which enables practical applications in flexible supercapacitors.

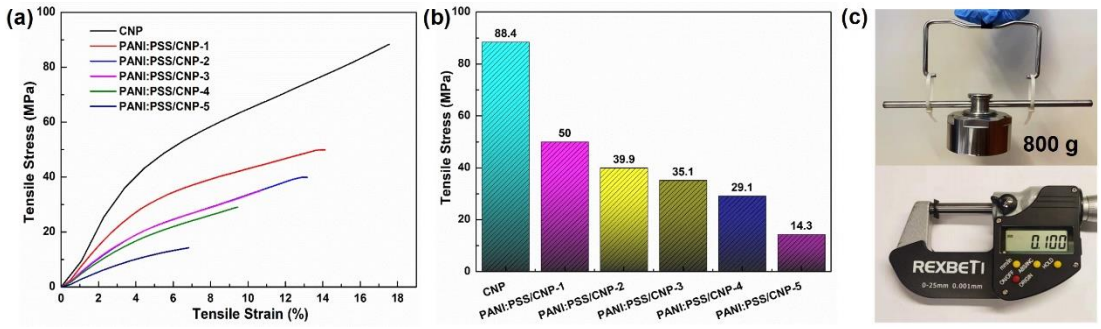

Figure 5.6 (a) Stress vs strain plot and (b) Tensile strength for CNP and PANI: PSS/CNP with different PANI: PSS mass loading; (c) Photograph of the PANI: PSS/CNP-4 strip, which could lift up a static load of 800 g

5.3.3 Conductivity

Theoretically, the electrode with high mass loading of electrically conductive material is favorable for improving the supercapacitor performance. As anticipated, when the mass ratio of PANI: PSS to PANI: PSS/CNP increases from 7.7% to 62.2%, the conductivity of PANI: PSS/CNP electrode increases from 0.008 S/cm to 1.16 S/cm (**Figure 5.7a**). It certifies that the electrical conductivity of PANI: PSS/CNP is mainly correlated to the content of PANI: PSS. Moreover, the measured values are superior to those of the reported cellulose conductive nanopapers [226, 233, 282]. It is worth noting that we can further improve the electrode conductivity via increasing the content of PANI: PSS, nevertheless, the mechanical performance of the composite electrode will be sacrificed. In order to prepare an electrode with high conductivity and good mechanical properties, the PANI: PSS/CNP-4 was chosen as an optimal electrode candidate and used for the electrochemical test later. Additionally, their conductance stability and flexibility were demonstrated by maintaining the luminance

of a blue LED bulb, where PANI: PSS/CNP-4 as a wire was subjected to different bending angles (**Figure 5.7b**).

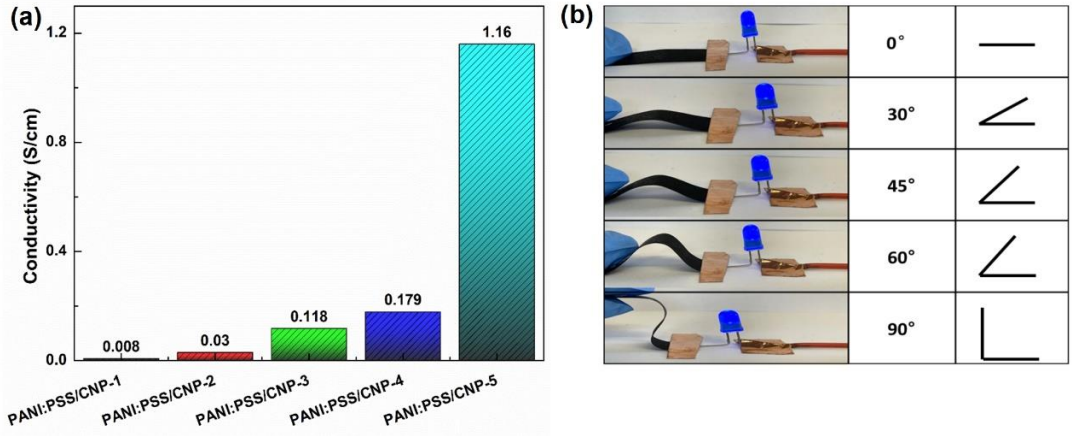

Figure 5.7 (a) Conductivity and (b) Photographs of PANI: PSS/CNP-4 with different bending angles

5.3.4 Electrochemical characterization

Figure 5.8a depicts the detailed CV profiles of PANI: PSS/CNP-4 between 0 V and 0.8 V at various scan rates. The shape of curves exhibits a quasi-rectangle under lower scan rates, which is induced by the pseudocapacitive behavior of the materials. As the scan rate increases, the curve deviates from the original shape, which is attributed to the fact that electrolyte ions with finite diffusion rates cannot diffuse from the solid/liquid interface to the electrode material and complete the electrochemical reaction under a high scan rate [283]. GCD behaviors of PANI: PSS/CNP-4 was measured at different current density. **Figure 5.8b** shows the nearly triangular GCD curves of PANI: PSS/CNP-4 with a very small voltage drop indicating superior capacitive performance. As the current density increases, the shape of curves is almost maintained indicating a highly reversible charge/discharge

property [245]. According to **Equation (5.3)**, the specific capacitance of the electrode derived from the GCD curves is calculated and shown in **Figure 5.8c and 5.8d**. The maximum specific capacitance value as high as 2.56 F/cm^2 (256 F/cm^3, 233 F/g) at 2 mA/cm^2 can be obtained, which is higher than other PANI-based electrode materials (**Table 5.2**). Moreover, with the increasing current density, the capacitance value decreases obviously, which is due to that the protons don't have enough time to reach the surface of the electrode, which decreases the accessibility of ions and active sites resulting in low utilization of active materials. EIS was employed to analyze the ion transport behavior of PANI: PSS/CNP-4. As shown in **Figure 5.8e**, the Nyquist plot consists of a small semicircle in the high-frequency region presenting the charge transfer resistance and a straight line in the low-frequency region, suggesting the ideal capacitance characteristics. The cycling stability of PANI: PSS/CNP-4 was verified by GCD measurements and shown in **Figure 5.8f**. After 8000 cycles, the specific capacitance of PANI: PSS/CNP-4 is still able to retain 81.5%. The remarkable cycling stability is ascribed to the introduction of good mechanical strength cellulose, which can more effectively prevent the volume expansion/shrinkage for PANI during the charging/discharging processes. In addition, the flexibility of the electrode was evaluated by the CV and GCD tests at different bending angles (0 º, 90 º, and 180 º) (**Figure 5.9a-c**). The result indicated that while the capacitance decreased with the increase of the bending angle (87% capacitance retention, at 180 º), but the overall stable performance demonstrated the electrode had excellent electrochemical behavior in the bending state (**Figure 5.9d**).

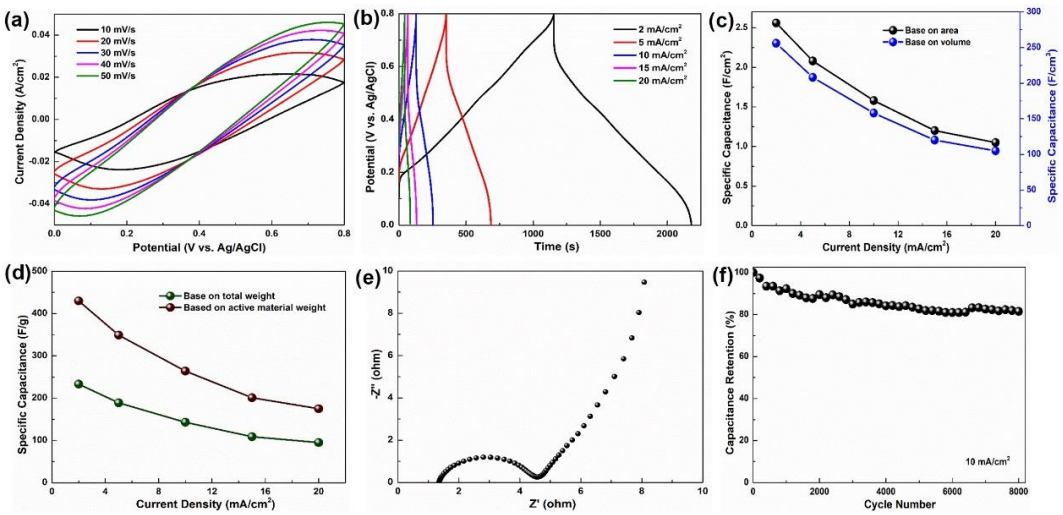

Figure 5.8 The electrochemical performance of PANI: PSS/CNP-4 in 1 M H_2SO_4 electrolyte. (a) CV curves; (b) GCD curves; (c) Specific capacitance based on areal and volume as a function of current density; (d) Specific capacitance based on total weight and active material weight as a function of current density; (e) Nyquist plot; (f) Cycling stability at 10 mA/cm^2

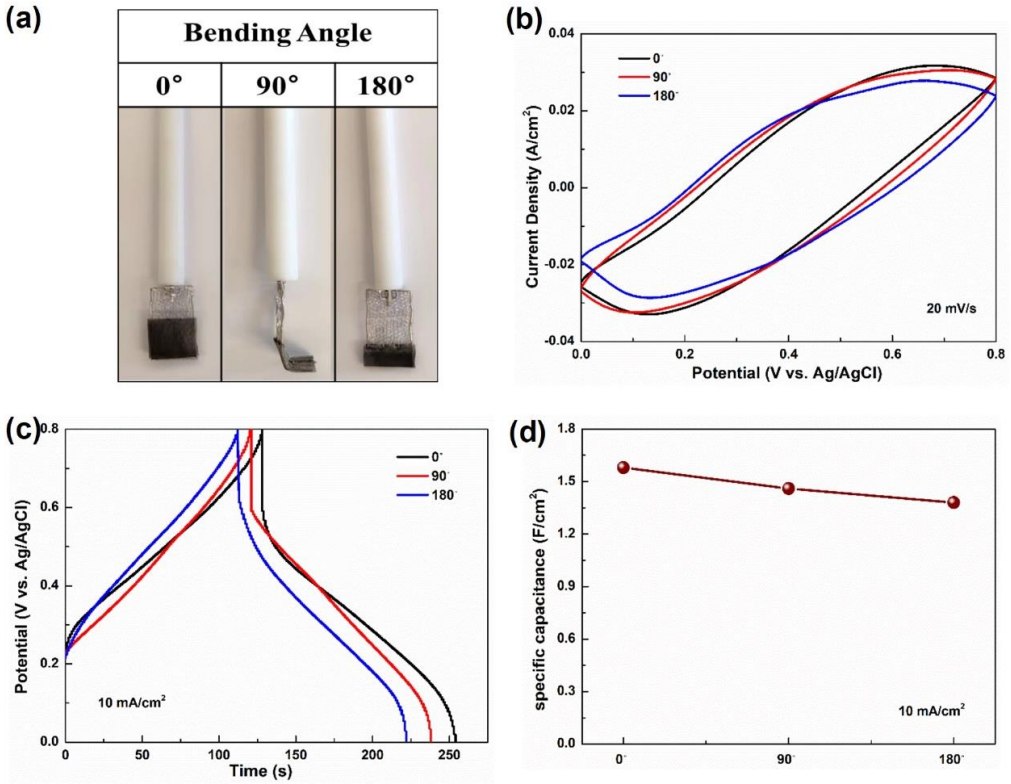

Figure 5.9 (a) Digital photos of PANI: PSS/CNP-4 at different bending angles (0 º, 90 º, and 180 º), (b) CV curves, (c) GCD curves, and (d) Specific capacitance of PANI: PSS/CNP-4 at different bending angles under 10 mA/cm^2

Table 5.2 Comparison of PANI: PSS/CNP electrode with other PANI-based electrode materials

Electrode materials	Specific capacitance	Capacitance retention (Cycles)	Ref
CNF/CNT/PANI	315 F/g, at 1 A/g	10000, 92.0%	[238]
CNFs/MWCNTs/PANI	207.2 F/g, at 0.2 A/g	1000, 82.4%	[284]
MnS/GO/PANI	773 F/g, at 1 A/g	1000, 95.6%	[285]
graphene/PANI fiber	871.4 mF/cm^2, at 0.5 mA/cm^2	5000, 85.5%	[286]
GO/PANI/$CuCo_2O_4$	312.7 F/g, at 1 A/g	5000, 84.2%	[287]
SWCNT/cellulose/PANI	330 mF/cm^2, at 0.2 mA/cm^2	1000, 79.0%	[288]
NiO/PANI:PSS	834 F/g, at 1 A/g	3000, 88.9%	[289]
PANI:PSS/Fe-modified graphene	768.6 F/g, at 1A/g	1600, 84.0%	[259]
MWCNTs/PANI/PSS-GR	602.5 F/g, at 0.5 A/g	2000, 78.32%	[260]
PANI:PSS/CNP	2.56 F/cm^2 (256 F/cm^3, 233 F/g) at 2 mA/cm^2	8000, 81.5%	**This work**

To better understand the underlying mechanism for the improved performance of the PANI: PSS/CNP electrode, a symmetric supercapacitor was fabricated with two pieces of PANI: PSS/CNP-4 (1 cm × 1 cm × 0.10 mm, 11 mg). The electrochemical performance of the device was evaluated in the two-electrode system. **Figure 5.10a** exhibits the CV curves of the device at different scan rates. As the scan rates increases,

the CV curves of the device show no obvious change, suggesting excellent rate feature and good reversibility. The GCD curves demonstrating near triangle shape indicate the ideal capacitive property. As the current density increases, the GCD curves maintain their original shape, matching the CV results (**Figure 5.10b**). The specific capacitance based on area, volume, and weight was calculated from the GCD curves and is presented in **Figure 5.10c and 5.10d.** The maximum areal capacitance of 460 mF/cm^2 (46 F/cm^3, 20.8 F/g) can be delivered by the device at 0.25 mA/cm^2. The cycling performance of the symmetric supercapacitor exhibits 78.3% capacitance retention after 2000 cycles at 2 mA/cm^2 **(Figure 5.10e).** To estimate the specific energy and power density of the device, the corresponding Ragone plot is exhibited in **Figure 5.11a and 11b**. The device offers the maximum energy density of 40.9 μWh/cm^2 (4.09 mWh/cm^3) with a power density of 100.5 μW/cm^2 (10.05 mW/cm^3), which outperforms most reported cellulose materials [225, 245-247, 250, 290-296]. This result suggests that PANI: PSS/CNP is a really hopeful candidate material for device applications of flexible wearable energy storage.

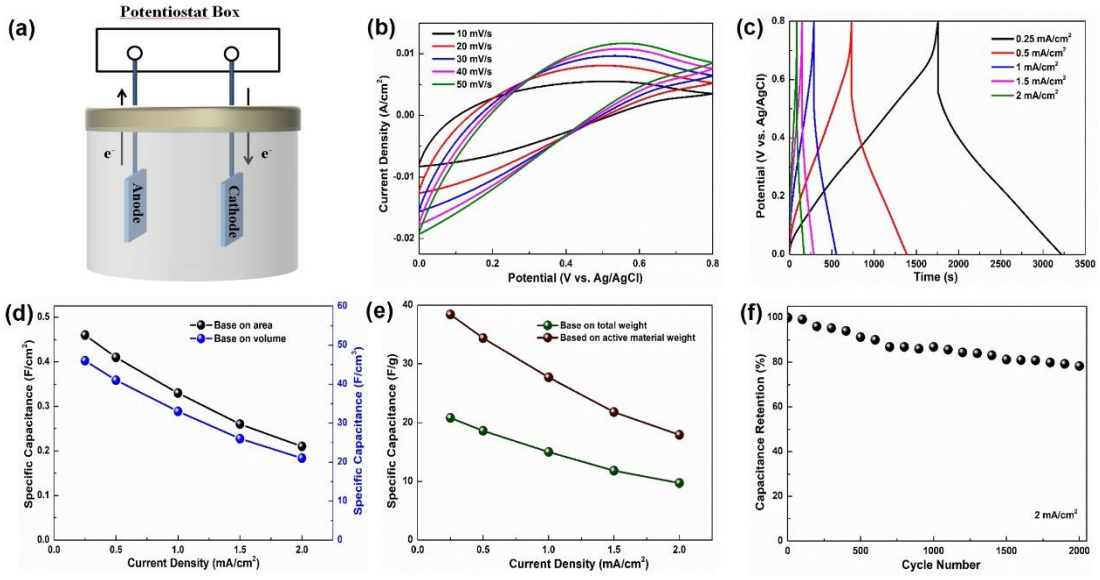

Figure 5.10 (a) Schematic illustration of the PANI: PSS/CNP supercapacitor device, (b) CV curves at different scan rate; (c) GCD curves at different current density; (d) Specific capacitance based on area and volume; (e) Specific capacitance based on total weight and active material weight; (f) Cycling stability of PANI: PSS/CNP device at 2 mA/cm^2

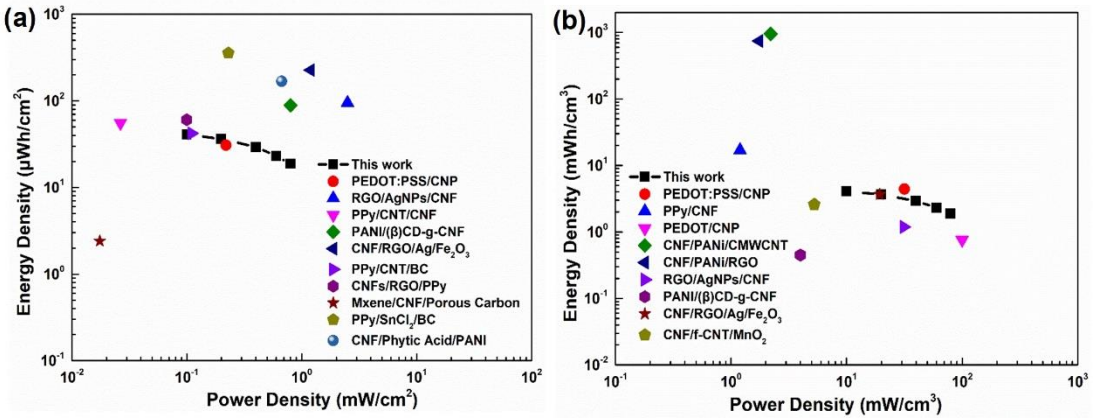

Figure 5.11 Ragone plots the symmetrical PANI: PSS/CNP supercapacitor device based on (a) area and (b) volume in comparison with other cellulose materials

5.4 Conclusion

In summary, a new freestanding, binder-free flexible PANI: PSS/CNF nanopaper electrode has been successfully fabricated by combining *in situ* polymerization with a simple and fast vacuum filtration method. Due to the effective combination of the cellulose as the flexible substrate and PANI: PSS as the active material, the PANI: PSS/CNP electrode exhibited high mechanical strength, and good conductance stability and superior flexibility. Besides, the PANI: PSS/CNP electrode yielded high specific capacitance of 2.56 F/cm^2 (256 F/cm^3, 233 F/g) and good cycling stability (81.5% capacitance retention, 8,000 cycles). Furthermore, the PANI: PSS/CNP-based symmetric supercapacitor showed a high areal energy density of 40.9 μWh/cm^2 at a power density of 100.5 μW/cm^2. It is worth noting that PANI: PSS/CNP may function well as a flexible supercapacitor electrode material because 1) PSS served as a dopant forming a water-soluble copolymer (PANI: PSS) with PANI effectively improves the processability problems of PANI, as well as a surfactant to improve the dispersity of PANI; 2) PANI with high conductivity provides good electrochemical properties (high specific capacitance, long cycling life, high power density, and energy density) to the electrode; 3) Cellulose is chosen as the flexible substrate, which provides good flexibility and mechanical strength for the electrodes due to the abundance of hydrogen bonds among cellulose molecules. Compared to conventional “rigid” electronic devices, our work provides new insight into the development of low-cost and energy-efficient flexible electrodes for the future design of green electronics.

Chapter 6: Conclusion and future work

Due to the increased energy consumption along with various environmental pollutions, there has been a crucial demand for the development of materials as well as their devices. Supercapacitors, as an important energy storage device, have been widely recognized as promising candidates due to their high power density, long cycling life, robust mechanical flexibility, and good operational safety. As the most important part of supercapacitors, the electrode is considered as a key impact on the successful fabrication of high performance supercapacitors. From this perspective, this dissertation is devoted to finding low-cost, sustainable electrode materials with high electrochemical performance. The obtained results from the projects indicated that the fabrication of the functional nanocomposite could effectively overcome the disadvantages of the single component electrode material to advance the performance of the SC. Furthermore, the attractiveness of these materials depends not only on the intrinsic properties of the building components but also on the methods of intelligent construction, hybridization, and synergy of these nanomaterials. In this regard, several highly facile and efficient preparation methods (microwave heating, in situ polymerization, and vacuum filtration) were used to synthesize nanocomposites in a highly controllable manner with improved electrochemical properties of the final product. Based on the presented results, our future work can transfer to three diverse directions to further improve the performance of the electrode: 1) synthesizing a variety of nanostructures electrode materials such as nanosize structure, porous structure, and architectures with different dimensions; 2) synthesizing electrode

materials of binary metal oxides and conducting polymer/graphene; 3) fabrication of asymmetric supercapacitors.

1) Synthesize a variety of nanostructure electrode materials

According to the charge storage mechanism of supercapacitors, the electrochemical performance of electrode materials is related to the ion accessible surface area and the kinetics of electron transfer.[297] Therefore, the surface area, mass loading, efficient utilization and path length for the electrolyte ion diffusion can be modified to adjust electrode performance. Constructing various morphologies of the electrode materials is a common used strategy to improve the electrochemical performance of the electrode materials. For instance, Dubal *et al.* reported the synthesis of PPy with different morphologies by electrochemical polymerization. The specific capacitance increased and charge transfer resistances values decreased when the nanostructure changes from nanobelts to nanosheets.[298] Except for the morphology, reasonable utilization of the porous structure is extremely important for electrode performance. This is due to 1) macropores minimize the diffusion resistance that facilitates the penetration of electrolyte ions to the interior surface of the electrode, improving the rate capability and cycle stability of the electrodes; 2) mesopores provide a large accessible surface area for ion transport/charge storage; 3) micropores contribute to increasing the specific surface area (SSA) and specific capacitance.[299] Furthermore, Jung, Sung *et al.* tuned the pore structure of porous graphene aerogels by controlling the electrolyte content in the exfoliation process. The aspect ratio of the graphene sheets and the porosity of the graphene network were

effectively optimized.[300] The above results indicate that we can develop a variety of nanostructures by adjusting the reaction conditions.

2) Synthesize electrode materials of binary metal oxides and conducting polymer/graphene

The design of binary metal oxide nanostructured electrodes is advantageous because the creation of active sites and defects in the grain boundaries of heterostructured materials leads to multiple redox activities, excellent electrical conductivity, and short diffusion paths. For example, Wang *et al*. synthesized different morphologies of $NiCo_2O_4$ by controlling the pH value during hydrothermal.[301] $NiCo_2O_4$ provided two different active sites for double redox reactions to enhance the charge storage capacity of the electrode. The low solution resistance at the electrode-electrolyte interface decreased due to the increase of the electrical conductivity induced by the defect that benefits the free charge carriers. The result indicated that binary metal oxide composites can exert the synergistic effect of pure oxides, which can improve capacitive performance with rapid ionic transport, superior conductivity, more active sites, and improved stability. Recently, binary metal oxide has been introduced to hybridize with carbonaceous materials (graphene, carbon nanotube, and activated carbon) and conducting polymers to improve the performance of electrode materials. Xu *et al.* studied the electrochemical performance of PANI/$NiCo_2O_4$ using CV, GCD, and EIS tests.[302] The presence of multimetal oxides provides additional active sites as well as a larger surface area, making the electrolyte more accessible to the active sites. The rough surface of the electrode

facilitates charge transfer between the electrode material and the electrolyte. Binary transition metal oxide/reduced graphene oxide nanocomposites (SnO_2-Co_3O_4/rGO) has been prepared using the co-precipitation method in 2020.[303] The conductivity, chemical stability and mechanical support of the material increased when compared to bare nanoparticles and the SnO_2-Co_3O_4 nanocomposite due to the combined contribution of both electric double layer capacitance and pseudocapacitance behavior. The above results proved that hybridization of binary metal oxide and conducting polymer/graphene can provide high electrochemical performance for electrodes.

3) Fabrication of asymmetric supercapacitors

Asymmetric supercapacitors device constructed with battery-type/pseudocapacitive material as the positive electrode and carbon-based material as the negative electrode. Benefiting from their structure, asymmetric supercapacitors could provide battery-like energy with supercapacitor-like power. Compared to the symmetric supercapacitors devices in our project, asymmetric supercapacitors are more suitable for commercial applications. For example, asymmetric supercapacitors have been fabricated using PPy@MoO_3 positive electrode and AC as negative electrode with an energy density of 12 Wh/kg at 3 kW/kg.[304] Kim M and coworker designed a high-voltage asymmetric electrochemical supercapacitor (1.9 V) using AC as the negative electrode and a silicon carbide-MnO_2 nanoneedle (SiC-N-MnO_2) composite as the positive electrode. Due to the synergistic effects of AC and SiC-N-MnO_2, the asymmetric supercapacitor exhibited a specific capacitance of 59.9 F/g and an excellent energy density (30.06

Wh/ kg at 113.92 W/kg).[305]

Although encouraging results have been attained in this research, there are still many challenges to commercialize these nanocomposites for energy materials in the future. Our work provides experimental and theoretical analysis to the nanocomposite systems, and hopefully it could support the design of high electrochemical performance functional nanocomposites, and the application in the next-generation energy storage devices.

Reference

[1] A.G. Pandolfo, A.F. Hollenkamp, Carbon properties and their role in supercapacitors, Journal of power sources, 157 (2006) 11.

[2] B.K. Roy, I. Tahmid, T.U. Rashid, Chitosan-Based Materials for Supercapacitor Application-A Review, Journal of Materials Chemistry A, (2021).

[3] H. Helmholtz, Studien über electrische Grenzschichten, Annalen der Physik, 243 (1879) 337-382.

[4] H.I. Becker, Low voltage electrolytic capacitor, Google Patents, 1957.

[5] L. Yang, X. Lu, S. Wang, J. Wang, X. Guan, X. Guan, G. Wang, Designed synthesis of nickel-cobalt-based electrode materials for high-performance solid-state hybrid supercapacitors, Nanoscale, 12 (2020) 1921-1938.

[6] B. Huang, W. Wang, T. Pu, J. Li, C. Zhao, L. Xie, L. Chen, Rational design and facile synthesis of two-dimensional hierarchical porous $M_3V_2O_8$ (M=Co, Ni and Co-Ni) thin sheets assembled by ultrathin nanosheets as positive electrode materials for high-performance hybrid supercapacitors, Chemical Engineering Journal, 375 (2019) 121969.

[7] Y.-R. Zhu, P.-P. Peng, J.-Z. Wu, T.-F. Yi, Y. Xie, S. Luo, Co_3O_4@$NiCo_2O_4$ microsphere as electrode materials for high-performance supercapacitors, Solid State Ionics, 336 (2019) 110.

[8] F. Nti, D.A. Anang, J.I. Han, Facilely synthesized $NiMoO_4$/$CoMoO_4$ nanorods as electrode material for high performance supercapacitor, Journal of Alloys and Compounds, 742 (2018) 342.

[9] J. Acharya, T.H. Ko, M.-K. Seo, M.-S. Khil, H.-Y. Kim, B.-S. Kim, Oxalic acid assisted rapid synthesis of mesoporous $NiCo_2O_4$ nanorods as electrode materials with higher energy density and cycle stability for high-performance asymmetric hybrid supercapacitor applications, Journal of colloid and interface science, 564 (2020) 65.

[10] P. Forouzandeh, V. Kumaravel, S.C. Pillai, Electrode materials for supercapacitors: a review of recent advances, Catalysts, 10 (2020) 969.

[11] Z.S. Iro, C. Subramani, S.S. Dash, A brief review on electrode materials for supercapacitor, Int. J. Electrochem. Sci, 11 (2016) 10628-10643.

[12] M. Winter, R.J. Brodd, What are batteries, fuel cells, and supercapacitors?, Chemical reviews, 104 (2004) 4245-4270.

[13] H. Du, X. Lin, Z. Xu, D. Chu, Electric double-layer transistors: a review of recent progress, Journal of Materials Science, 50 (2015) 5641-5673.

[14] T.S. Mathis, N. Kurra, X. Wang, D. Pinto, P. Simon, Y. Gogotsi, Energy storage data reporting in perspective-guidelines for interpreting the performance of electrochemical energy storage systems, Advanced Energy Materials, 9 (2019) 1902007.

[15] E.I. Santiago, A.V.C. Andrade, C.O. Paiva-Santos, L.O.S. Bulhoes, Structural and electrochemical properties of $LiCoO_2$ prepared by combustion synthesis, Solid State Ionics, 158 (2003) 91-102.

[16] V. Augustyn, P. Simon, B. Dunn, Pseudocapacitive oxide materials for high-rate electrochemical energy storage, Energy & Environmental Science, 7 (2014)

1597-1614.

[17] M. Okubo, E. Hosono, J. Kim, M. Enomoto, N. Kojima, T. Kudo, H. Zhou, I. Honma, Nanosize effect on high-rate Li-ion intercalation in $LiCoO_2$ electrode, Journal of the American chemical society, 129 (2007) 7444.

[18] J. Wang, J. Polleux, J. Lim, B. Dunn, Pseudocapacitive contributions to electrochemical energy storage in TiO_2 (anatase) nanoparticles, The Journal of Physical Chemistry C, 111 (2007) 14925.

[19] H. Huang, M. Niederberger, Towards fast-charging technologies in Li^+/Na^+ storage: from the perspectives of pseudocapacitive materials and non-aqueous hybrid capacitors, Nanoscale, 11 (2019) 19225-19240.

[20] E. Herrero, L.J. Buller, H.D. Abruña, Underpotential deposition at single crystal surfaces of Au, Pt, Ag and other materials, Chemical Reviews, 101 (2001) 1897-1930.

[21] C.-C. Hu, K.-H. Chang, M.-C. Lin, Y.-T. Wu, Design and tailoring of the nanotubular arrayed architecture of hydrous RuO_2 for next generation supercapacitors, Nano letters, 6 (2006) 2690-2695.

[22] V. Augustyn, J. Come, M. a. Lowe, JW Kim, P.-L. Taberna, SH Tolbert, HD Abruña, P. Simon and B. Dunn, Nat. Mater, 12 (2013) 518-522.

[23] Y. Wang, Y. Song, Y. Xia, Electrochemical capacitors: mechanism, materials, systems, characterization and applications, Chemical Society Reviews, 45 (2016) 5925-5950.

[24] V. Augustyn, J. Come, M.A. Lowe, J.W. Kim, P.-L. Taberna, S.H. Tolbert, H.D.

Abruña, P. Simon, B. Dunn, High-rate electrochemical energy storage through Li^+ intercalation pseudocapacitance, Nature materials, 12 (2013) 518.

[25] C. Yang, J. Feng, F. Lv, J. Zhou, C. Lin, K. Wang, Y. Zhang, Y. Yang, W. Wang, J. Li, Metallic graphene-like VSe^2 ultrathin nanosheets: superior potassium-ion storage and their working mechanism, Advanced Materials, 30 (2018) 1800036.

[26] B. Hsia, Materials synthesis and characterization for micro-supercapacitor applications, University of California, Berkeley2013.

[27] F. Rafik, H. Gualous, R. Gallay, A. Crausaz, A. Berthon, Frequency, thermal and voltage supercapacitor characterization and modeling, Journal of power sources, 165 (2007) 928-934.

[28] B.-A. Mei, J. Lau, T. Lin, S.H. Tolbert, B.S. Dunn, L. Pilon, Physical interpretations of electrochemical impedance spectroscopy of redox active electrodes for electrical energy storage, The Journal of Physical Chemistry C, 122 (2018) 24499-24511.

[29] M. Lenz, J. Zabel, M. Franzreb, New approach for investigating diffusion kinetics within capacitive deionization electrodes using electrochemical impedance spectroscopy, Frontiers in Materials, 7 (2020) 229.

[30] T. Qian, N. Xu, J. Zhou, T. Yang, X. Liu, X. Shen, J. Liang, C. Yan, Interconnected three-dimensional V_2O_5/polypyrrole network nanostructures for high performance solid-state supercapacitors, Journal of Materials Chemistry A, 3 (2015) 488-493.

[31] A.M. Abdelkader, A.J. Cooper, R.A.W. Dryfe, I.A. Kinloch, How to get between

the sheets: a review of recent works on the electrochemical exfoliation of graphene materials from bulk graphite, Nanoscale, 7 (2015) 6944-6956.

[32] A. Ambrosi, M. Pumera, Exfoliation of layered materials using electrochemistry, Chemical Society Reviews, 47 (2018) 7213-7224.

[33] R. Kumar, S. Sahoo, E. Joanni, R.K. Singh, W.K. Tan, K.K. Kar, A. Matsuda, Recent progress in the synthesis of graphene and derived materials for next generation electrodes of high performance lithium ion batteries, Progress in Energy and Combustion Science, 75 (2019) 100786.

[34] G. Cai, P. Darmawan, M. Cui, J. Wang, J. Chen, S. Magdassi, P.S. Lee, Highly stable transparent conductive silver grid/PEDOT:PSS electrodes for integrated bifunctional flexible electrochromic supercapacitors, Advanced Energy Materials, 6 (2016) 1501882.

[35] D. Yang, Y. Song, Y.-J. Ye, M. Zhang, X. Sun, X.-X. Liu, Boosting the pseudocapacitance of nitrogen-rich carbon nanorod arrays for electrochemical capacitors, Journal of Materials Chemistry A, 7 (2019) 12086-12094.

[36] Y. Huang, J. Tao, W. Meng, M. Zhu, Y. Huang, Y. Fu, Y. Gao, C. Zhi, Super-high rate stretchable polypyrrole-based supercapacitors with excellent cycling stability, Nano Energy, 11 (2015) 518-525.

[37] K. Okamura, R. Inoue, T. Sebille, K. Tomono, M. Nakayama, An approach to optimize the composition of supercapacitor electrodes consisting of manganese-molybdenum mixed oxide and carbon nanotubes, Journal of The Electrochemical Society, 158 (2011) A711.

[38] Y.-H. Li, Q.-Y. Li, H.-Q. Wang, Y.-G. Huang, X.-H. Zhang, Q. Wu, H.-Q. Gao, J.-H. Yang, Synthesis and electrochemical properties of nickel-manganese oxide on MWCNTs/CFP substrate as a supercapacitor electrode, Applied Energy, 153 (2015) 78-86.

[39] H. Zhou, X. Zou, K. Zhang, P. Sun, M.S. Islam, J. Gong, Y. Zhang, J. Yang, Molybdenum-tungsten mixed oxide deposited into titanium dioxide nanotube arrays for ultrahigh rate supercapacitors, ACS Applied Materials & Interfaces, 9 (2017) 18699-18709.

[40] Y. Wang, S. Dong, X. Wu, M. Li, One-step electrodeposition of MnO_2@NiAl layered double hydroxide nanostructures on the nickel foam for high-performance supercapacitors, Journal of The Electrochemical Society, 164 (2016) H56.

[41] Z. Zeng, P. Sun, J. Zhu, X. Zhu, Porous petal-like $Ni(OH)_2$- MnO_x nanosheet electrodes grown on carbon fiber paper for supercapacitors, Surfaces and Interfaces, 8 (2017) 73-82.

[42] T. Sreethawong, S. Chavadej, S. Ngamsinlapasathian, S. Yoshikawa, A modified sol-gel process-derived highly nanocrystalline mesoporous NiO with narrow pore size distribution, Colloids and Surfaces A: Physicochemical and Engineering Aspects, 296 (2007) 222-229.

[43] T. Puangpetch, S. Chavadej, T. Sreethawong, Mesoporous-assembled V_2O_5 nanosheet synthesized via a surfactant-modified sol-gel technique and its photocatalytic H_2 production activity under visible light irradiation, Powder

technology, 208 (2011) 37-41.

[44] T. Sreethawong, S. Chavadej, S. Ngamsinlapasathian, S. Yoshikawa, Sol-gel synthesis of mesoporous assembly of Nd_2O_3 nanocrystals with the aid of structure-directing surfactant, Solid state sciences, 10 (2008) 20-25.

[45] A.A. Mirghni, M.J. Madito, K.O. Oyedotun, T.M. Masikhwa, N.M. Ndiaye, S.J. Ray, N. Manyala, A high energy density asymmetric supercapacitor utilizing a nickel phosphate/graphene foam composite as the cathode and carbonized iron cations adsorbed onto polyaniline as the anode, RSC advances, 8 (2018) 11608-11621.

[46] S. Venkateshalu, D. Rangappa, A.N. Grace, Hydrothermal synthesis and electrochemical properties of CoS_2-reduced graphene oxide nanocomposite for supercapacitor application, International Journal of Nanoscience, 17 (2018) 1760020.

[47] K. Sharma, N. Singh, S.K. Tripathi, Characterization of nickel cobalt oxide: a potential material for supercapacitor, Materials Research Express, 6 (2018) 025502.

[48] H. Xiao, F. Qu, X. Wu, Ultrathin NiO nanoflakes electrode materials for supercapacitors, Applied Surface Science, 360 (2016) 8-13.

[49] J. Zhu, J. Jiang, J. Liu, R. Ding, H. Ding, Y. Feng, G. Wei, X. Huang, Direct synthesis of porous NiO nanowall arrays on conductive substrates for supercapacitor application, Journal of Solid State Chemistry, 184 (2011) 578-583.

[50] J. Sun, W. Wang, Q. Yue, Review on microwave-matter interaction fundamentals and efficient microwave-associated heating strategies, Materials, 9 (2016) 231.

[51] H.I. Lee, J.H. Kim, S.H. Joo, H. Chang, D. Seung, O.-S. Joo, D.J. Suh, W.-S. Ahn, C. Pak, J.M. Kim, Ultrafast production of ordered mesoporous carbons via microwave irradiation, Letters to the Editor, 45 (2007) 2843-2854.

[52] J.-F. Zhu, Y.-J. Zhu, Microwave-assisted one-step synthesis of polyacrylamide-metal (M=Ag, Pt, Cu) nanocomposites in ethylene glycol, The Journal of Physical Chemistry B, 110 (2006) 8593-8597.

[53] Y. Wang, Z. Iqbal, S. Mitra, Rapid, low temperature microwave synthesis of novel carbon nanotube-silicon carbide composite, Carbon, 44 (2006) 2804-2808.

[54] Y. Zhang, L. Li, H. Su, W. Huang, X. Dong, Binary metal oxide: advanced energy storage materials in supercapacitors, Journal of Materials Chemistry A, 3 (2015) 43-59.

[55] R.S. Kate, S.A. Khalate, R.J. Deokate, Overview of nanostructured metal oxides and pure nickel oxide (NiO) electrodes for supercapacitors: a review, Journal of Alloys and Compounds, 734 (2018) 89-111.

[56] M. Zhi, C. Xiang, J. Li, M. Li, N. Wu, Nanostructured carbon-metal oxide composite electrodes for supercapacitors: a review, Nanoscale, 5 (2013) 72-88.

[57] M. Nakamura, M. Nakanishi, K. Yamamoto, Influence of physical properties of activated carbons on characteristics of electric double-layer capacitors, Journal of power sources, 60 (1996) 225-231.

[58] V.C. Lokhande, A.C. Lokhande, C.D. Lokhande, J.H. Kim, T. Ji, Supercapacitive composite metal oxide electrodes formed with carbon, metal oxides and conducting polymers, Journal of Alloys and Compounds, 682 (2016) 381-403.

[59] M. Galiński, A. Lewandowski, I. Stępniak, Ionic liquids as electrolytes, Electrochimica acta, 51 (2006) 5567-5580.

[60] A. Jain, S. Jayaraman, M. Ulaganathan, R. Balasubramanian, V. Aravindan, M.P. Srinivasan, S. Madhavi, Highly mesoporous carbon from Teak wood sawdust as prospective electrode for the construction of high energy Li-ion capacitors, Electrochimica Acta, 228 (2017) 131-138.

[61] X. Fang, D. Yao, An overview of solid-like electrolytes for supercapacitors, American Society of Mechanical Engineers, 2013, pp. V06AT07A071.

[62] E. Coadou, L. Timperman, J. Jacquemin, H. Galiano, C. Hardacre, M. Anouti, Comparative study on performances of trimethyl-sulfonium and trimethyl-ammonium based ionic liquids in molecular solvents as electrolyte for electrochemical double layer capacitors, The Journal of Physical Chemistry C, 117 (2013) 10315-10325.

[63] N. Padmanathan, S. Selladurai, K.M. Rahulan, C. O'Dwyer, K.M. Razeeb, NiO hybrid nanoarchitecture-based pseudocapacitor in organic electrolyte with high rate capability and cycle life, Ionics, 21 (2015) 2623-2631.

[64] A. Brandt, S. Pohlmann, A. Varzi, A. Balducci, S. Passerini, Ionic liquids in supercapacitors, MRS bulletin, 38 (2013) 554-559.

[65] J. Garche, C. Dyer, P.T. Moseley, Z. Ogumi, D.A.J. Rand, B. Scrosati,

Encyclopedia of electrochemical power sources, Newnes2013.

[66] Y. Huang, J. Liang, Y. Chen, An overview of the applications of graphene-based materials in supercapacitors, small, 8 (2012) 1805-1834.

[67] S.-M. Chen, R. Ramachandran, V. Mani, R. Saraswathi, Recent advancements in electrode materials for the high-performance electrochemical supercapacitors: a review, Int. J. Electrochem. Sci, 9 (2014) 4072-4085.

[68] Y. Zhai, Y. Dou, D. Zhao, P.F. Fulvio, R.T. Mayes, S. Dai, Carbon materials for chemical capacitive energy storage, Advanced materials, 23 (2011) 4828-4850.

[69] M. Vangari, T. Pryor, L. Jiang, Supercapacitors: review of materials and fabrication methods, Journal of Energy Engineering, 139 (2013) 72-79.

[70] Y. Wang, L. Zhang, H. Hou, W. Xu, G. Duan, S. He, K. Liu, S. Jiang, Recent progress in carbon-based materials for supercapacitor electrodes: a review, Journal of Materials Science, 56 (2021) 173-200.

[71] S. Bose, T. Kuila, A.K. Mishra, R. Rajasekar, N.H. Kim, J.H. Lee, Carbon-based nanostructured materials and their composites as supercapacitor electrodes, Journal of Materials Chemistry, 22 (2012) 767-784.

[72] L.L. Zhang, X.S. Zhao, Carbon-based materials as supercapacitor electrodes, Chemical Society Reviews, 38 (2009) 2520-2531.

[73] E. Frackowiak, Carbon materials for supercapacitor application, Physical chemistry chemical physics, 9 (2007) 1774-1785.

[74] A.B. Fuertes, G. Lota, T.A. Centeno, E. Frackowiak, Templated mesoporous carbons for supercapacitor application, Electrochimica Acta, 50 (2005)

2799-2805.

[75] G. Lota, T.A. Centeno, E. Frackowiak, F. Stoeckli, Improvement of the structural and chemical properties of a commercial activated carbon for its application in electrochemical capacitors, Electrochimica Acta, 53 (2008) 2210-2216.

[76] V. Subramanian, C. Luo, A.M. Stephan, K.S. Nahm, S. Thomas, B. Wei, Supercapacitors from activated carbon derived from banana fibers, The Journal of Physical Chemistry C, 111 (2007) 7527-7531.

[77] S. Ghosh, Hydrogen Storage in Single-Walled Carbon Nanotubes, IIT, Kharagpur, 2017.

[78] H. Pan, J. Li, Y. Feng, Carbon nanotubes for supercapacitor, Nanoscale research letters, 5 (2010) 654-668.

[79] X. Liu, J. Zeng, H. Yang, K. Zhou, D. Pan, V_2O_5-based nanomaterials: synthesis and their applications, RSC advances, 8 (2018) 4014-4031.

[80] Z. Yang, J. Tian, Z. Yin, C. Cui, W. Qian, F. Wei, Carbon nanotube-and graphene-based nanomaterials and applications in high-voltage supercapacitor: A review, Carbon, 141 (2019) 467-480.

[81] Q. Wang, Y. Ma, X. Liang, D. Zhang, M. Miao, Flexible supercapacitors based on carbon nanotube-MnO_2 nanocomposite film electrode, Chemical Engineering Journal, 371 (2019) 145-153.

[82] R. Malik, L. Zhang, C. McConnell, M. Schott, Y.-Y. Hsieh, R. Noga, N.T. Alvarez, V. Shanov, Three-dimensional, free-standing polyaniline/carbon nanotube composite-based electrode for high-performance supercapacitors,

Carbon, 116 (2017) 579-590.

[83] B.K. Kim, S. Sy, A. Yu, J. Zhang, Electrochemical supercapacitors for energy storage and conversion, Handbook of clean energy systems, (2015) 1-25.

[84] R.B. Rakhi, W. Chen, D. Cha, H.N. Alshareef, High performance supercapacitors using metal oxide anchored graphene nanosheet electrodes, Journal of Materials Chemistry, 21 (2011) 16197-16204.

[85] W.K. Chee, H.N. Lim, I. Harrison, K.F. Chong, Z. Zainal, C.H. Ng, N.M. Huang, Performance of flexible and binderless polypyrrole/graphene oxide/zinc oxide supercapacitor electrode in a symmetrical two-electrode configuration, Electrochimica Acta, 157 (2015) 88-94.

[86] C.-q. Yi, J.-p. Zou, H.-z. Yang, L. Xian, Recent advances in pseudocapacitor electrode materials: transition metal oxides and nitrides, Transactions of Nonferrous Metals Society of China, 28 (2018) 1980-2001.

[87] S.C. Pang, M.A. Anderson, T.W. Chapman, Novel electrode materials for thin-film ultracapacitors: comparison of electrochemical properties of sol-gel-derived and electrodeposited manganese dioxide, Journal of the Electrochemical Society, 147 (2000) 444.

[88] M. Toupin, T. Brousse, D. Bélanger, Charge storage mechanism of MnO_2 electrode used in aqueous electrochemical capacitor, Chemistry of Materials, 16 (2004) 3184-3190.

[89] H.Y. Lee, J.B. Goodenough, Supercapacitor behavior with KCl electrolyte, Journal of Solid State Chemistry, 144 (1999) 220-223.

[90] J.-G. Wang, F. Kang, B. Wei, Engineering of MnO_2-based nanocomposites for high-performance supercapacitors, Progress in Materials Science, 74 (2015) 51-124.

[91] T. Brousse, M. Toupin, R. Dugas, L. Athouel, O. Crosnier, D. Belanger, Crystalline MnO_2 as possible alternatives to amorphous compounds in electrochemical supercapacitors, Journal of the Electrochemical Society, 153 (2006) A2171.

[92] V.B.R. Boppana, F. Jiao, Nanostructured MnO_2: an efficient and robust water oxidation catalyst, Chemical Communications, 47 (2011) 8973-8975.

[93] H. Chen, S. Zhou, L. Wu, Porous nickel hydroxide–manganese dioxide-reduced graphene oxide ternary hybrid spheres as excellent supercapacitor electrode materials, ACS applied materials & interfaces, 6 (2014) 8621-8630.

[94] S. Nandy, U.N. Maiti, C.K. Ghosh, K.K. Chattopadhyay, Enhanced p-type conductivity and band gap narrowing in heavily Al doped NiO thin films deposited by RF magnetron sputtering, Journal of Physics: Condensed Matter, 21 (2009) 115804.

[95] B.E. Conway, Electrochemical supercapacitors: scientific fundamentals and technological applications, Springer Science & Business Media2013.

[96] N. Liu, J. Li, W. Ma, W. Liu, Y. Shi, J. Tao, X. Zhang, J. Su, L. Li, Y. Gao, Ultrathin and lightweight 3D free-standing Ni@NiO nanowire membrane electrode for a supercapacitor with excellent capacitance retention at high rates, ACS applied materials & interfaces, 6 (2014) 13627-13634.

[97] M.S. Kolathodi, M. Palei, T.S. Natarajan, Electrospun NiO nanofibers as cathode materials for high performance asymmetric supercapacitors, Journal of Materials Chemistry A, 3 (2015) 7513-7522.

[98] D. Das, L.J. Borthakur, B.C. Nath, B.J. Saikia, K.J. Mohan, S.K. Dolui, Designing hierarchical NiO/PAni-MWCNT core-shell nanocomposites for high performance super capacitor electrodes, RSC advances, 6 (2016) 44878-44887.

[99] A. García-Gómez, S. Eugénio, R.G. Duarte, T.M. Silva, M.J. Carmezim, M.F. Montemor, Electrodeposited reduced-graphene oxide/cobalt oxide electrodes for charge storage applications, Applied Surface Science, 382 (2016) 34-40.

[100] S. Kalasina, N. Phattharasupakun, M. Sawangphruk, A new energy conversion and storage device of cobalt oxide nanosheets, Journal of Materials Chemistry A, 6 (2018) 36-40.

[101] Y. Gao, S. Chen, D. Cao, G. Wang, J. Yin, Electrochemical capacitance of Co_3O_4 nanowire arrays supported on nickel foam, Journal of Power Sources, 195 (2010) 1757-1760.

[102] G. Wang, X. Shen, J. Horvat, B. Wang, H. Liu, D. Wexler, J. Yao, Hydrothermal synthesis and optical, magnetic, and supercapacitance properties of nanoporous cobalt oxide nanorods, The Journal of Physical Chemistry C, 113 (2009) 4357-4361.

[103] S.H. Kim, Y.I. Kim, J.H. Park, J.M. Ko, Cobalt-manganese oxide/carbon-nanofiber composite electrodes for supercapacitors, Int. J. Electrochem. Sci, 4 (2009) 1489-1496.

[104] N.A. Chernova, M. Roppolo, A.C. Dillon, M.S. Whittingham, Layered vanadium and molybdenum oxides: batteries and electrochromics, Journal of Materials Chemistry, 19 (2009) 2526-2552.

[105] B. Saravanakumar, K.K. Purushothaman, G. Muralidharan, Interconnected V_2O_5 nanoporous network for high-performance supercapacitors, ACS applied materials & interfaces, 4 (2012) 4484-4490.

[106] D. Majumdar, M. Mandal, S.K. Bhattacharya, V_2O_5 and its carbon-based nanocomposites for supercapacitor applications, ChemElectroChem, 6 (2019) 1623-1648.

[107] S.D. Perera, B. Patel, N. Nijem, K. Roodenko, O. Seitz, J.P. Ferraris, Y.J. Chabal, K.J. Balkus Jr, Vanadium oxide nanowire–carbon nanotube binder-free flexible electrodes for supercapacitors, Advanced Energy Materials, 1 (2011) 936-945.

[108] Q. Meng, K. Cai, Y. Chen, L. Chen, Research progress on conducting polymer based supercapacitor electrode materials, Nano Energy, 36 (2017) 268-285.

[109] K.D. Fong, T. Wang, S.K. Smoukov, Multidimensional performance optimization of conducting polymer-based supercapacitor electrodes, Sustainable Energy & Fuels, 1 (2017) 1857-1874.

[110] W. Teng, Q. Zhou, X. Wang, H. Che, P. Hu, H. Li, J. Wang, Hierarchically interconnected conducting polymer hybrid fiber with high specific capacitance for flexible fiber-shaped supercapacitor, Chemical Engineering Journal, 390 (2020) 124569.

[111] T.O. Magu, A.U. Agobi, L. Hitler, P.M. Dass, A review on conducting polymers-based composites for energy storage application, Journal of Chemical Reviews, 1 (2019) 19-34.

[112] G.A. Snook, P. Kao, A.S. Best, Conducting-polymer-based supercapacitor devices and electrodes, Journal of power sources, 196 (2011) 1-12.

[113] A. Rudge, J. Davey, I. Raistrick, S. Gottesfeld, J.P. Ferraris, Conducting polymers as active materials in electrochemical capacitors, Journal of power sources, 47 (1994) 89-107.

[114] V. Gupta, N. Miura, Polyaniline/single-wall carbon nanotube (PANI/SWCNT) composites for high performance supercapacitors, Electrochimica acta, 52 (2006) 1721-1726.

[115] K.R. Prasad, N. Miura, Polyaniline-MnO_2 composite electrode for high energy density electrochemical capacitor, Electrochemical and Solid State Letters, 7 (2004) A425.

[116] C. Zhou, Y. Zhang, Y. Li, J. Liu, Construction of high-capacitance 3D CoO@ polypyrrole nanowire array electrode for aqueous asymmetric supercapacitor, Nano letters, 13 (2013) 2078-2085.

[117] K. Liu, Z. Hu, R. Xue, J. Zhang, J. Zhu, Electropolymerization of high stable poly (3, 4-ethylenedioxythiophene) in ionic liquids and its potential applications in electrochemical capacitor, Journal of Power Sources, 179 (2008) 858-862.

[118] N. Phattharasupakun, J. Wutthiprom, P. Chiochan, P. Suktha, M. Suksomboon, S. Kalasina, M. Sawangphruk, Turning conductive carbon nanospheres into

nanosheets for high-performance supercapacitors of MnO_2 nanorods, Chemical communications, 52 (2016) 2585-2588.

[119] C. Yang, X. Li, L. Yu, X. Liu, J. Yang, M. Wei, A new promising Ni-MOF superstructure for high-performance supercapacitors, Chemical Communications, 56 (2020) 1803-1806.

[120] A. Gopalakrishnan, S. Badhulika, Facile sonochemical assisted synthesis of a hybrid red-black phosphorus/sulfonated porous carbon composite for high-performance supercapacitors, Chemical Communications, 56 (2020) 7096-7099.

[121] A. Afif, S.M.H. Rahman, A.T. Azad, J. Zaini, M.A. Islan, A.K. Azad, Advanced materials and technologies for hybrid supercapacitors for energy storage-A review, Journal of Energy Storage, 25 (2019) 100852.

[122] A. Roy, A. Ray, S. Saha, M. Ghosh, T. Das, B. Satpati, M. Nandi, S. Das, NiO-CNT composite for high performance supercapacitor electrode and oxygen evolution reaction, Electrochimica Acta, 283 (2018) 327-337.

[123] B. Zhao, J. Song, P. Liu, W. Xu, T. Fang, Z. Jiao, H. Zhang, Y. Jiang, Monolayer graphene/NiO nanosheets with two-dimension structure for supercapacitors, Journal of Materials Chemistry, 21 (2011) 18792-18798.

[124] J. Ma, J. Yang, L. Jiao, Y. Mao, T. Wang, X. Duan, J. Lian, W. Zheng, NiO nanomaterials: controlled fabrication, formation mechanism and the application in lithium-ion battery, CrystEngComm, 14 (2012) 453-459.

[125] X. Zhang, W. Shi, J. Zhu, W. Zhao, J. Ma, S. Mhaisalkar, T.L. Maria, Y. Yang, H.

Zhang, H.H. Hng, Synthesis of porous NiO nanocrystals with controllable surface area and their application as supercapacitor electrodes, Nano Research, 3 (2010) 643-652.

[126] I. Hotovy, J. Huran, P. Siciliano, S. Capone, L. Spiess, V. Rehacek, The influences of preparation parameters on NiO thin film properties for gas-sensing application, Sensors and Actuators B: Chemical, 78 (2001) 126-132.

[127] F. Motahari, M.R. Mozdianfard, F. Soofivand, M. Salavati-Niasari, NiO nanostructures: synthesis, characterization and photocatalyst application in dye wastewater treatment, RSC advances, 4 (2014) 27654-27660.

[128] J.-W. Lang, L.-B. Kong, W.-J. Wu, Y.-C. Luo, L. Kang, Facile approach to prepare loose-packed NiO nano-flakes materials for supercapacitors, Chemical Communications, (2008) 4213-4215.

[129] P. Justin, S.K. Meher, G.R. Rao, Tuning of capacitance behavior of NiO using anionic, cationic, and nonionic surfactants by hydrothermal synthesis, The Journal of Physical Chemistry C, 114 (2010) 5203-5210.

[130] X. Wang, L. Li, Y.g. Zhang, S. Wang, Z. Zhang, L. Fei, Y. Qian, High-yield synthesis of NiO nanoplatelets and their excellent electrochemical performance, Crystal growth & design, 6 (2006) 2163-2165.

[131] H. Liu, G. Wang, J. Liu, S. Qiao, H. Ahn, Highly ordered mesoporous NiO anode material for lithium ion batteries with an excellent electrochemical performance, Journal of Materials Chemistry, 21 (2011) 3046-3052.

[132] M. Liu, J. Chang, J. Sun, L. Gao, A facile preparation of NiO/Ni composites as

high-performance pseudocapacitor materials, RSC advances, 3 (2013) 8003-8008.

[133] A.K. Singh, D. Sarkar, G.G. Khan, K. Mandal, Unique hydrogenated Ni/NiO core/shell 1D nano-heterostructures with superior electrochemical performance as supercapacitors, Journal of Materials Chemistry A, 1 (2013) 12759-12767.

[134] Y. Feng, H. Zhang, W. Li, L. Fang, Y. Wang, Targeted synthesis of novel hierarchical sandwiched NiO/C arrays as high-efficiency lithium ion batteries anode, Journal of Power Sources, 301 (2016) 78-86.

[135] M. Hakamada, T. Abe, M. Mabuchi, Electrodes from carbon nanotubes/NiO nanocomposites synthesized in modified Watts bath for supercapacitors, Journal of Power Sources, 325 (2016) 670-674.

[136] Y. Liu, C. Gao, Q. Li, H. Pang, Nickel oxide/graphene composites: synthesis and applications, Chemistry-A European Journal, 25 (2019) 2141-2160.

[137] Y. Bu, S. Wang, H. Jin, W. Zhang, J. Lin, J. Wang, Synthesis of porous NiO/reduced graphene oxide composites for supercapacitors, Journal of the Electrochemical Society, 159 (2012) A990.

[138] X. Hui, L. Qian, G. Harris, T. Wang, J. Che, Fast fabrication of NiO@graphene composites for supercapacitor electrodes: Combination of reduction and deposition, Materials & design, 109 (2016) 242-250.

[139] T. Li, G.H. Li, L.H. Li, L. Liu, Y. Xu, H.Y. Ding, T. Zhang, Large-scale self-assembly of 3D flower-like hierarchical Ni/Co-LDHs microspheres for high-performance flexible asymmetric supercapacitors, ACS applied materials

& interfaces, 8 (2016) 2562-2572.

[140] L. Nie, H. Wang, Y. Chai, S. Liu, R. Yuan, In situ formation of flower-like $CuCo_2S_4$ nanosheets/graphene composites with enhanced lithium storage properties, RSC advances, 6 (2016) 38321-38327.

[141] M.-S. Wu, Y.-A. Huang, C.-H. Yang, Capacitive behavior of porous nickel oxide/hydroxide electrodes with interconnected nanoflakes synthesized by anodic electrodeposition, Journal of the Electrochemical Society, 155 (2008) A798.

[142] M. Michalska, L. Lipińska, M. Mirkowska, M. Aksienionek, R. Diduszko, M. Wasiucionek, Nanocrystalline lithium-manganese oxide spinels for Li-ion batteries-Sol-gel synthesis and characterization of their structure and selected physical properties, Solid State Ionics, 188 (2011) 160-164.

[143] P. Kaspar, D. Sobola, K. Částková, R. Dallaev, E. Šťastná, P. Sedlák, A. Knápek, T. Trčka, V. Holcman, Case study of polyvinylidene fluoride doping by carbon nanotubes, Materials, 14 (2021) 1428.

[144] J. Chastain, R.C. King Jr, Handbook of X-ray photoelectron spectroscopy, Perkin-Elmer Corporation, 40 (1992) 221.

[145] N.M. Vuong, N.M. Hieu, H.N. Hieu, H. Yi, D. Kim, Y.-S. Han, M. Kim, Ni_2O_3-decorated SnO_2 particulate films for methane gas sensors, Sensors and Actuators B: Chemical, 192 (2014) 327-333.

[146] C. Yin, W. Wan, H. Xie, W. Weng, G. Li, B. Li, Y. Wang, X. Wu, W. Sun, Supercapacitance Performances of Electrodeposited Nickel Oxide/Graphene

Nanocomposite, Int. J. Electrochem. Sci, 14 (2019) 4185-4194.

[147] J. Lin, H. Jia, H. Liang, S. Chen, Y. Cai, J. Qi, C. Qu, J. Cao, W. Fei, J. Feng, In situ synthesis of vertical standing nanosized NiO encapsulated in graphene as electrodes for high-performance supercapacitors, Advanced science, 5 (2018) 1700687.

[148] D.T. Dam, X. Wang, J.-M. Lee, Graphene/NiO nanowires: controllable one-pot synthesis and enhanced pseudocapacitive behavior, ACS applied materials & interfaces, 6 (2014) 8246-8256.

[149] Z. Wang, P. Tammela, J. Huo, P. Zhang, M. Strømme, L. Nyholm, Solution-processed poly (3, 4-ethylenedioxythiophene) nanocomposite paper electrodes for high-capacitance flexible supercapacitors, Journal of Materials Chemistry A, 4 (2016) 1714-1722.

[150] Y. Jiang, D. Chen, J. Song, Z. Jiao, Q. Ma, H. Zhang, L. Cheng, B. Zhao, Y. Chu, A facile hydrothermal synthesis of graphene porous NiO nanocomposite and its application in electrochemical capacitors, Electrochimica Acta, 91 (2013) 173-178.

[151] W. Chen, D. Gui, J. Liu, Nickel oxide/graphene aerogel nanocomposite as a supercapacitor electrode material with extremely wide working potential window, Electrochimica Acta, 222 (2016) 1424-1429.

[152] X. Feng, J. Zhou, L. Wang, Y. Li, Z. Huang, S. Chen, Y. Ma, L. Wang, X. Yan, Synthesis of shape-controlled NiO-graphene nanocomposites with enhanced supercapacitive properties, New Journal of Chemistry, 39 (2015) 4026-4034.

[153] Z. Wei, J. Li, R. Wang, Surface engineered polar CeO_2-based cathode host materials for immobilizing lithium polysulfides in High-performance Li-S batteries, Applied Surface Science, 580 (2022) 152237.

[154] P. Liu, M. Yang, S. Zhou, Y. Huang, Y. Zhu, Hierarchical shell-core structures of concave spherical NiO nanospines@carbon for high performance supercapacitor electrodes, Electrochimica Acta, 294 (2019) 383-390.

[155] J. Liu, J. Wang, C. Xu, H. Jiang, C. Li, L. Zhang, J. Lin, Z.X. Shen, Advanced energy storage devices: basic principles, analytical methods, and rational materials design, Advanced science, 5 (2018) 1700322.

[156] H. Vijeth, S.P. Ashokkumar, L. Yesappa, M. Vandana, H. Devendrappa, Hybrid core-shell nanostructure made of chitosan incorporated polypyrrole nanotubes decorated with NiO for all-solid-state symmetric supercapacitor application, Electrochimica Acta, 354 (2020) 136651.

[157] S. Vijayakumar, S. Nagamuthu, G. Muralidharan, Supercapacitor studies on NiO nanoflakes synthesized through a microwave route, ACS applied materials & interfaces, 5 (2013) 2188-2196.

[158] B. Zhao, H. Zhuang, T. Fang, Z. Jiao, R. Liu, X. Ling, B. Lu, Y. Jiang, Self-assembly of NiO/graphene with three-dimension hierarchical structure as high performance electrode material for supercapacitors, Journal of alloys and compounds, 597 (2014) 291-298.

[159] X. Su, H. Chai, D. Jia, S. Bao, W. Zhou, M. Zhou, Effective microwave-assisted synthesis of graphene nanosheets/NiO composite for high-performance

supercapacitors, New Journal of Chemistry, 37 (2013) 439-443.

[160] Q. Zheng, Z. Cai, Z. Ma, S. Gong, Cellulose nanofibril/reduced graphene oxide/carbon nanotube hybrid aerogels for highly flexible and all-solid-state supercapacitors, ACS applied materials & interfaces, 7 (2015) 3263-3271.

[161] H. Li, H. Yang, C. Lei, Chapter Formability and Performance of Al-Zn-Mg-Cu Alloys with Different Initial Tempers in Creep Aging Process, (2017).

[162] Y.-G. Zhu, G.-S. Cao, C.-Y. Sun, J. Xie, S.-Y. Liu, T.-J. Zhu, X.B. Zhao, H.Y. Yang, Design and synthesis of NiO nanoflakes/graphene nanocomposite as high performance electrodes of pseudocapacitor, RSC advances, 3 (2013) 19409-19415.

[163] Z. Wei, J. Li, Y. Wang, R. Wang, High-performance Li-S batteries enabled by polysulfide-infiltrated free-standing 3D carbon cloth with CeO_2 nanorods decoration, Electrochimica Acta, 388 (2021) 138645.

[164] Z. Wei, R. Wang, Chemically etched CeO_{2-x} nanorods with abundant surface defects as effective cathode additive for trapping lithium polysulfides in Li-S batteries, Journal of Colloid and Interface Science, 615 (2022) 527-542.

[165] S. Azam, Z. Wei, R. Wang, Cerium oxide nanorods anchored on carbon nanofibers derived from cellulose paper as effective interlayer for lithium sulfur battery, Journal of Colloid and Interface Science, 615 (2022) 417-431.

[166] M. Zhang, H. Du, Z. Wei, X. Zhang, R. Wang, Ultrafast microwave synthesis of nickel-cobalt sulfide/graphene hybrid electrodes for high-performance asymmetrical supercapacitors, ACS Applied Energy Materials, 4 (2021)

8262-8274.

[167] M. Zhang, A. Nautiyal, H. Du, Z. Wei, X. Zhang, R. Wang, Electropolymerization of polyaniline as high-performance binder free electrodes for flexible supercapacitor, Electrochimica Acta, 376 (2021) 138037.

[168] M. Zhang, H. Du, Z. Wei, X. Zhang, R. Wang, Facile Electrodeposition of Mn-CoP Nanosheets on Ni Foam as High-Rate and Ultrastable Electrodes for Supercapacitors, ACS Applied Energy Materials, 5 (2021) 186-195.

[169] B. Xu, H. Zhang, H. Mei, D. Sun, Recent progress in metal-organic framework-based supercapacitor electrode materials, Coordination Chemistry Reviews, 420 (2020) 213438.

[170] M. Guan, Q. Wang, X. Zhang, J. Bao, X. Gong, Y. Liu, Two-dimensional transition metal oxide and hydroxide-based hierarchical architectures for advanced supercapacitor materials, Frontiers in Chemistry, 8 (2020) 390.

[171] D. Chen, J. Li, Q. Wu, Review of V_2O_5-based nanomaterials as electrode for supercapacitor, Journal of Nanoparticle Research, 21 (2019) 1-15.

[172] D. Choi, G.E. Blomgren, P.N. Kumta, Fast and reversible surface redox reaction in nanocrystalline vanadium nitride supercapacitors, Advanced Materials, 18 (2006) 1178-1182.

[173] D.J. Ahirrao, K. Mohanapriya, N. Jha, V_2O_5 nanowires-graphene composite as an outstanding electrode material for high electrochemical performance and long-cycle-life supercapacitor, Materials Research Bulletin, 108 (2018) 73-82.

[174] B. Balamuralitharan, I.-H. Cho, J.-S. Bak, H.-J. Kim, V_2O_5 nanorod electrode

material for enhanced electrochemical properties by a facile hydrothermal method for supercapacitor applications, New Journal of Chemistry, 42 (2018) 11862-11868.

[175] B. Saravanakumar, K.K. Purushothaman, G. Muralidharan, Fabrication of two-dimensional reduced graphene oxide supported V_2O_5 networks and their application in supercapacitors, Materials Chemistry and Physics, 170 (2016) 266-275.

[176] Y. Wu, G. Gao, H. Yang, W. Bi, X. Liang, Y. Zhang, G. Zhang, G. Wu, Controlled synthesis of V_2O_5/MWCNT core/shell hybrid aerogels through a mixed growth and self-assembly methodology for supercapacitors with high capacitance and ultralong cycle life, Journal of Materials Chemistry A, 3 (2015) 15692-15699.

[177] X. Lu, C. Shen, Z. Zhang, E. Barrios, L. Zhai, Core-shell composite fibers for high-performance flexible supercapacitor electrodes, ACS applied materials & interfaces, 10 (2018) 4041-4049.

[178] Y. Ma, C. Hou, H. Zhang, Q. Zhang, H. Liu, S. Wu, Z. Guo, Three-dimensional core-shell Fe_3O_4/Polyaniline coaxial heterogeneous nanonets: Preparation and high performance supercapacitor electrodes, Electrochimica Acta, 315 (2019) 114-123.

[179] N. Jabeen, Q. Xia, M. Yang, H. Xia, Unique core-shell nanorod arrays with polyaniline deposited into mesoporous $NiCo_2O_4$ support for high-performance supercapacitor electrodes, ACS applied materials & interfaces, 8 (2016)

6093-6100.

[180] Y. Zeng, Y. Han, Y. Zhao, Y. Zeng, M. Yu, Y. Liu, H. Tang, Y. Tong, X. Lu, Advanced Ti-doped Fe_2O_3@PEDOT core/shell anode for high-energy asymmetric supercapacitors, Advanced energy materials, 5 (2015) 1402176.

[181] H. Wang, M. Liang, D. Duan, W. Shi, Y. Song, Z. Sun, Rose-like Ni_3S_4 as battery-type electrode for hybrid supercapacitor with excellent charge storage performance, Chemical Engineering Journal, 350 (2018) 523-533.

[182] X. Liang, G. Gao, X. Jiang, W. Zhang, W. Bi, J. Wang, Y. Du, G. Wu, Preparation of hydrophobic PPy coated V_2O_5 yolk-shell nanospheres-based cathode materials with excellent cycling performance, ACS Applied Energy Materials, 3 (2020) 2791-2802.

[183] J.-G. Wang, H. Liu, H. Liu, W. Hua, M. Shao, Interfacial constructing flexible V_2O_5@polypyrrole core-shell nanowire membrane with superior supercapacitive performance, ACS applied materials & interfaces, 10 (2018) 18816-18823.

[184] P. Asen, S. Shahrokhian, One step electrodeposition of V_2O_5/polypyrrole/graphene oxide ternary nanocomposite for preparation of a high performance supercapacitor, International journal of hydrogen energy, 42 (2017) 21073-21085.

[185] L.L. Zhang, S. Zhao, X.N. Tian, X.S. Zhao, Layered graphene oxide nanostructures with sandwiched conducting polymers as supercapacitor electrodes, Langmuir, 26 (2010) 17624-17628.

[186] G.A. Snook, G.Z. Chen, D.J. Fray, M. Hughes, M. Shaffer, Studies of deposition of and charge storage in polypyrrole-chloride and polypyrrole-carbon nanotube composites with an electrochemical quartz crystal microbalance, Journal of Electroanalytical Chemistry, 568 (2004) 135-142-.

[187] G.A. Snook, G.Z. Chen, The measurement of specific capacitances of conducting polymers using the quartz crystal microbalance, Journal of Electroanalytical Chemistry, 612 (2008) 140-146-.

[188] K.P. Vidanapathirana, M.A. Careem, S. Skaarup, K. West, Ion movement in polypyrrole/dodecylbenzenesulphonate films in aqueous and non-aqueous electrolytes, Solid State Ionics, 154 (2002) 331-335-.

[189] R. Ramkumar, M. Minakshi, Fabrication of ultrathin $CoMoO_4$ nanosheets modified with chitosan and their improved performance in energy storage device, Dalton Transactions, 44 (2015) 6158-6168.

[190] Y. Lu, H. Yan, D. Zhang, J. Lin, Y. Xue, J. Li, Y. Luo, C. Tang, Hybrid nanonet/nanoflake $NiCo_2O_4$ electrodes with an ultrahigh surface area for supercapacitors, Journal of Solid State Electrochemistry, 18 (2014) 3143-3152.

[191] X. Sun, Q. Li, Y. Mao, Understanding the influence of polypyrrole coating over V_2O_5 nanofibers on electrochemical properties, Electrochimica Acta, 174 (2015) 563-573.

[192] V. Aravindan, Y.L. Cheah, W.F. Mak, G. Wee, B.V.R. Chowdari, S. Madhavi, Fabrication of high energy-density hybrid supercapacitors using electrospun V_2O_5 nanofibers with a self-supported carbon nanotube network,

ChemPlusChem, 77 (2012) 570-575.

[193] J. Xue, Q. Yang, R. Guan, Q. Shen, X. Liu, H. Jia, Q. Li, High-performance ordered porous Polypyrrole/ZnO films with improved specific capacitance for supercapacitors, Materials Chemistry and Physics, 256 (2020) 123591.

[194] A.M. Cao, J.S. Hu, H.P. Liang, L.J. Wan, Self-assembled vanadium pentoxide (V_2O_5) hollow microspheres from nanorods and their application in lithium-Ion batteries, Angewandte Chemie International Edition, 44 (2005) 4391-4395.

[195] K. Kong, W. Xue, W. Zhu, W. Ye, Z. Zhang, R. Zhao, D. He, The fabrication of bowl-shaped polypyrrole/graphene nanostructural electrodes and its application in all-solid-state supercapacitor devices, Journal of Power Sources, 470 (2020) 228452.

[196] E.P. Randviir, C.E. Banks, Electrochemical impedance spectroscopy: an overview of bioanalytical applications, Analytical methods, 5 (2013) 1098-1115.

[197] W. Zhang, Y. Wang, X. Guo, Y. Liu, Y. Zheng, M. Zhang, R. Li, Z. Peng, Z. Wang, T. Zhang, High performance $Bi_2O_2CO_3$/rGO electrode material for asymmetric solid-state supercapacitor application, Journal of Alloys and Compounds, 855 (2021) 157394.

[198] B.K. Lesel, J.S. Ko, B. Dunn, S.H. Tolbert, Mesoporous Li x Mn_2O_4 thin film cathodes for lithium-ion pseudocapacitors, ACS nano, 10 (2016) 7572-7581.

[199] J.W. Kim, V. Augustyn, B. Dunn, The effect of crystallinity on the rapid pseudocapacitive response of Nb_2O_5, Advanced Energy Materials, 2 (2012)

141-148.

[200] H. Liu, W. Zhu, D. Long, J. Zhu, G. Pezzotti, Porous V_2O_5 nanorods/reduced graphene oxide composites for high performance symmetric supercapacitors, Applied Surface Science, 478 (2019) 383-392.

[201] Z. Chen, V. Augustyn, J. Wen, Y. Zhang, M. Shen, B. Dunn, Y. Lu, High-performance supercapacitors based on intertwined CNT/V_2O_5 nanowire nanocomposites, Advanced materials, 23 (2011) 791-795.

[202] G. Sun, H. Ren, Z. Shi, L. Zhang, Z. Wang, K. Zhan, Y. Yan, J. Yang, B. Zhao, V_2O_5/vertically-aligned carbon nanotubes as negative electrode for asymmetric supercapacitor in neutral aqueous electrolyte, Journal of Colloid and Interface Science, 588 (2021) 847-856.

[203] B. Hu, Q. Xiang, Y. Cen, S. Li, L. Liu, D. Yu, C. Chen, In situ constructing flexible V_2O_5@GO composite thin film electrode for superior electrochemical energy storage, Journal of the Electrochemical Society, 165 (2018) A3738.

[204] A.-Y. Wang, M. Chaudhary, T.-W. Lin, Enhancing the stability and capacitance of vanadium oxide nanoribbons/3D-graphene binder-free electrode by using $VOSO_4$ as redox-active electrolyte, Chemical Engineering Journal, 355 (2019) 830-839.

[205] H. Jiang, X. Cai, Y. Qian, C. Zhang, L. Zhou, W. Liu, B. Li, L. Lai, W. Huang, V_2O_5 embedded in vertically aligned carbon nanotube arrays as free-standing electrodes for flexible supercapacitors, Journal of Materials Chemistry A, 5 (2017) 23727-23736.

[206] K. Sharma, A. Arora, S.K. Tripathi, Review of supercapacitors: Materials and devices, Journal of Energy Storage, 21 (2019) 801-825.

[207] G. Wang, L. Zhang, J. Zhang, A review of electrode materials for electrochemical supercapacitors, Chemical Society Reviews, 41 (2012) 797-828.

[208] Y. Wang, X. Wu, Y. Han, T. Li, Flexible supercapacitor: overview and outlooks, Journal of Energy Storage, 42 (2021) 103053.

[209] W.K. Chee, H.N. Lim, Z. Zainal, N.M. Huang, I. Harrison, Y. Andou, Flexible graphene-based supercapacitors: a review, The Journal of Physical Chemistry C, 120 (2016) 4153-4172.

[210] N. Hillier, S. Yong, S. Beeby, The good, the bad and the porous: A review of carbonaceous materials for flexible supercapacitor applications, Energy Reports, 6 (2020) 148-156.

[211] Y. Huang, H. Li, Z. Wang, M. Zhu, Z. Pei, Q. Xue, Y. Huang, C. Zhi, Nanostructured polypyrrole as a flexible electrode material of supercapacitor, Nano Energy, 22 (2016) 422-438.

[212] T.-F. Yi, L.-Y. Qiu, J. Mei, S.-Y. Qi, P. Cui, S. Luo, Y.-R. Zhu, Y. Xie, Y.-B. He, Porous spherical NiO@$NiMoO_4$@PPy nanoarchitectures as advanced electrochemical pseudocapacitor materials, Science Bulletin, 65 (2020) 546-556.

[213] H. Fu, Z.-j. Du, W. Zou, H.-q. Li, C. Zhang, Carbon nanotube reinforced polypyrrole nanowire network as a high-performance supercapacitor electrode,

Journal of Materials Chemistry A, 1 (2013) 14943-14950.

[214] T. Qian, C. Yu, S. Wu, J. Shen, A facilely prepared polypyrrole–reduced graphene oxide composite with a crumpled surface for high performance supercapacitor electrodes, Journal of Materials Chemistry A, 1 (2013) 6539-6542.

[215] P. Gahlout, V. Choudhary, Tailoring of polypyrrole backbone by optimizing synthesis parameters for efficient EMI shielding properties in X-band (8.2-12.4 GHz), Synthetic Metals, 222 (2016) 170-179.

[216] Y.M. Huang, F.-f. Zhou, Y. Deng, B.-g. Zhai, Effects of salt 9, 10-anthraquinone-2-sulfonic acid sodium on the conductivity of polypyrrole, Solid State Ionics, 179 (2008) 1305-1309.

[217] W. Wang, Z. Li, T. Jiang, Z. Zhao, Y. Li, Z. Wang, C. Wang, Sulfonated poly (ether ether ketone)/polypyrrole core-shell nanofibers: a novel polymeric adsorbent/conducting polymer nanostructures for ultrasensitive gas sensors, ACS applied materials & interfaces, 4 (2012) 6080-6084.

[218] R.S. Malik, S.N. Tripathi, D. Gupta, V. Choudhary, Novel anhydrous composite membranes based on sulfonated poly (ether ketone) and aprotic ionic liquids for high temperature polymer electrolyte membranes for fuel cell applications, International journal of hydrogen energy, 39 (2014) 12826-12834.

[219] J. Ouyang, C.W. Chu, F.C. Chen, Q. Xu, Y. Yang, High-conductivity poly (3, 4-ethylenedioxythiophene): poly (styrene sulfonate) film and its application in polymer optoelectronic devices, Advanced Functional Materials, 15 (2005)

203-208.

[220] S. Maruthamuthu, J. Chandrasekaran, D. Manoharan, R. Magesh, Conductivity and dielectric analysis of nanocolloidal polypyrrole particles functionalized with higher weight percentage of poly (styrene sulfonate) using the dispersion polymerization method, Journal of Polymer Engineering, 37 (2017) 481-492.

[221] C. Miao, H. Du, X. Zhang, H.V. Tippur, Dynamic crack initiation and growth in cellulose nanopaper, Cellulose, 29 (2022) 557-569.

[222] H. Liu, H. Du, T. Zheng, K. Liu, X. Ji, T. Xu, X. Zhang, C. Si, Cellulose based composite foams and aerogels for advanced energy storage devices, Chemical Engineering Journal, 426 (2021) 130817.

[223] D. Zhao, Q. Zhang, W. Chen, X. Yi, S. Liu, Q. Wang, Y. Liu, J. Li, X. Li, H. Yu, Highly flexible and conductive cellulose-mediated PEDOT:PSS/MWCNT composite films for supercapacitor electrodes, ACS applied materials & interfaces, 9 (2017) 13213-13222.

[224] J.P. Jyothibasu, D.-W. Kuo, R.-H. Lee, Flexible and freestanding electrodes based on polypyrrole/carbon nanotube/cellulose composites for supercapacitor application, Cellulose, 26 (2019) 4495-4513.

[225] H. Du, M. Zhang, K. Liu, M. Parit, Z. Jiang, X. Zhang, B. Li, C. Si, Conductive PEDOT:PSS/cellulose nanofibril paper electrodes for flexible supercapacitors with superior areal capacitance and cycling stability, Chemical Engineering Journal, 428 (2022) 131994.

[226] M. Parit, H. Du, X. Zhang, C. Prather, M. Adams, Z. Jiang, Polypyrrole and

cellulose nanofiber based composite films with improved physical and electrical properties for electromagnetic shielding applications, Carbohydrate polymers, 240 (2020) 116304.

[227] S. Li, Q. Shi, Y. Li, J. Yang, T.H. Chang, J. Jiang, P.Y. Chen, Intercalation of Metal Ions into $Ti_3C_2T_x$ MXene Electrodes for High-Areal-Capacitance Microsupercapacitors with Neutral Multivalent Electrolytes, Advanced Functional Materials, 30 (2020) 2003721.

[228] C. Wan, Y. Jiao, J. Li, Flexible, highly conductive, and free-standing reduced graphene oxide/polypyrrole/cellulose hybrid papers for supercapacitor electrodes, Journal of Materials Chemistry A, 5 (2017) 3819-3831.

[229] S. Maruthamuthu, J. Chandrasekaran, D. Manoharan, S.N. Karthick, H.J. Kim, Multilayer photoactive nanocolloidal PPy: PSS as a novel substitute for Pt free counter electrode in DSSC, Journal of Applied Polymer Science, 133 (2016).

[230] M. Lay, M.À. Pèlach, N. Pellicer, J.A. Tarrés, K.N. Bun, F. Vilaseca, Smart nanopaper based on cellulose nanofibers with hybrid PEDOT:PSS/polypyrrole for energy storage devices, Carbohydrate polymers, 165 (2017) 86-95.

[231] X. Fei, J. Wang, J. Zhu, X. Wang, X. Liu, Biobased Poly (ethylene 2, 5-furancoate): No longer an alternative, but an irreplaceable polyester in the polymer industry, ACS Sustainable Chemistry & Engineering, 8 (2020) 8471-8485.

[232] G. Fei, Y. Wang, H. Wang, Y. Ma, Q. Guo, W. Huang, D. Yang, Y. Shao, Y. Ni, Fabrication of bacterial cellulose/polyaniline nanocomposite paper with

excellent conductivity, strength, and flexibility, ACS Sustainable Chemistry & Engineering, 7 (2019) 8215-8225.

[233] Y. Li, H. Zhang, S. Ni, H. Xiao, In situ synthesis of conductive nanocrystal cellulose/polypyrrole composite hydrogel based on semi-interpenetrating network, Materials Letters, 232 (2018) 175-178.

[234] H. Kashani, L. Chen, Y. Ito, J. Han, A. Hirata, M. Chen, Bicontinuous nanotubular graphene-polypyrrole hybrid for high performance flexible supercapacitors, Nano Energy, 19 (2016) 391-400.

[235] J. Zhang, P. Chen, B.H.L. Oh, M.B. Chan-Park, High capacitive performance of flexible and binder-free graphene-polypyrrole composite membrane based on in situ reduction of graphene oxide and self-assembly, Nanoscale, 5 (2013) 9860-9866.

[236] X. Guan, L. Pan, Z. Fan, Flexible, transparent and highly conductive polymer film electrodes for all-solid-state transparent supercapacitor applications, Membranes, 11 (2021) 788.

[237] H. Du, M. Parit, K. Liu, M. Zhang, Z. Jiang, T.-S. Huang, X. Zhang, C. Si, Engineering cellulose nanopaper with water resistant, antibacterial, and improved barrier properties by impregnation of chitosan and the followed halogenation, Carbohydrate Polymers, 270 (2021) 118372.

[238] F. Miao, C. Shao, X. Li, K. Wang, N. Lu, Y. Liu, Electrospun carbon nanofibers/carbon nanotubes/polyaniline ternary composites with enhanced electrochemical performance for flexible solid-state supercapacitors, ACS

Sustainable Chemistry & Engineering, 4 (2016) 1689-1696.

[239] L. Xia, X. Li, Y. Wu, S. Hu, Y. Liao, L. Huang, Y. Qing, X. Lu, Electrodes derived from carbon fiber-reinforced cellulose nanofiber/multiwalled carbon nanotube hybrid aerogels for high-energy flexible asymmetric supercapacitors, Chemical Engineering Journal, 379 (2020) 122325.

[240] M. Hou, M. Xu, Y. Hu, B. Li, Nanocellulose incorporated graphene/polypyrrole film with a sandwich-like architecture for preparing flexible supercapacitor electrodes, Electrochimica Acta, 313 (2019) 245-254.

[241] H. Olsson, G. Nyström, M. Strømme, M. Sjödin, L. Nyholm, Cycling stability and self-protective properties of a paper-based polypyrrole energy storage device, Electrochemistry communications, 13 (2011) 869-871.

[242] H. Koga, H. Tonomura, M. Nogi, K. Suganuma, Y. Nishina, Fast, scalable, and eco-friendly fabrication of an energy storage paper electrode, Green Chemistry, 18 (2016) 1117-1124.

[243] B. Anothumakkool, R. Soni, S.N. Bhange, S. Kurungot, Novel scalable synthesis of highly conducting and robust PEDOT paper for a high performance flexible solid supercapacitor, Energy & Environmental Science, 8 (2015) 1339-1347.

[244] T. Wang, W. Zhang, S. Yang, X. Liu, L. Zhang, Preparation of foam-like network structure of polypyrrole/graphene composite particles based on cellulose nanofibrils as electrode material, ACS omega, 5 (2020) 4778-4786.

[245] Q. Fu, Y. Wang, S. Liang, Q. Liu, C. Yao, High-performance flexible

freestanding polypyrrole-coated CNF film electrodes for all-solid-state supercapacitors, Journal of Solid State Electrochemistry, 24 (2020) 533-544.

[246] B. Li, H. Lopez-Beltran, C. Siu, K.H. Skorenko, H. Zhou, W.E. Bernier, M.S. Whittingham, W.E. Jones Jr, Vaper phase polymerized PEDOT/cellulose paper composite for flexible solid-state supercapacitor, ACS Applied Energy Materials, 3 (2020) 1559-1568.

[247] S. Lyu, Y. Chen, L. Zhang, S. Han, Y. Lu, Y. Chen, N. Yang, Z. Chen, S. Wang, Nanocellulose supported hierarchical structured polyaniline/nanocarbon nanocomposite electrode via layer-by-layer assembly for green flexible supercapacitors, RSC advances, 9 (2019) 17824-17834.

[248] Z. Zou, W. Zhou, Y. Zhang, H. Yu, C. Hu, W. Xiao, High-performance flexible all-solid-state supercapacitor constructed by free-standing cellulose/reduced graphene oxide/silver nanoparticles composite film, Chemical Engineering Journal, 357 (2019) 45-55.

[249] R. Liu, L. Ma, S. Huang, J. Mei, J. Xu, G. Yuan, A flexible polyaniline/graphene/bacterial cellulose supercapacitor electrode, New Journal of Chemistry, 41 (2017) 857-864.

[250] W. Wang, Y. Yang, Z. Chen, Z. Deng, L. Fan, W. Guo, J. Xu, Z. Meng, High-performance yarn supercapacitor based on directly twisted carbon nanotube@ bacterial cellulose membrane, Cellulose, 27 (2020) 7649-7661.

[251] Y. Bai, R. Liu, E. Li, X. Li, Y. Liu, G. Yuan, Graphene/carbon nanotube/bacterial cellulose assisted supporting for polypyrrole towards flexible

supercapacitor applications, Journal of Alloys and Compounds, 777 (2019) 524-530.

[252] L. Ma, R. Liu, H. Niu, M. Zhao, Y. Huang, Flexible and freestanding electrode based on polypyrrole/graphene/bacterial cellulose paper for supercapacitor, Composites Science and Technology, 137 (2016) 87-93.

[253] P. Xie, W. Yuan, X. Liu, Y. Peng, Y. Yin, Y. Li, Z. Wu, Advanced carbon nanomaterials for state-of-the-art flexible supercapacitors, Energy Storage Materials, 36 (2021) 56-76.

[254] M.R. Benzigar, V.D.B.C. Dasireddy, X. Guan, T. Wu, G. Liu, Advances on emerging materials for flexible supercapacitors: current trends and beyond, Advanced Functional Materials, 30 (2020) 2002993.

[255] P. Liu, J. Yan, Z. Guang, Y. Huang, X. Li, W. Huang, Recent advancements of polyaniline-based nanocomposites for supercapacitors, Journal of Power Sources, 424 (2019) 108-130.

[256] J. Banerjee, K. Dutta, M.A. Kader, S.K. Nayak, An overview on the recent developments in polyaniline-based supercapacitors, Polymers for Advanced Technologies, 30 (2019) 1902-1921.

[257] R. Malik, S. Lata, R.S. Malik, Electrochemical behavior of composite electrode based on sulphonated polymeric surfactant (SPEEK/PSS) incorporated polypyrrole for supercapacitor, Journal of Electroanalytical Chemistry, 835 (2019) 48-59.

[258] K. Lee, H. Yu, J.W. Lee, J. Oh, S. Bae, S.K. Kim, J. Jang, Efficient and

moisture-resistant hole transport layer for inverted perovskite solar cells using solution-processed polyaniline, Journal of Materials Chemistry C, 6 (2018) 6250-6256.

[259] G.E. Fenoy, B. Van der Schueren, J. Scotto, F. Boulmedais, M.R. Ceolín, S. Bégin-Colin, D. Bégin, W.A. Marmisollé, O. Azzaroni, Layer-by-layer assembly of iron oxide-decorated few-layer graphene/PANI:PSS composite films for high performance supercapacitors operating in neutral aqueous electrolytes, Electrochimica Acta, 283 (2018) 1178-1187.

[260] R. Zhang, J. Qian, S. Ye, Y. Zhou, Z. Zhu, Enhanced electrochemical capacitive performance of “sandwich-like” MWCNTs/PANI/PSS-GR electrode materials, RSC advances, 6 (2016) 100954-100961.

[261] K. Gholami Laelabadi, R. Moradian, I. Manouchehri, One-step fabrication of flexible, cost/time effective, and high energy storage reduced graphene oxide@PANI supercapacitor, ACS Applied Energy Materials, 3 (2020) 5301-5312.

[262] G.-T. Xia, C. Li, K. Wang, L.-W. Li, Structural design and electrochemical performance of PANI/CNTs and MnO_2/CNTs supercapacitor, Science of Advanced Materials, 11 (2019) 1079-1086.

[263] S. Anand, M.W. Ahmad, A.K.A. Al Saidi, D.-J. Yang, A. Choudhury, Polyaniline nanofiber decorated carbon nanofiber hybrid mat for flexible electrochemical supercapacitor, Materials Chemistry and Physics, 254 (2020) 123480.

[264] M.S. Lakshmi, S.M. Wabaidur, Z.A. Alothman, D. Ragupathy, Novel 1D polyaniline nanorods for efficient electrochemical supercapacitors: A facile and green approach, Synthetic Metals, 270 (2020) 116591.

[265] H. Xu, Y. Zhu, M. Zhang, Q. Li, S. Zuo, Y. Chen, Eigenstate PANI-coated paper fiber with graphene materials for high-performance supercapacitor, Ionics, 26 (2020) 5199-5210.

[266] T. Hao, W. Wang, D. Yu, A flexible cotton-based supercapacitor electrode with high stability prepared by multiwalled CNTs/PANI, Journal of Electronic Materials, 47 (2018) 4108-4115.

[267] A. Sharma, M. Thakur, M. Bhattacharya, T. Mandal, S. Goswami, Commercial application of cellulose nano-composites-A review, Biotechnology Reports, 21 (2019) e00316.

[268] L. Deng, R.J. Young, I.A. Kinloch, A.M. Abdelkader, S.M. Holmes, D.A. De Haro-Del Rio, S.J. Eichhorn, Supercapacitance from cellulose and carbon nanotube nanocomposite fibers, ACS applied materials & interfaces, 5 (2013) 9983-9990.

[269] M. Mo, C. Chen, H. Gao, M. Chen, D. Li, Wet-spinning assembly of cellulose nanofibers reinforced graphene/polypyrrole microfibers for high performance fiber-shaped supercapacitors, Electrochimica Acta, 269 (2018) 11-20.

[270] L. Wang, T. Shu, S. Guo, Y. Lu, M. Li, J. Nzabahimana, X. Hu, Fabricating strongly coupled V_2O_5@PEDOT nanobelts/graphene hybrid films with high areal capacitance and facile transferability for transparent solid-state

supercapacitors, Energy Storage Materials, 27 (2020) 150-158.

[271] S. Uzun çar, L. Meng, A.P.F. Turner, W.C. Mak, Processable and nanofibrous polyaniline: polystyrene-sulphonate (nano-PANI:PSS) for the fabrication of catalyst-free ammonium sensors and enzyme-coupled urea biosensors, Biosensors and Bioelectronics, 171 (2021) 112725.

[272] P. Ranka, V. Sethi, A.Q. Contractor, One step electrodeposition of composite of PANI-PSS tubules with TiO_2 nanoparticles and application as electronic sensor device, Sensors and Actuators B: Chemical, 261 (2018) 11-21.

[273] S. Biswas, J. Jeong, J.W. Shim, H. Kim, Improved charge transport in PANI: PSS by the uniform dispersion of silver nanoparticles, Applied Surface Science, 483 (2019) 819-826.

[274] H. Han, J.S. Lee, S. Cho, Comparative studies on two-electrode symmetric supercapacitors based on polypyrrole: Poly(4-styrenesulfonate) with different molecular weights of poly (4-styrenesulfonate), Polymers, 11 (2019) 232.

[275] A.D.W. Carswell, E.A. O'Rea, B.P. Grady, Adsorbed surfactants as templates for the synthesis of morphologically controlled polyaniline and polypyrrole nanostructures on flat surfaces: from spheres to wires to flat films, Journal of the American Chemical Society, 125 (2003) 14793-14800.

[276] G.M. do Nascimento, V.R.L. Constantino, R. Landers, M.L.A. Temperini, Spectroscopic characterization of polyaniline formed in the presence of montmorillonite clay, Polymer, 47 (2006) 6131-6139.

[277] H. Xu, Y. Li, M. Jia, L. Cui, C. Chen, Y. Yang, X. Jin, Design and synthesis of a

3D flexible film electrode based on a sodium carboxymethyl cellulose-polypyrrole@ reduced graphene oxide composite for supercapacitors, New Journal of Chemistry, 45 (2021) 6630-6639.

[278] G. Nystrom, A. Mihranyan, A. Razaq, T. Lindstrom, L. Nyholm, M. Strømme, A nanocellulose polypyrrole composite based on microfibrillated cellulose from wood, The Journal of Physical Chemistry B, 114 (2010) 4178-4182.

[279] Y. Zhang, T. Nypelö, C. Salas, Cellulose nanofibrils: From strong materials to bioactive surfaces. J Renew Mater 1: 195-211, 2013.

[280] D. Zhang, Q. Zhang, X. Gao, G. Piao, A nanocellulose polypyrrole composite based on tunicate cellulose, International Journal of Polymer Science, 2013.

[281] S.S. Nair, N. Yan, Effect of high residual lignin on the thermal stability of nanofibrils and its enhanced mechanical performance in aqueous environments, Cellulose, 22 (2015) 3137-3150.

[282] M. Lay, J.A. Méndez, M. Pèlach, K.N. Bun, F. Vilaseca, Combined effect of carbon nanotubes and polypyrrole on the electrical properties of cellulose-nanopaper, Cellulose, 23 (2016) 3925-3937.

[283] M. Salado, S. Lanceros-Mendez, E. Lizundia, Free-standing intrinsically conducting polymer membranes based on cellulose and poly (vinylidene fluoride) for energy storage applications, European Polymer Journal, 144 (2021) 110240.

[284] C. Yang, D. Li, Flexible and foldable supercapacitor electrodes from the porous 3D network of cellulose nanofibers, carbon nanotubes and polyaniline,

Materials Letters, 155 (2015) 78-81.

[285] K.Y. Yasoda, S. Kumar, M.S. Kumar, K. Ghosh, S.K. Batabyal, Fabrication of MnS/GO/PANI nanocomposites on a highly conducting graphite electrode for supercapacitor application, Materials Today Chemistry, 19 (2021) 100394.

[286] L. Qin, G. Yang, D. Li, K. Ou, H. Zheng, Q. Fu, Y. Sun, High area energy density of all-solid-state supercapacitor based on double-network hydrogel with high content of graphene/PANI fiber, Chemical Engineering Journal, 430 (2022) 133045.

[287] S. Verma, V.K. Pandey, B. Verma, Facile synthesis of graphene oxide-polyaniline-copper cobaltite (GO/PANI/$CuCo_2O_4$) hybrid nanocomposite for supercapacitor applications, Synthetic Metals, 286 (2022) 117036.

[288] D. Ge, L. Yang, L. Fan, C. Zhang, X. Xiao, Y. Gogotsi, S. Yang, Foldable supercapacitors from triple networks of macroporous cellulose fibers, single-walled carbon nanotubes and polyaniline nanoribbons, Nano Energy, 11 (2015) 568-578.

[289] E.-C. Cho, C.-W. Chang-Jian, K.-C. Lee, J.-H. Huang, B.-C. Ho, Y.-R. Ding, Y.-S. Hsiao, Spray-dried nanoporous NiO/PANI:PSS composite microspheres for high-performance asymmetric supercapacitors, Composites Part B: Engineering, 175 (2019) 107066.

[290] J.P. Jyothibasu, R.-H. Wang, K. Ong, J.H.L. Ong, R.-H. Lee, Cellulose/carbon nanotube/MnO_2 composite electrodes with high mass loadings for symmetric supercapacitors, Cellulose, 28 (2021) 3549-3567.

[291] Y. Sun, Y. Yang, L. Fan, W. Zheng, D. Ye, J. Xu, Polypyrrole/$SnCl_2$ modified bacterial cellulose electrodes with high areal capacitance for flexible supercapacitors, Carbohydrate Polymers, (2022) 119679.

[292] W. Chen, D. Zhang, K. Yang, M. Luo, P. Yang, X. Zhou, Mxene ($Ti_3C_2T_x$)/cellulose nanofiber/porous carbon film as free-standing electrode for ultrathin and flexible supercapacitors, Chemical Engineering Journal, 413 (2021) 127524.

[293] Y. Zhang, Z. Shang, M. Shen, S.P. Chowdhury, A. Ignaszak, S. Sun, Y. Ni, Cellulose nanofibers/reduced graphene oxide/polypyrrole aerogel electrodes for high-capacitance flexible all-solid-state supercapacitors, ACS Sustainable Chemistry & Engineering, 7 (2019) 11175-11185.

[294] A. Lu, H. Wan, C. Qin, Flexible, Robust Cellulose/Phytic Acid/Polyaniline Hydrogel for All-in-one Supercapacitor and Strain Sensor, Journal of Materials Chemistry A, (2022).

[295] Z. Zou, W. Xiao, Y. Zhang, H. Yu, W. Zhou, Facile synthesis of freestanding cellulose/RGO/silver/Fe_2O_3 hybrid film for ultrahigh-areal-energy-density flexible solid-state supercapacitor, Applied Surface Science, 500 (2020) 144244.

[296] Q. Gong, Y. Li, X. Liu, Z. Xia, Y. Yang, A facile preparation of polyaniline/cellulose hydrogels for all-in-one flexible supercapacitor with remarkable enhanced performance, Carbohydrate polymers, 245 (2020) 116611.

[297] T. Ouyang, K. Cheng, F. Yang, L. Zhou, K. Zhu, K. Ye, G. Wang, D. Cao, From

biomass with irregular structures to 1D carbon nanobelts: a stripping and cutting strategy to fabricate high performance supercapacitor materials, Journal of Materials Chemistry A, 5 (2017) 14551-14561.

[298] D.P. Dubal, S.H. Lee, J.G. Kim, W.B. Kim, C.D. Lokhande, Porous polypyrrole clusters prepared by electropolymerization for a high performance supercapacitor, Journal of Materials Chemistry, 22 (2012) 3044-3052.

[299] X. Zhang, H. Zhang, C. Li, K. Wang, X. Sun, Y. Ma, Recent advances in porous graphene materials for supercapacitor applications, Rsc Advances, 4 (2014) 45862-45884.

[300] S.M. Jung, D.L. Mafra, C.-T. Lin, H.Y. Jung, J. Kong, Controlled porous structures of graphene aerogels and their effect on supercapacitor performance, Nanoscale, 7 (2015) 4386-4393.

[301] Q. Wang, B. Liu, X. Wang, S. Ran, L. Wang, D. Chen, G. Shen, Morphology evolution of urchin-like $NiCo_2O_4$ nanostructures and their applications as psuedocapacitors and photoelectrochemical cells, Journal of Materials Chemistry, 22 (2012) 21647-21653.

[302] H. Xu, J.-X. Wu, Y. Chen, J.-L. Zhang, B.-Q. Zhang, Facile synthesis of polyaniline/$NiCo_2O_4$ nanocomposites with enhanced electrochemical properties for supercapacitors, Ionics, 21 (2015) 2615-2622.

[303] S. Yadav, A. Devi, Recent advancements of metal oxides/Nitrogen-doped graphene nanocomposites for supercapacitor electrode materials, Journal of Energy Storage, 30 (2020) 101486.

[304] Y. Liu, B. Zhang, Y. Yang, Z. Chang, Z. Wen, Y. Wu, Polypyrrole-coated α-MoO_3 nanobelts with good electrochemical performance as anode materials for aqueous supercapacitors, Journal of Materials Chemistry A, 1 (2013) 13582-13587.

[305] M. Kim, J. Kim, Development of high power and energy density microsphere silicon carbide-MnO_2 nanoneedles and thermally oxidized activated carbon asymmetric electrochemical supercapacitors, Physical Chemistry Chemical Physics, 16 (2014) 11323-11336.